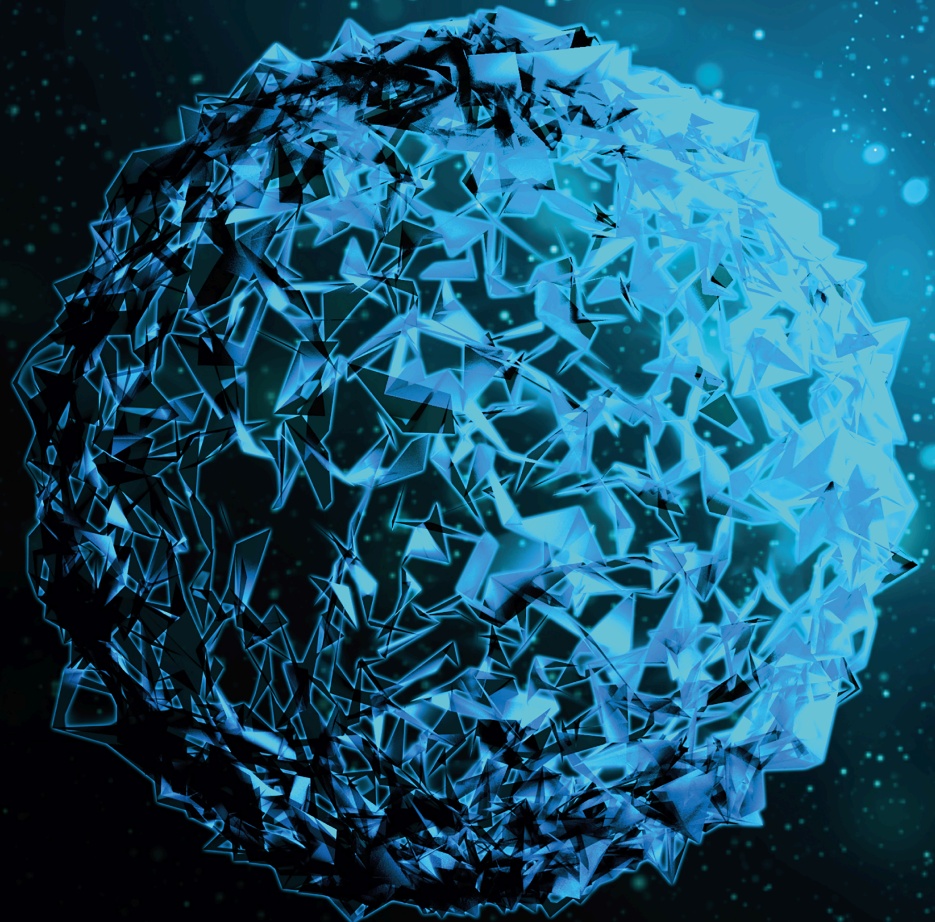# Biomaterials Development, Modification, and Potential Application for Interventional Cardiology

Lead Guest Editor: Jingan Li
Guest Editors: Salvatore De Rosa, Juan Wang, and Kun Zhang

Biomaterials Development, Modification, and Potential Application for Interventional Cardiology

Biomaterials Development, Modification, and Potential Application for Interventional Cardiology

Lead Guest Editor: Jingan Li
Guest Editors: Salvatore De Rosa, Juan Wang, and Kun Zhang

Editorial Board

Contents

Editorial

Biomaterials Development, Modification, and Potential Application for Interventional Cardiology

Jingan Li [iD],[1] Salvatore De Rosa [iD],[2] Juan Wang [iD],[3] and Kun Zhang [iD][1]

[1]Zhengzhou University, Zhengzhou, China
[2]"Magna Graecia" University, Catanzaro, Italy
[3]Yale University, New Haven, USA

Correspondence should be addressed to Jingan Li; lijingan@zzu.edu.cn

Vascular stent interventional therapy is the main approach for the clinical treatment of coronary artery diseases. However, due to the insufficient biocompatibility of cardiovascular materials, the implantation of stents often leads to serious adverse cardiac events. Neointimal hyperplasia contributes to the pathophysiological process of several different vascular disorders, such as restenosis after angioplasty, allograft vasculopathy, vein graft stenosis, and atherosclerosis. Many novel biomaterials such as nanoparticles have attracted tremendous interest. In this special issue, we intend to cover recent experimental progress on the modification of stent materials. The purpose of this special issue is to present the recent progress in biomaterials development, modification, and potential application for interventional cardiology. A brief summary of all accepted papers is provided below.

The paper reported by X. Yue et al. evaluated the mechanical performances of the existing four types of DES with the length of 38 mm, including crossing ability, compliance, elastic recoil, and longitudinal strength. Here, the 38 mm long stents from XIENCE Xpedition (Abbott, US), SYNERGY (Boston Scientific, US), FIREHAWK (Microport, China), and HELIOS (HELIOS, China) were collected. The results indicated that the stents from XIENCE Xpedition and SYNERGY performed the best crossing ability. The reduced ratio of stent diameter from XIENCE Xpedition was the least, indicating better compliance. In addition, the elastic recoil percentage of stents revealed better elastic recoil in the stent from SYNERGY. Moreover, the stent from XIENCE Xpedition had less displacement under pressure with the

best longitudinal strength. The evaluation of mechanical properties for the stent with 38 mm including crossing ability, compliance, elastic recoil, and longitudinal strength for long stents could provide a reference index for the clinical application.

In the paper by S. Liu et al., they have reported the novel fibronectin- (Fn-) loaded poly-L lysine/heparin nanoparticles constructed for stent surface modification. In vitro blood compatibility and in vitro cellular compatibility evaluations were tested. It is found that the incorporation of Fn can improve the binding density of nanoparticles, which may contribute to enhancing the anticoagulant properties of the surface and thereby prevent the coagulation reaction caused by the presence of Fn. In addition, the Fn-loaded nanocoating was found to effectively improve the adhesion and proliferation of vascular endothelial cells on the material surface and thereby accelerate endothelium regeneration. The results showed that the nanoparticles-modified surface could effectively reduce platelet adhesion and activation and provide adequate efficacy in promoting the adhesion and proliferation of endothelial cells and thereby accelerate endothelialization. Based on the structure and function of the extracellular matrix on vascular injury healing, it provides a new approach for the surface biological function modification of vascular stents.

In the paper by Z. Huang et al., they have reported the capability of hydroxyapatite nanoparticles to deliver drugs. Composites containing drug delivery compounds were synthesized by coprecipitation and freeze-drying and then characterized by scanning electron microscopy, X-ray

diffraction, and Fourier transform infrared spectroscopy. The use of hydroxyapatite nanoparticles (nano-SHAP) alone did not affect the proliferation of normal cell lines. However, nanoparticles containing the different amounts of norcantharidin in the composite materials had different inhibitory effects on osteosarcoma and different proliferative effects on osteoblasts. Also, with the increase of the norcantharidin dose, the antitumor performance of the composite has been enhanced. In summary, the nano-SHAP system can inhibit the growth of tumors and induce the proliferation of osteoblasts.

The work by Y. Wang et al. has modified biscarbamate cross-linked polyethylenimine derivative (PEI-Et) through PEGylation and thus obtained polyethylene glycol-graft-polyethylenimine derivative (PEG-Et 1:1), which has lower cytotoxicity and higher gene transfection efficiency compared with PEI-Et. In this study, PEG-Et 1:1 was employed in Smad3 shRNA (shSmad3) delivery for preventing intimal hyperplasia after vascular injury. It was observed that PEG-Et 1:1 could condense shSmad3 gene into nanoparticles with the particle size of 115–168 nm and zeta potential of 3–6 mV. PEG-Et 1:1 displayed remarkably lower cytotoxicity, higher transfection efficiency, and shRNA silencing efficiency than PEI-Et and PEI 25 kDa in vascular smooth muscle cells. Moreover, PEG-Et 1:1/shSmad3 polyplex treatment significantly inhibited collagen, matrix metalloproteinase 1 (MMP1), MMP2 and MMP9 expression, and upregulated tissue inhibitor of metalloproteinase 1 (TIMP1) expression both in vitro and in vivo. Furthermore, intravascular delivery of shSmad3 with PEG-Et 1:1 polyplex efficiently reduced Smad3 expression and inhibited intimal thickening 14 days after vascular injury. Ultimately, this study indicated that PEGEt 1:1-mediated local delivery of shSmad3 is a promising strategy for preventing intimal thickening.

The paper reported by S. Mosbahi et al. aimed to enhance the antiosteoporotic performance of bioactive glass (46S6) through its association with bisphosphonate such as risedronate. In vitro and in vivo explorations have been carried out. The association of bioactive glass and risedronate has been performed by the adsorption process. Structure analyses have been carried out to evaluate and to understand the chemical interactions by the Solid Nuclear Magnetic Resonance and the spectra deconvolution. In vitro experiments showed the enhancement of the chemical reactivity of the composites 46S6-xRIS compared with the pure bioactive glass. In vivo results showed good behavior with only 8% of introduced risedronate in the glass matrix.

Conflicts of Interest

The editors declare that they have no conflicts of interest regarding the publication of this Special Issue.

Acknowledgments

Research Article

Evaluation of Mechanical Performances of Stents with 38 mm Length in Long Lesion

Xiaoting Yue,[1,2] **Jiacheng Guo,**[1,2] **Jianchao Zhang,**[1,2] **Chang Cao,**[1,2] **Zenglei Zhang,**[1,2] **Deliang Shen,**[1,2] **Junnan Tang** ⓘ**,**[1,2] **and Jinying Zhang** ⓘ[1,2]

[1]*Department of Cardiology, The First Affiliated Hospital of Zhengzhou University, Zhengzhou, Henan 450052, China*
[2]*Henan Province Key Laboratory of Cardiac Injury and Repair, Zhengzhou, Henan 450052, China*

Correspondence should be addressed to Junnan Tang; fcctangjn@zzu.edu.cn and Jinying Zhang; jyzhang@zzu.edu.cn

Objective. Single stent with 38 mm length has emerged as a potential solution for long lesion treatment using PCI. However, long stents need to come over a longer lesion length combined with a higher incidence of tortuous calcification, requiring a stent to provide superior transport and compliance and reduce elastic retraction. Here, we evaluated the mechanical performances of the existing four types of drug eluting stents with 38 mm length, which could provide guidance for clinicians to choose the proper stents for the patients. *Methods*. The stents with 38 mm length from XIENCE Xpedition (Abbott, US), SYNERGY (Boston Scientific, US), FIREHAWK (Microport, China), and HELIOS (HELIOS, China) were collected. Mechanical parameters of stents including crossing ability, compliance, elastic recoil, and longitudinal strength were performed. *Results*. The resistance force of stents from XIENCE Xpedition was smaller than FIREHAWK ($p < 0.05$), which indicates that the stent from XIENCE Xpedition has better crossing ability. The ratio of stent diameter reduction from both XIENCE Xpedition and SYNERGY was less than 3% with no statistical difference. In addition, the elastic recoil percentage of stents from SYNERGY, XIENCE Xpedition, FIREHAWK, and HELIOS was 1.16%, 2.62%, 3.66%, and 4.19%, respectively, indicating that SYNERGY had better elastic recoil compared to FIREHAWK and HELIOS ($p < 0.05$). Moreover, the stent from XIENCE Xpedition had less displacement under pressure with the best longitudinal strength ($p < 0.05$). *Conclusion*. The evaluation of mechanical properties for the stent with 38 mm length including crossing ability, compliance, elastic recoil, and longitudinal strength could provide reference index for more accurately clinical application for long lesion treatment.

1. Introduction

Complex coronary lesions, especially the long lesion, still remain a challenge for intervention cardiologists, which usually require multiple stent implantations. The coronary artery lesion greater than 20 mm is defined as a long lesion. Percutaneous coronary intervention (PCI) preformation in long lesion could be the overlapping of several stents, and in fact, stent overlap has been reported in as many as 30% of patients undergoing PCI. In the age of bare metal stents (BMS), stent length was an independent predictor of in-stent restenosis (ISR) [1]. Thus, often, PCI operation was not recommended for the long lesion.

With the development of the drug-eluting stent (DES), after the year of 2000, the risk of ISR dropped from 20%–30% in the BMS era to 5%–10% in the DES era [2–6]. However, the late restenosis rate after DES implantation is still relatively high [7], especially multiple stent implantation. The common approach for current clinical setting still involves the overlapping of two short stents. Unfortunately, the overlapping method in clinical application is deficiency in some extent. Multiple stent implantation could result in the excessive overlap of double-layer stent beams or the geographical loss between the overlapped two short stents easily, together with the prolonged operation time and extensive medical expenses. For some type of long lesions,

the overlapping length of stents can be either too long or too short. While both of excessive overlap and longer total length of the stents by less overlapping may lead to an excessive incidence of ISR [8–10]. In addition, the medical cost for cardiac patients could increase because of the usage of multiple stents [11]. Previous reports also indicated that stent overlap was associated with major adverse cardiac events (MACE) [2, 12, 13].

However, recent clinical reports have shown that overlapping latest generation of DES is safer and more efficient, compared to early-generation DES [12, 14]. Moreover, new stent designs with increasing length are emerging as an alternative tool to reduce the needs of overlapping multiple stents, during the percutaneous treatment of coronary artery disease (CAD). Therefore, to treat the long lesion during PCI became feasible [13, 15, 16]. In fact, one single newer-generation DES with 38 mm in length has been applied into clinical use for some specific patients. From a clinical and economic perspective, the utilization of single stents can significantly reduce the practice of overlapping stents, resulting in lower ISR, shorter operation time, and less cost. However, for long lesion treatment, single stents need to provide superior transport and compliance and a reduced elastic retraction, as well as an excellent longitudinal strength, which are all relevant to their design and mechanical properties [14, 17, 18].

Until now, there is no sufficient data on the mechanical properties of long stents applied for a long lesion in former studies. Therefore, the goal of the present work was to compare the mechanical performances of the existing DES with 38 mm length, which gives the cardiologists a better understanding of the performance of the current market available DES. Here, we evaluated the crossing ability, compliance, elastic recoil, and longitudinal strength of the four popular stents with 38 mm length being used in current clinical setting.

2. Materials and Methods

2.1. Samples. The stents with 38 mm length from XIENCE Xpedition (X-stent) (Abbott, US), SYNERGY (S-stent) (Boston Scientific, US), FIREHAWK (F-stent) (Microport, China) and HELIOS (H-stent) (HELIOS, China) were collected. The detailed parameters of the collected stents are presented in Table 1. The size of four stents was $3.0 * 38$ mm, which was defined as a long stent. The X-stent, F-stent, and H-stents were made by cobalt-chromium alloy (CoCr), and the metal material of S-stent was platinum-chromium alloy (PtCr).

2.2. The Method to Test the Crossing Ability. The test of crossing ability is based on the standard of YY/T 0663.2-2016, which is from the People's Republic of China Pharmaceutical Industry Standard. We used the push tester (resolution 0.001 mN) and plane vessel model with three curves as test tools. We advanced the stent catheter system through three curves (bending radius from proximal to distal: 16 mm, 12 mm, and 9 mm) in 15 mm/s speed and pulled back to the

initial. The resistance force was measured, and the maximal value was used to evaluate the crossing ability.

2.3. The Method of the Compliance Test. The test of compliance met with the standard of YY/T 0663.2-2016. Bending test mold (cylindrical gauge) and image measuring instrument were used as the testing tools. For the compliance of stent, the stent was expanded with NP (nominal pressure, stent diameter D1 was measured) and bended along a 16 mm diameter cylinder (stent diameter D2 was measured). The reduced stent diameter %= (D1-D2)/D1 * 100% could indicate the compliance of the stent.

2.4. The Test of Elastic Recoil. In this trial, same standard as the compliance test standard was employed. Using a vernier caliper, we measured the stent diameter (ER-D1) when the stent was expanded with NP and held the pump pressure. We then measured the stent diameter (ER-D2) when the pump was released. ER-D1 and ER-D2 was defined as the average of detected diameters in the proximal, middle, and distal location of the stent, which were measured at a different state. The elastic recoil %= (ER-D1-ER-D2)/ER-D1 * 100%.

2.5. The Test for Longitudinal Strength. For longitudinal strength, the stent was expanded with NP and compressed by using a machine (Instron5943) with 0.1 mm/s speed from 0 N up to 0.49 N force, and the maximal compressed stent length was measured. The less compressed stent length indicated better longitudinal strength.

2.6. Statistic Analysis. Quantitative variables that follow a normal distribution were expressed as mean ± standard deviation or abnormal distribution expressed as median (range). Qualitative variables were analyzed as statistical significance level of p value less than 0.05. Comparisons among more than three groups were performed with One-way ANOVA or nonparametric analysis followed with multiple comparisons test. All statistical analyzes were performed using Graph Prism7.0.

3. Results

The detailed parameters of the enrolled stents were presented in Table 1. The size of four kinds of stents was $3.0 * 38$ mm, which was defined as one kind of long stents. In the crossing ability test, when the different stents were pushed and pulled back in 15 mm/s speed (Figure 1(a)), the average resistance force was recorded. In general, a lower resistant force indicates a better crossing ability. In this test, the average resistant force was 923.23 mN, 1066.66 mN, 1900.00 mN, and 1766.66 mN for the X-stent, S-stent, F-stent, and H-stent, respectively. When we compared the average resistance force among the four groups, it clearly showed that the F-stent generated highest resistance force, and there was a significant difference compared with this from X-stent groups ($p < 0.05$) (Figure 1(b)). Furthermore,

TABLE 1: The detailed information of the stents with 38 mm length from a different source.

Test item	Crossing ability + compliance + elastic recoil + longitudinal strength			
Brand	Abbott	Boston Scientific	Microport	HELIOS
Type	XIENCE Xpedition	SYNERGY	FIREHAWK	HELIOS
Size	3.0 * 38	3.0 * 38	3.0 * 38	3.0 * 38
Sample size	3	3	3	3

(a)

(b)
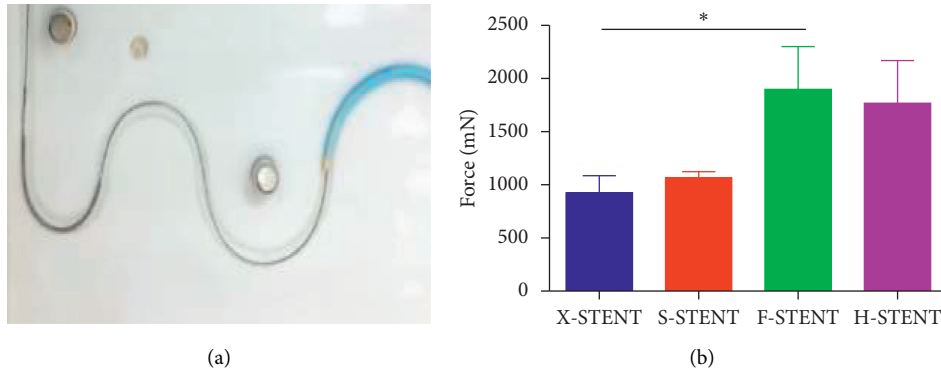
FIGURE 1: The resistance force of the stents in the test of crossing ability. The crossing ability test of the stents was completed by using a catheter system (a). In this test, the resistance force was compared among stents from the X-stent, S-stent, F-stent, and H-stent (b). $^{*}p < 0.05$.

(a)

(b)
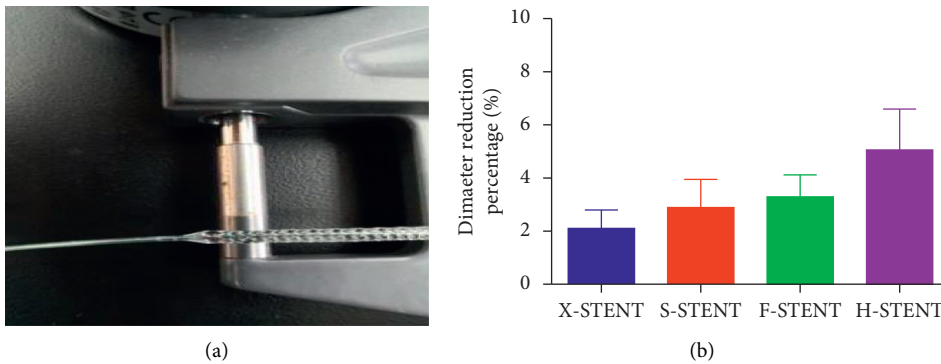
FIGURE 2: The percentage of stent diameter reduction of the stents in the compliance test. Diameters of the stents were measured both before and after the stent was bended along a 16 mm diameter cylinder (a). The reduced stent diameter% was compared among stents from the X-stent, S-stent, F-stent, and H-stent (b).

the resistant force among the stents from XIENCE Xpedition, SYNERGY, and HELIOS was similar, which indicated better crossing ability in these three groups.

In Figure 2(a), we presented the curved stent in the standard angle for testing the compliance. The ratio of reduced stent diameter reduction is relevant to the ability of the compliance. Often smaller ration implies better compliance. In this test, the average ratio of stent diameter reduction in the X-stent, S-stent, F-stent, or H-stent stents was 2.11%, 2.89%, 3.30%, and 5.06%, respectively. According to the data, it seems that X-stents hold a lower ratio of stent diameter reduction. However, there was no statistical difference when we compared the ratio of stent diameter reduction among the four groups (Figure 2(b)).

In addition, a relatively smaller elastic recoil percentage is corresponding to an excellent stent performance

(Figure 3(a)). The percentage of elastic recoil of stents from the X-stent, S-stent, F-stent, or H-stent was 2.62%, 1.16%, 3.66%, and 4.19%, respectively. Further statistical analysis indicated that the percentage of elastic recoil of stents from the S-stent was significantly lower than that from the F-stent and H-stent (Figure 3(b)). However, there was no difference between the X-stent and S-stent (Figure 3(b)), which indicates comparable performance between these two kinds of stents.

Notably, longitudinal strength is an important indicator for the mechanical performances of DES. After being compressed by Instron 5934 and expanded by NP, the average maximal compressed stent length of X-stent, S-stent, F-stent, or H-stent was 1.86 mm, 18.6 mm, 7.65 mm, and 3.18 mm, respectively (Figure 4(a) and 4(b)). Obviously, the stents from the X-stent and H-stent had less displacement

(a)   (b)
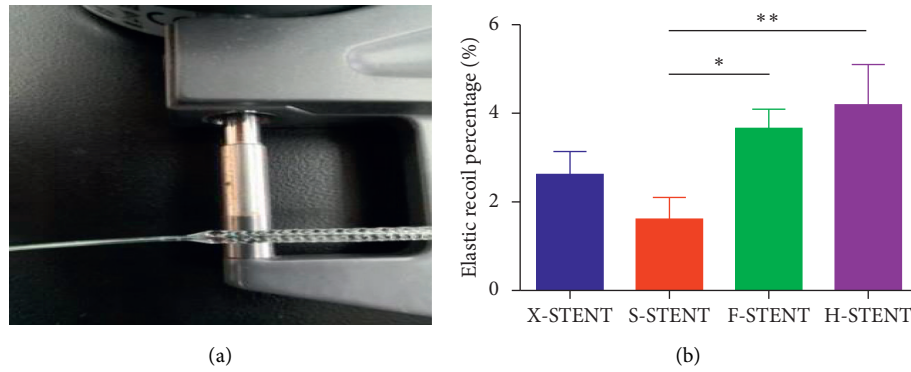
FIGURE 3: The percentage of elastic recoil of the stents. Using a vernier caliper, the stent diameter was measured before and after the pump releasing (a). The elastic recoil% was compared among stents from the X-stent, S-stent, F-stent, and H-stent (b). $*p < 0.05$; $**p < 0.005$.

(a)   (b)

(c)
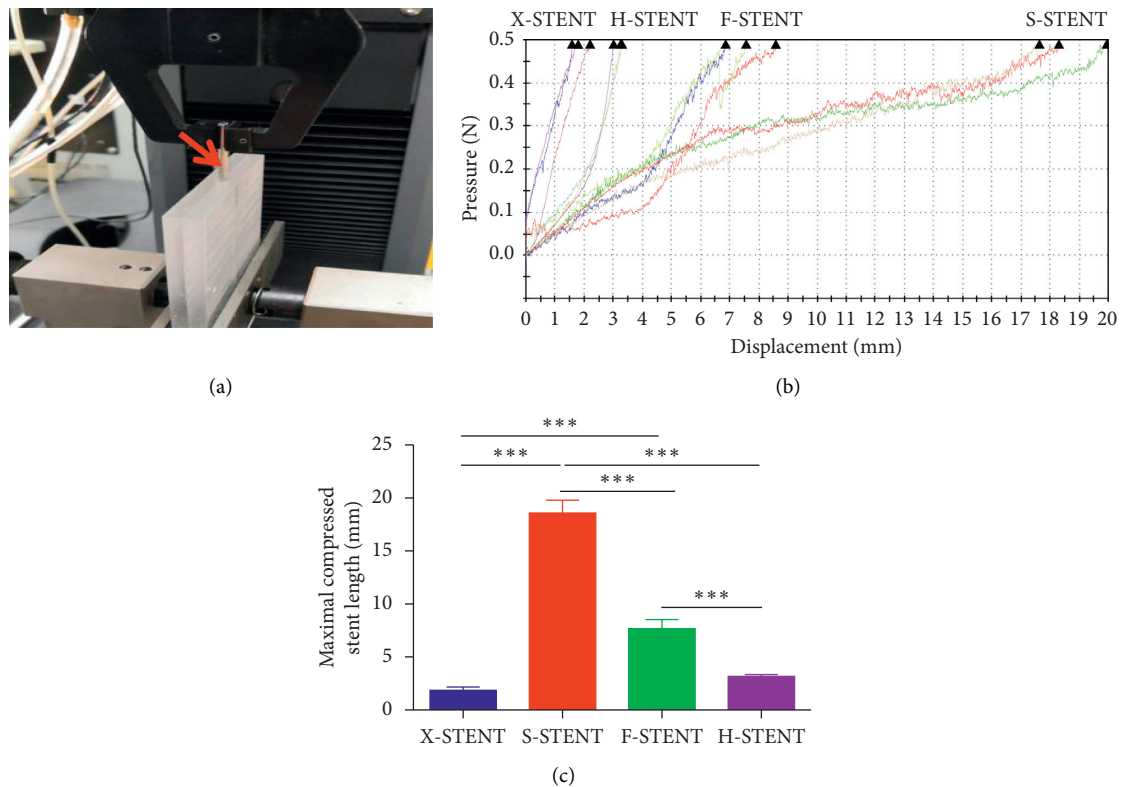
FIGURE 4: The maximal compressed stent length of the stents in the longitudinal strength test. Model 5943 Materials Testing was used in the tested of longitudinal strength (a), and the compressed stent length from different source were measured under pressure (b). The maximal compressed stent length was compared among stents from the X-stent, S-stent, F-stent, and H-stent (c). $***p < 0.001$.

under pressure compared with the S-stent and F-stent. This result demonstrated that both X-stent and H-stent had superb longitudinal strength ($p < 0.0001$) (Figure 4(c)). Surprisingly, S-stents presented the most displacement. (Figure 4(c)).

4. Discussion

It has been investigated that high incidence of major adverse cardiovascular events is associated with lesion length. Coronary stenting is a milestone in the treatment of CAD

[19]. However, due to the complicated properties of the long lesions, including distortion, calcification, and angle formation, it has high demand in the surgeon's skill and the overall performance of the stent. Many animal and human experiments have showcased that materials and design of stents can have an important impact on postoperative arterial intimal thickening, which is related to the formation of in-stent restenosis [20–23]. Therefore, focusing on the mechanical properties of the stent is important for reducing adverse events after PCI. With the development of stents design, the newly adopted a stent with 38 mm may

potentially solve many problems in treating long lesions. However, in the current market, a variety of different 38 mm stents bring doctors some troubles in their choices. Hence, this study provides a much-needed guidance for cardiologists to choose the best stents. Here, we focused on assessing the mechanical properties of the DES with 38 mm length available in the market, to assist clinicians select the proper stents for a long lesion, which can reduce adverse events after PCI.

Due to its complexity, the long lesion is often associated with the vessel calcification, vascular circuity, and repeated operation on the stents. Especially, the application of balloons in the procedure of PCI is frequent for long lesion treatment. Better longitudinal strength of stents could prevent the stent deformation during the operated process. In our present study, mechanical parameters like crossing ability, compliance, elastic recoil, and longitudinal strength have been evaluated for those four long stents with 38 mm length, which may provide some reference for clinicians when choosing the stents for application in patients. In this study, X-stent performed significantly better than F-stent in the test of crossing ability. In terms of compliance, X-stent was better than other DES, although there was no significant difference. Thus, X-stent could be listed as one of the top choices when the long lesion companied with severe vessel calcification and vascular circuity. S-stent showed significantly improved percentage of elastic recoil when compared to F-stent and H-stent, but was no significant compared with X-stent. As to the longitudinal strength test, stents from the X-stent achieved an overwhelming advantage compared with the other three, which indicated that X-stent could be the best choice when the PCI operation needs multiple application of balloon. Inevitably, there are still some limitations in this study. The sample size of this study is relatively limited. Also, instead of assessing all mechanical parameters of DES, only important ones were tested and compared. Moreover, the assessment in this study was only performed *in vitro*, without verification from *in vivo* or human trials. Thus, further larger-scale studies with more comprehensive data are essential to provide a better insight for clinicians.

5. Conclusion

Mechanical performances of stent should be considered as one of the major factors when clinicians perform the operation of stent. Our present study compared the performance of the four major 38 mm long stents, which may provide a direct index for accurately clinical application. Clinicians could make more accurate decision on the choice of stent as well as the following treatment when combining the detailed mechanical performance of stent and the patient's condition.

Abbreviations

PCI: Percutaneous coronary intervention
BMS: Bare metal stents
ISR: In-stent restenosis

DES: Drug-eluting stent
MACE: Major adverse cardiac events
CAD: Coronary artery disease.

Data Availability

The data used to support the findings of this study are included within the article.

Conflicts of Interest

The authors declare that they have no conflicts of interest.

Authors' Contributions

Xiaoting Yue and Jiacheng Guo contributed equally to this work.

Acknowledgments

References

[1] C. Bauters, E. Hubert, A. Prat et al., "Predictors of restenosis after coronary stent implantation," *Journal of the American College of Cardiology*, vol. 31, no. 6, pp. 1291–1298, 1998.

[2] M. Taniwaki, G. G. Stefanini, S. Silber et al., "4 year clinical outcomes and predictors of repeat revascularization in patients treated with new-generation drug-eluting stents," *Journal of the American College of Cardiology*, vol. 63, no. 16, pp. 1617–1625, 2014.

[3] S. Cassese, R. A. Byrne, T. Tada et al., "Incidence and predictors of restenosis after coronary stenting in 10 004 patients with surveillance angiography," *Heart*, vol. 100, no. 2, pp. 153–159, 2014.

[4] A. Kastrati, A. Schömig, R. Dietz, F. J. Neumann, and G. Richardt, "Time course of restenosis during the first year after emergency coronary stenting," *Circulation*, vol. 87, no. 5, pp. 1498–1505, 1993.

[5] K. H. Bønaa, J. Mannsverk, R. Wiseth et al., "Drug-eluting or bare-metal stents for coronary artery disease," *The New England Journal of Medicine*, vol. 375, no. 13, pp. 1242–1252, 2016.

[6] D. G. Kokkinidis, S. W. Waldo, and E. J. Armstrong, "Treatment of coronary artery in-stent restenosis," *Expert Review of Cardiovascular Therapy*, vol. 15, no. 3, pp. 191–202, 2017.

[7] B. Xu, R. L. Gao, R. Y. Zhang et al., "Efficacy and safety of FIREHAWK(R) abluminal groove filled biodegradable polymer sirolimus-eluting stents for the treatment of long coronary lesions: nine-month angiographic and one-year

clinical results from TARGET I trial long cohort," *Chinese Medical Journal*, vol. 126, pp. 1026–1032, 2013.

[8] L. Räber, P. Jüni, L. Löffel et al., "Impact of stent overlap on angiographic and long-term clinical outcome in patients undergoing drug-eluting stent implantation," *Journal of the American College of Cardiology*, vol. 55, no. 12, pp. 1178–1188, 2010.

[9] R. M. Minutello, S. Bhagan, D. Feldman, A. Sharma, M. K. Hong, and S. C. Wong, "Angiographic pattern of restenosis following implantation of overlapping sirolimus-eluting (Cypher) stents," *The American Journal of Cardiology*, vol. 97, no. 4, pp. 499–501, 2006.

[10] F. Burzotta, M. Siviglia, L. Altamura et al., "Outcome of overlapping heterogenous drug-eluting stents and of overlapping drug-eluting and bare metal stents," *The American Journal of Cardiology*, vol. 99, no. 3, pp. 364–368, 2007.

[11] L. Venkitachalam, Y. Lei, J. M. Stolker et al., "Clinical and economic outcomes of liberal versus selective drug-eluting stent use," *Circulation*, vol. 124, no. 9, pp. 1028–1037, 2011.

[12] C. E. Beale and J. Dawn Abbott, "Drug eluting stents for very long lesions: go long, but know the risks," *Catheterization and Cardiovascular Interventions*, vol. 89, no. 6, pp. 992-993, 2017.

[13] Y. Honda, T. Muramatsu, Y. Ito et al., "Impact of ultra-long second-generation drug-eluting stent implantation," *Catheterization and Cardiovascular Interventions*, vol. 87, no. 2, pp. E44–E53, 2016.

[14] A. Colombo, G. Stankovic, and J. W. Moses, "Selection of coronary stents," *Journal of the American College of Cardiology*, vol. 40, no. 6, pp. 1021–1033, 2002.

[15] I. J. Choi, Y.-S. Koh, S. Lim et al., "Impact of the stent length on long-term clinical outcomes following newer-generation drug-eluting stent implantation," *The American Journal of Cardiology*, vol. 113, no. 3, pp. 457–464, 2014.

[16] G. Bouras, S. Jhamnani, V. G. Ng et al., "Clinical outcomes after PCI treatment of very long lesions with the XIENCE V everolimus eluting stent; Pooled analysis from the SPIRIT and XIENCE V USA prospective multicenter trials," *Catheterization and Cardiovascular Interventions*, vol. 89, no. 6, pp. 984–991, 2017.

[17] P. Chichareon, Y. Katagiri, T. Asano et al., "Mechanical properties and performances of contemporary drug-eluting stent: focus on the metallic backbone," *Expert Review of Medical Devices*, vol. 16, no. 3, pp. 211–228, 2019.

[18] A. Sakamoto, S. Torii, H. Jinnouchi, R. Virmani, and A. V. Finn, "Histopathologic and physiologic effect of overlapping vs single coronary stents: impact of stent evolution," *Expert Review of Medical Devices*, vol. 15, no. 9, pp. 665–682, 2018.

[19] U. Sigwart, J. Puel, V. Mirkovitch, F. Joffre, and L. Kappenberger, "Intravascular stents to prevent occlusion and Re-stenosis after transluminal angioplasty," *New England Journal of Medicine*, vol. 316, no. 12, pp. 701–706, 1987.

[20] C. Rogers and E. R. Edelman, "Endovascular stent design dictates experimental restenosis and thrombosis," *Circulation*, vol. 91, no. 12, pp. 2995–3001, 1995.

[21] J. M. Garasic, E. R. Edelman, J. C. Squire, P. Seifert, M. S. Williams, and C. Rogers, "Stent and artery geometry determine intimal thickening independent of arterial injury," *Circulation*, vol. 101, no. 7, pp. 812–818, 2000.

[22] R. Hoffmann, C. Jansen, A. Konig et al., "Stent design related neointimal tissue proliferation in human coronary arteries; an intravascular ultrasound study," *European Heart Journal*, vol. 22, no. 21, pp. 2007–2014, 2001.

[23] R. Yamada, H. Okura, T. Kume et al., "Impact of stent platform on longitudinal stent deformation: an in vivo frequency domain optical coherence tomography study," *Cardiovascular Intervention and Therapeutics*, vol. 32, no. 3, pp. 199–205, 2017.

Research Article

Strontium/Chitosan/Hydroxyapatite/Norcantharidin Composite That Inhibits Osteosarcoma and Promotes Osteogenesis In Vitro

Zhipeng Huang, Haoyuan Sun, Yang Lu, Fengnian Zhao, Chang Liu, Qinglong Wang, Changming Zheng, Renpei Lu, and Keguan Song ⬥

The First Affiliated Hospital of Harbin Medical University, No. 23 Post Street, Nangang District, Harbin, Heilongjiang, China

Correspondence should be addressed to Keguan Song; songkeguan@sohu.com

Hydroxyapatite can deliver drugs, and its composite material is capable of repairing bone defects in tumors. This study was conducted to evaluate the effect of composite materials on tumor growth inhibition and bone growth induction. Composites containing drug delivery compounds were synthesized by coprecipitation and freeze-drying and then characterized by scanning electron microscopy (SEM), X-ray diffraction (XRD), and Fourier-transform infrared spectroscopy (FTIR). In addition, the effect of hydroxyapatite nanoparticles (nano-SHAP) on proliferation of an osteosarcoma cell line (MG-63) and an osteoblast cell line (MC3T3-E1) was evaluated, and its mechanism was studied. The use of nano-SHAP alone did not affect the proliferation of normal cell lines. However, nanoparticles containing different amounts of norcantharidin in the composite materials and had different inhibitory effects on osteosarcoma and different effects on osteoblasts. And, with the increase of the content of norcantharidin, the antitumor performance of the composite has been enhanced. In summary, the nano-SHAP system developed in this study is a drug delivery material that can inhibit the growth of tumors and induce the proliferation of osteoblasts.

1. Introduction

Osteosarcoma (OS) is the most common primary malignant solid tumor in humans between the ages of 10 and 25 [1]. It is characterized mainly by the destruction of and recurrence in local tissue and is prone to distant metastasis. The widely accepted treatment for OS, which includes routine surgical resection and neoadjuvant chemotherapy, can improve the short-term survival rate to 60–70% [2]. However, tumor cells can remain in the area around the tumor resection site after surgery, resulting in high recurrence and bone destruction. Adjuvant chemotherapy plays an important role in killing the residual tumor cells and preventing tumor metastasis and recurrence [3]. In addition, it is common knowledge that bone defects need to be repaired using repair techniques such as allogeneic bone transplantation, iliac bone grafts, and irradiation bone grafts. However, there are still disadvantages in these technologies. For example, allogeneic bone is one of the most commonly used materials used for repairing tumor-induced bone defects, but it has no antitumor effect and is associated with the spread of infectious diseases and immune response [4]. Therefore, biocompatible biomaterials have the potential to be anticancer agents and to repair defects.

Composite materials, which comprise two or more excellent biomaterials, exhibit the properties of those materials. In recent years, composite materials composed of inorganic and organic components have attracted increasing attention. Depending on the characteristics of the components, the composites are used in catalysts, genes, and drug carriers [5, 6], for photodynamic and photothermal effects [7], and for their antibacterial properties [8, 9]. The organic components are important for modifying the inorganic materials, improving biocompatibility, escaping mononuclear cell phagocytic systems, and improving the therapeutic effects of the composite [10]. The cited studies have shown that composite materials will have a wide range of

applications in the biomedical field and in many different scientific fields in the future.

Inorganic salts and carbohydrates play a crucial role in antitumor, bone regeneration, and biomineralization. Chitosan (CS) is the only basic aminopolysaccharide found in natural polysaccharides. It is widely used in many fields because of its biocompatible, biodegradable, and good antibacterial and antioxidant properties. CS can be used to absorb metal ions or other chemicals which is used to resist tumors [11]. Nanohydroxyapatite (nHAP) is the main inorganic component of human bones and teeth, accounting for 50–70% of human bone. Due to its good biocompatibility, biological activity, and osteoinductivity, nHAP added to the CS material can increase mechanical performance and mimic the natural structure of bone while maintaining biocompatibility [12]. In addition, studies have shown that CS/nHAP materials increase bone regeneration primarily by upregulating osteogenic genes and promoting mesenchymal stem cell (MSC) differentiation mineralization in vivo [13, 14]. Due to the advantages of good stability, biocompatibility, bone conductivity, and bone induction, CS/nHAP materials have been developed as osteogenic materials.

Strontium (Sr) ions not only promote the formation of new bone but also inhibit bone resorption [15], which have positive effects on promoting osteogenic differentiation of MSCs, preventing the proliferation of osteoclasts [16], and increasing the osteoinductivity of the composite. Marie et al. [17] reported that low-dose Sr^{2+} can accelerate bone formation and increase bone mass in animals. In the study by Lei et al. [15], SrHAP/CS was shown to have excellent cell compatibility and that it supports adhesion, diffusion, and proliferation of human bone marrow stromal cells (hBMSCs). Sr^{2+} released by the material contributed to osteogenic differentiation, and the presence of Sr in the SrHAP/CS material enhanced alkaline phosphatase (ALP) activity, extracellular matrix (ECM) mineralization, and the expression of osteogenesis-related genes Col-1 and ALP. Furthermore, the percentage of Sr in SrHAP had a large effect on ALP activity. ALP activity gradually increased as the Sr/Ca ratio in SrHAP increased and reached the maximum when the Sr/Ca ratio was 1 : 1. A high dose of Sr may lead to bone mineralization defects and even cause bone abnormalities.

Norcantharidin (NCTD) (7-oxabicyclo[2.2.1]heptane-2,3-dicarboxylic anhydride) is a new anticancer drug extracted and synthesized from traditional Chinese medicine. It has remarkable anti-cancer properties and is the only antitumor drug that can elevate white blood cell counts. Previous studies have demonstrated that NCTD suppresses the growth of numerous cancer cell lines, including oral cancer [18], hepatoma [19], and prostate cancer [20], via apoptosis, autophagy, and cell cycle arrest. Demethylcantharidin tablets have been used in the clinical treatment of hepatocellular, esophageal, and gastric cancer and leukemia [21]. It is reported that NCTD can play an anti-osteosarcoma role in many ways. NCTD can inhibit the proliferation of osteosarcoma cells by blocking the Akt/mTOR signal transduction pathway and inducing G2/M cell cycle arrest in 143B and SJSA osteosarcoma cells in a dose- and time-

dependent manner. At the same time, NCTD led to the upregulation of cleaved caspase-3 and an increase in the downstream target cleaved PARP, which suggested that the extrinsic pathway may also be involved in NCTD-induced cell apoptosis [22]. By evaluating the effects of NCTD on OS cell lines (MG63 and HOS) in vitro and in vivo, we found that NCTD can inhibit cell cycle and induce apoptosis of human OS cells. These effects are mediated by autophagy induction, triggering ER stress and inactivation of the c-Met/Akt/mTOR pathway [23]. It works when the proliferation and apoptosis of normal cells are out of balance by inhibiting and then inducing apoptosis of tumor cells [24]. Studies have shown that $5 \mu M$ of cantharidin kills nearly 45% of viable tumor cells [25]. In addition, $10 \mu M$ of cantharidin was used to treat cells for different time periods and then western blot was used to analyze protein levels. Cantharidin increased the levels of p21 and phospho-p53 but decreased the levels of cyclin E and Cdc25c, which cause G0/G1 arrest [26]. NCTD effectively induces TNBC cell senescence and cell cycle arrest in vitro, accompanied by a decrease in phosphorylation of Akt and ERK1/2 and an increase in p21 and p16 [27]. At present, the most common route of administration is oral administration, which can lead to adverse reactions, such as nausea and vomiting. However, we have not found any reports that NCTD can be used as a composite biomaterial with anticancer effect in human body. However, to the best of our knowledge, few biomaterials can effectively kill residual tumor cells and repair bone defects after OS surgery. For the first time, we tried to incorporate NCTD into biological composite materials, which not only can reduce the systemic side effects caused by high blood drug concentration but also provide a good method and attempt for anti-osteosarcoma and osteogenesis.

In this study, we developed a novel strontium/chitosan/hydroxyapatite/norcantharidin (Sr/CS/HAP/NCTD or SCHN) composite that has certain osteoinductive properties and a significant inhibitory effect on the proliferation of OS cells. Experiments demonstrated that the inhibitory effect induced apoptosis by upregulating the expression of pro-apoptotic genes. In addition, the composite material reduced the osteoclastic activity of tumor cells by downregulating osteoclast-related genes. The composite shows good potential for treating OS in situ and repairing tumor-related bone defects.

2. Materials and Methods

2.1. Synthesis of Materials. SCHN composites were prepared by the method of in situ precipitation. The specific methods are as follows: three grams of CS powder (2% w/v; Sigma Aldrich, St. Louis, Mo, USA) was dissolved in 2% acetic acid solution and mechanical mixed at 60°C until the solution was clarified. $SrCl_2$ 42 g and $Ca(OH)_2$ 12 g were added into deionized water in proper sequence. After stirring and mixing smoothly, 30 g KH_2PO_4 was added slowly to keep the ratio of (Ca + Sr)/P at 1.67 and pH at 10, which was mixed for 24 hours. The above two solutions were mixed and divided into four parts, adding 0 g, 5/6 g, 5/3 g, and 5/2 g norcantharidin, respectively. The above liquids were fully

mixed and added to 24-hole plate which was freeze-dried overnight in a freeze-dryer at -60°C. The mixtures were marked as Strontium/chitosan/hydroxyapatite/norcantharidin0, Strontium/chitosan/hydroxyapatite/norcantharidin1, Strontium/chitosan/hydroxyapatite/norcantharidin2, and Strontium/chitosan/hydroxyapatite/norcantharidin3. To facilitate the marking, we refer to above materials as Q0, Q1, Q2, and Q3.

2.2. Characterization of Materials

2.2.1. Surface Microstructure.
The surface microstructure and morphology of the samples were examined using a field-emission scanning electron microscope (FE-SEM, Quanta 200, Thermo Fisher Scientific, Waltham, MA, USA) at an acceleration voltage of 20 kV. All samples were plated with Au for 30 s before undergoing SEM. In addition, the microscope was equipped with an energy-dispersive X-ray (EDX) spectrometer to perform elemental analysis of the composite.

2.2.2. Chemical Composition.
The chemical composition of the composite was obtained using an FTIR spectrometer (Nicolet 6700, Thermo Fisher Scientific). The spectra of the Q0–Q3 materials were recorded using the KBr particle method with a 4000–$400\,\text{cm}^{-1}$ FTIR spectrophotometer. Each infrared spectrum was the average of 32 scans collected at $4\,\text{cm}^{-1}$ resolution at 25°C over a range of 400–$4000\,\text{cm}^{-1}$.

2.2.3. Elemental Analysis.
The elemental analysis of the crystal phase exhibited on the powder was performed via X-ray diffraction (XRD) with a stepwise scanning diffractometer (XPS, Rigaku, Tokyo, Japan) equipped with Cu Kα radiation target generated at 40 kV and 30 mA. The data set was collected in a 2θ range of 10°–70° at 0.02° per step.

2.2.4. Swelling Behavior.
The swelling behavior of the materials was evaluated using conventional methods [28]. Briefly, the dry weight of the material was recorded. Then, the material was immersed in 37°C phosphate-buffered saline (PBS), the wet weight was recorded for 1 hour and 24 hours, and the surface moisture was removed using filter paper. The expansion ratio was calculated using the following equation:

$$\text{Swell ratio} = \frac{(\text{Wet weight} - \text{dry weight})}{\text{Dry weight}}. \quad (1)$$

2.2.5. Hemolysis Test.
The method used had been reported previously [29]. Briefly, blood-containing EDTA was taken from volunteers and diluted to a blood : physiological saline ratio of 4 : 5. After 15 mg of the different composite materials was placed in 1 ml of normal saline, the mixture was incubated at 37°C for 30 min. Deionized water and PBS (each 1 ml) were added as positive and negative controls, respectively, followed by the addition of $200\,\mu$l of diluted blood

to each sample. The mixture was incubated in a constant temperature water bath at 37°C for 60 minutes. Finally, $100\,\mu$l of the supernatant was transferred to a 96-well plate after centrifugation. The optical density (OD) was measured at 545 nm using a microplate reader.

2.3. Biological Properties of Materials

2.3.1. Cell Proliferation and Toxicity.
CCK-8 was used to measure the proliferation of osteogenic MC3T3-E1 cells and osteosarcoma MG-63 cells in the environment of composite immersion solution. In brief, $100\,\mu$l of MC3T3-E1 cells or MG-63 cell suspension was seeded at a density of 2×10^4 cells/ml in 96-well plates separately; culture medium and solution immersed in NCTD composites with different concentrations are added in proper order, which are cultured at 37°C. After 1, 4, and 7 days of incubation, the original culture solution was replaced by 10% CCK-8 culture solution in order to measure the OD value at 450 nm. The cell viability was calculated as follows:

$$\text{cell survival rate} = \left[\frac{A_s - A_b}{A_c - A_b}\right] \times 100\%, \quad (2)$$

where A_s is the experimental well, A_c is the control well, and A_b is the blank well. All experiments were performed in triplicate.

2.3.2. Apoptosis and Necrosis.
The OS cell suspension ($500\,\mu$l) was seeded at a density of 2×10^5 cells/ml for 2 days and detected using a CYTOMICS FC 500 MCL flow cytometer (Beckman Coulter, Brea, CA, USA). Briefly, after the extract of the composite material was added to the cells, the supernatant and adherent cells were collected and centrifuged at 1000 rpm for 5 min. The cell pellet was resuspended in $100\,\mu$l of PBS and incubated with $10\,\mu$l of Annexin V-FITC and $5\,\mu$l of PI labeling solution for 20 min at 24°C–28°C in the dark. Finally, the cells were analyzed using flow cytometry, and the results were analyzed via Cytomics FC500 flow cytometry CXP analysis.

2.3.3. Real-Time Polymerase Chain Reaction (RT-PCR).
Expression of apoptosis- and osteoblast-associated genes was assessed using RT-PCR. MG-63 cells and MC3T3-E1 cells, respectively, were cultured with the composite extract for 3 days. Total cellular RNA was isolated using TRIzol. The RNA was separated into an aqueous phase by the addition of chloroform. The colorless upper aqueous phase was then transferred to a new 1.5 ml tube to which isopropanol was added to precipitate the RNA. Finally, the RNA was washed with 75% ethanol and dissolved in enzyme-free water. RNA concentration was determined using a NanoDrop™ 2000 spectrophotometer (Thermo Fisher Scientific). RNA from each sample was reverse transcribed into complementary DNA (cDNA) using a PrimeScript™ RT reagent kit (Takara Bio Inc., Kusatsu, Japan) according to the manufacturer's instructions. Gene expression level of ALP, runt-associated transcription factor 2 (Runx2), osteocalcin (OCN),

osteopontin (OPN), caspase-3 (CASP3), caspase-9 (CASP9), and matrix metallopeptidase 9 (MMP9) were evaluated by using iTap Universal SYBR® Green Spermix (BIO-RAD). The relative expression level of each target gene was then calculated using the $2^{-\Delta\Delta CT}$ method. The relative mRNA expression level of each gene was normalized to that of GAPDH.

2.4. Statistical Analysis. All data were recorded as mean-±standard deviation. One-way analysis of variance (ANOVA) was performed using GraphPad Prism 6.0 (GraphPad Software, San Diego, CA, USA). $p < 0.05$ was considered as significant difference.

3. Results and Discussion

3.1. Composite Properties. In situ precipitation is a common method for preparing Sr/CS/HAP materials. In situ CS/HAP composites have better mechanical and biological properties than the physically prepared materials. The addition of Sr can enhance the cell adhesion [30] and the expression of osteogenesis-related genes [31] and promote osteoblast differentiation [15]. More importantly, the addition of Sr enhances the strength of the composites and improves the solubility of hydroxyapatite [32]. The various shapes of the HAP particles in the CS/HAP composite and the size of the composite depend on the processing conditions. Figures 1(a)–1(d) shows the morphology of the synthesized nanoparticles. The SEM images show that the materials were porous, that the pore size of the Q1, Q2, and Q3 composite materials was smaller than that of Q0, that the materials were made of small needle-like or plate-like crystals, and that the structure changed with the addition of NCTD. The materials had an irregular three-dimensional (3D) structure, and their pores were tightly connected to each other. The 3D environment may enhance cell-cell interaction and promote cell biological activity [33, 34]. Thus, the prepared material may be suitable for bone repair. Figure 1(e) shows the energy-dispersive X-ray (EDX) spectrum of the Sr/HAP nanoparticles with the characteristic bands of Ca and Sr. The (Sr + Ca)/P ratio was about 1.66, which is similar to that of standard HAP. These minerals are key components of bone and tooth tissue.

3.2. Elemental Analysis of Q0, Q1, Q2, and Q3. In the XRD spectra of Q0, Q1, Q2, and Q3, a narrow and pointed peak was detected at θ values of 24.98°, 31.6°, 40.82°, and 56.38°, respectively (Figure 2), which shows that all the diffraction peaks correspond to the reflection of the composition of the material. As the concentration of NCTD increased, the diffraction spectrum lines narrowed and became sharper. The peak at 22.2° indicated an increase in crystallinity and a decrease in molecular size [35]. Meanwhile, traces of other impurities were not detected by this technique.

3.3. Chemical Composition. The functional groups contained in the composites were analyzed by FTIR. Figure 3 shows the representative FTIR spectra of the synthesized Q0 and Q1, Q2, and Q3 nanoparticles. The characteristic peaks of CS appear at 1668 and 1431 cm^{-1}, which correspond to the bands of amide-I and amide-II, and the vibrational band at 1024 cm^{-1} corresponds to $C = O$ stretching [9]. For NCTD, the band at 860 cm^{-1} is attributed to the characteristic band of OH stretching, which is also the characteristic band of HAP [36]. Compared with Q0, the tensile vibration in Q1, Q2, and Q3 was enhanced, indicating that the addition of NCTD into the material was successful.

3.4. Swelling Behavior. The swelling behavior of the material was determined by immersing the composite materials in PBS solution. Figure 4 shows that the swelling rates of the composites were different; however, the calculated differences were not significant. In addition, the swelling rates of the four materials did not change significantly during the incubation period, indicating that they were very stable. The difference in the swelling ratio among the materials, as seen in Figure 4, may be due to experimental errors in the materials.

3.5. Biocompatibility and Osteoinductivity. In this study, blood compatibility plays an important role in biological materials. Good biological materials should not cause red blood cells to rupture. In a blood compatibility test with a positive control (deionized water), a negative control (PBS), and the sample groups, the positive control caused hemolysis, with the released hemoglobin making the solution red (Figure 5(a)). After centrifugation, the red blood cells in the test tubes containing the material and the negative control were sedimented and the supernatant was clear. A small amount of the layer containing red blood cells was placed under a microscope, and no cell rupture was observed. It can be concluded that the material does not cause acute hemolysis. On the other hand, it is well known that CS and HAP possess excellent histocompatibility in bone repair. Although the addition of NCTD to materials has a good antitumor effect, it may also be toxic to normal osteoblasts. CCK-8 was used to detect the cytotoxicity of the composite to MC3T3-E1 cells. In all time intervals, Q1 and Q2 scaffolds showed little toxicity; accordingly, the OD value increased with the increase of incubation time, while the OD value of Q3 did not change significantly. In conclusion, the results indicate that the appropriate concentration of NCTD composite has good biocompatibility to bone tissue.

3.6. Antitumor and Increased Osteoblast Characteristics. To determine the optimal concentration of NCTD in the material, the cytotoxic effect of NCTD on osteosarcoma MG-63 cells and on MC3T3-E1 cells was determined using the standard CCK-8 assay. Figure 6 summarizes the cell viability of MG-63 and MC3T3-E1 cells after 1, 3, and 7 days of cultured with different NCTD concentrations. Figure 6(a) shows that, according to the CCK-8 assay, the osteoblast cells cultured in the three extract media cultured on day 1 had relatively similar absorbances as that of the control group

(a)

(b)

(c)

(d)

(e)
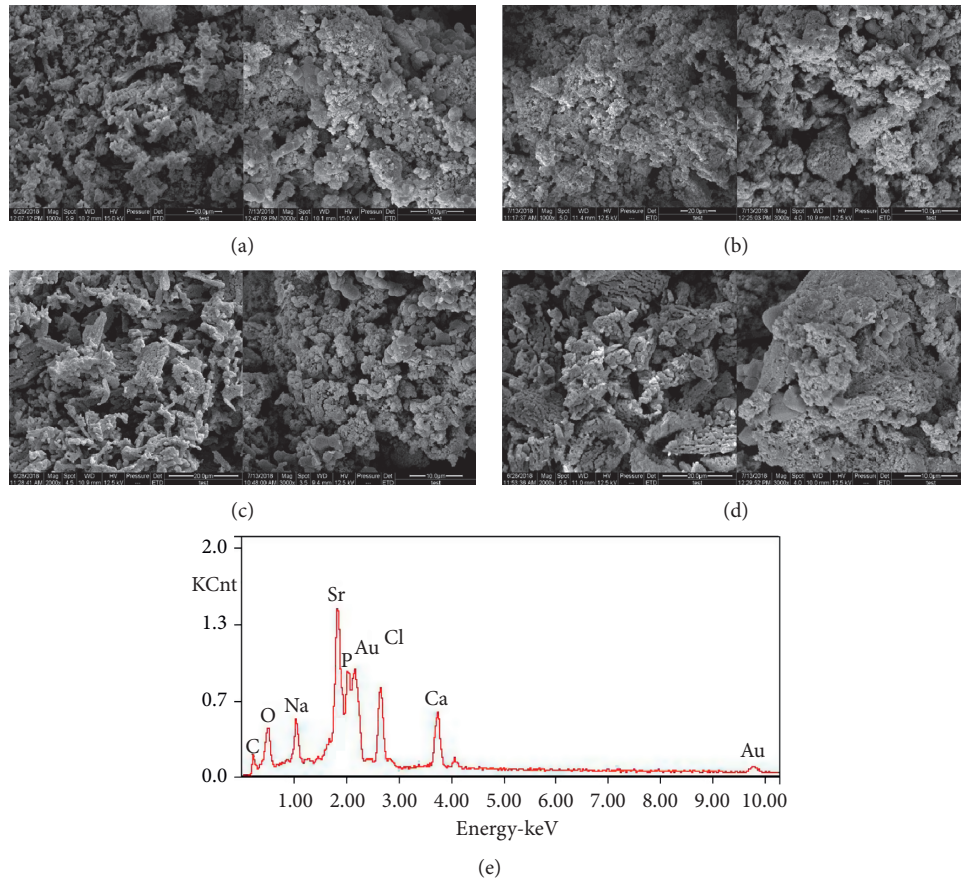
Figure 1: (a)–(d) SEM images of the materials of the Q0, Q1, Q2, and Q3 composite materials, respectively. (e) EDX spectra of the nanoparticles.
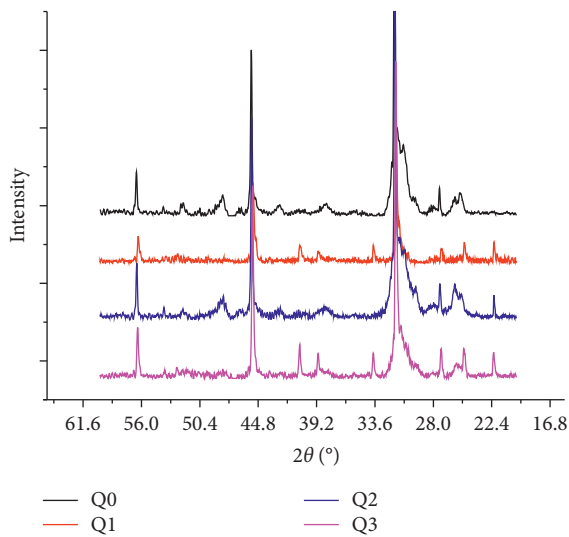
Figure 2: X-ray diffraction spectra.
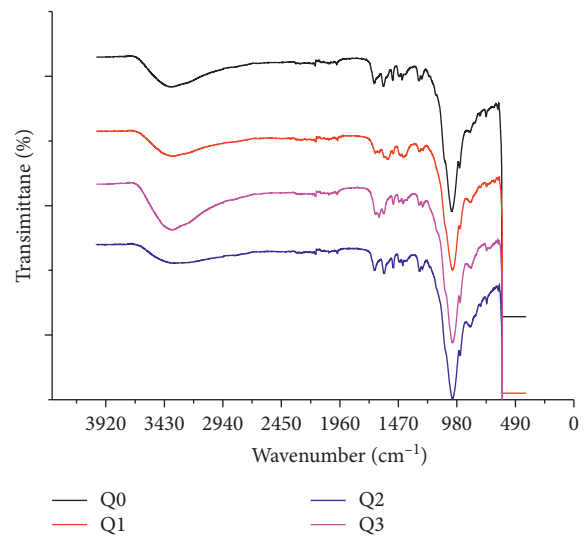
Figure 3: FTIR diffraction spectra.

(Q0) ($p > 0.05$). After day 1, the absorbance values of all groups increased, meaning that the number of live cells increased. On day 3, the OD value and number of live cells of the Q2 group increased ($p < 0.01$), and the number of live cells of the Q3 group increased ($p < 0.05$). On day 7, the OD value and number of live cells of the Q1 group increased ($p < 0.01$), and the number of live cells of the Q2 group increased ($p < 0.05$). At the same time, the absorbance values of the other composite material groups were not statistically significant ($p > 0.05$). Figure 6(b) shows the results for the
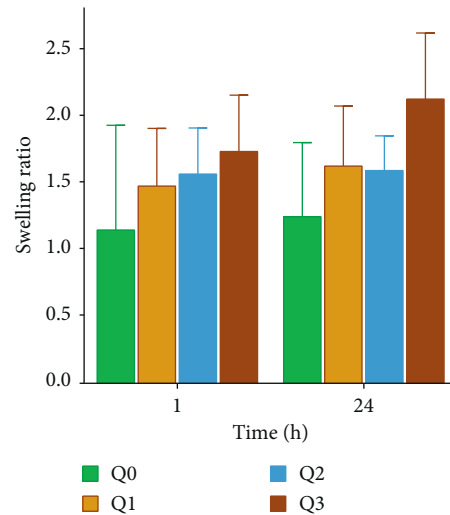
FIGURE 4: Expansion behavior of composites in PBS.

(a)

(b)
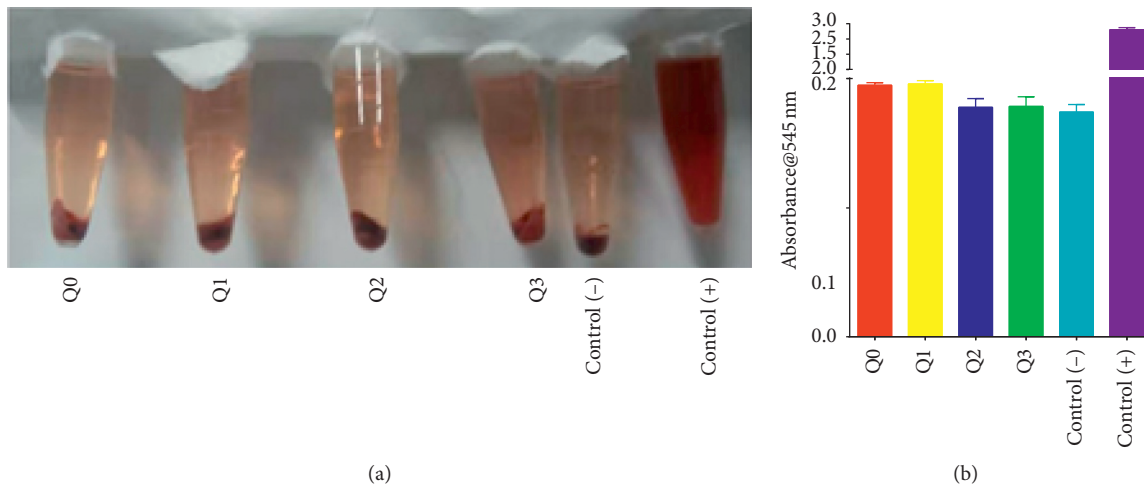
FIGURE 5: Composite hemolysis test. (a) None of the four materials caused hemolysis. (b) Supernatant of the area that underwent absorbance testing. Each value is the mean ± standard deviation of three determinations.

OS cells. The OD value and the number of live cells in the Q1, Q2, and Q3 composites gradually decreased compared with the values for Q0 as the culture period increased. The Q1, Q2, and Q3 composites had a significant inhibitory effect ($p < 0.01$). On day 7, Q3 inhibited tumor growth better than Q1 and Q2 ($p < 0.05$). The results showed that different NCTD levels affect cell viability differently. The higher the tumor cell inhibition, the better the viability of normal cells. Considering the effect of the composite extracts on the osteoblasts, the Q2 concentration of NCTD is best at promoting osteogenesis and inhibiting the proliferation of bone tumor cells.

To demonstrate our hypothesis, on day 2 of the culturing of OS cells with the different composite extracts, samples were collected by flow cytometry for apoptosis analysis using Annexin V-FITC and PI. Figure 7(a) shows that the Sr/CS/HAP material (Q0) induced about 6.3% apoptosis and 5% necrosis, whereas the apoptosis and necrosis rates of the Q1, Q2, and Q3 materials were 5% and 6.8%, 4.2% and 6.5%, and

3.7% and 9.7%, respectively. Figure 7(b) results display the apoptosis rate of Q2 and Q3 was significantly higher than that of Q0 ($p < 0.05$), Q2 was significantly higher than that of Q1 ($p < 0.05$), Q3 was significantly higher than that of Q1 ($p < 0.01$). The necrosis rate of Q1 was significantly higher than that of Q0 ($p < 0.05$), Q3 was significantly higher than that of Q0 ($p < 0.001$), and Q3 was significantly higher than that of Q1 and Q2 ($p < 0.01$), indicating that the addition of NCTD significantly induced apoptosis of the OS cells. Apoptosis increased with the increase in the concentration of NCTD, which is consistent with recent research [37].

In addition, osteolytic bone resorption is common in OS due to the osteolytic nature of OS cells. NCTD inhibits protein, DNA, and RNA syntheses, so we quantified the expression of OS, osteoblasts, and osteogenic-related genes in the different composites. Apoptosis regulation involves two major pathways: the mitochondria-mediated endogenous pathway and the caspase-dependent exogenous pathway [38]. In the caspase-dependent exogenous pathway,
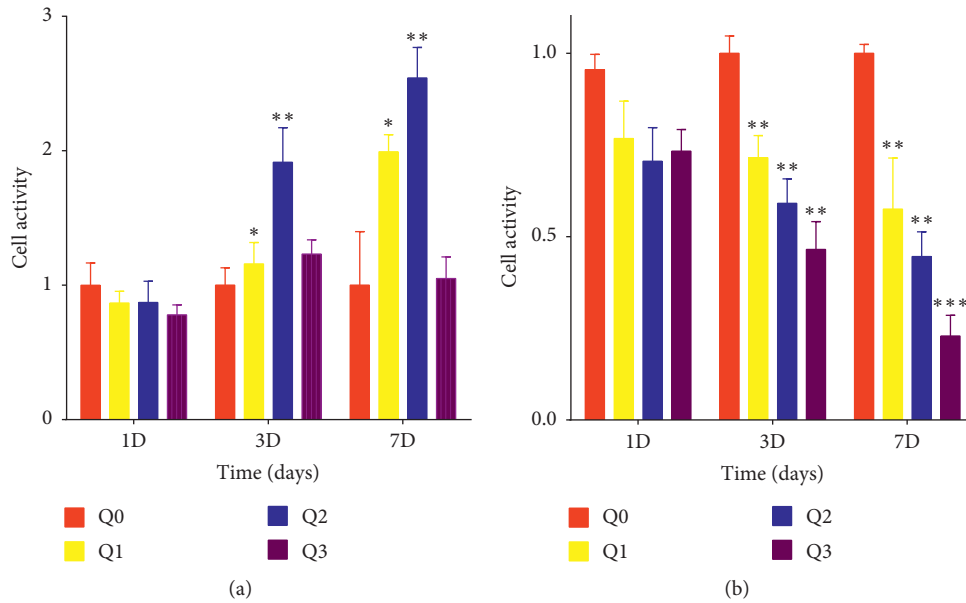
FIGURE 6: Effect of composites on the activity and cell viability of (a) murine osteoblast cell line MC3T3-E1 and (b) human osteosarcoma cell line MG-63 treated with the composite extracts for 1, 3, and 7 days. Cell viability was assayed using the CCK-8 method. Each experiment was repeated three times. $^*p < 0.05$ compared with Q0.
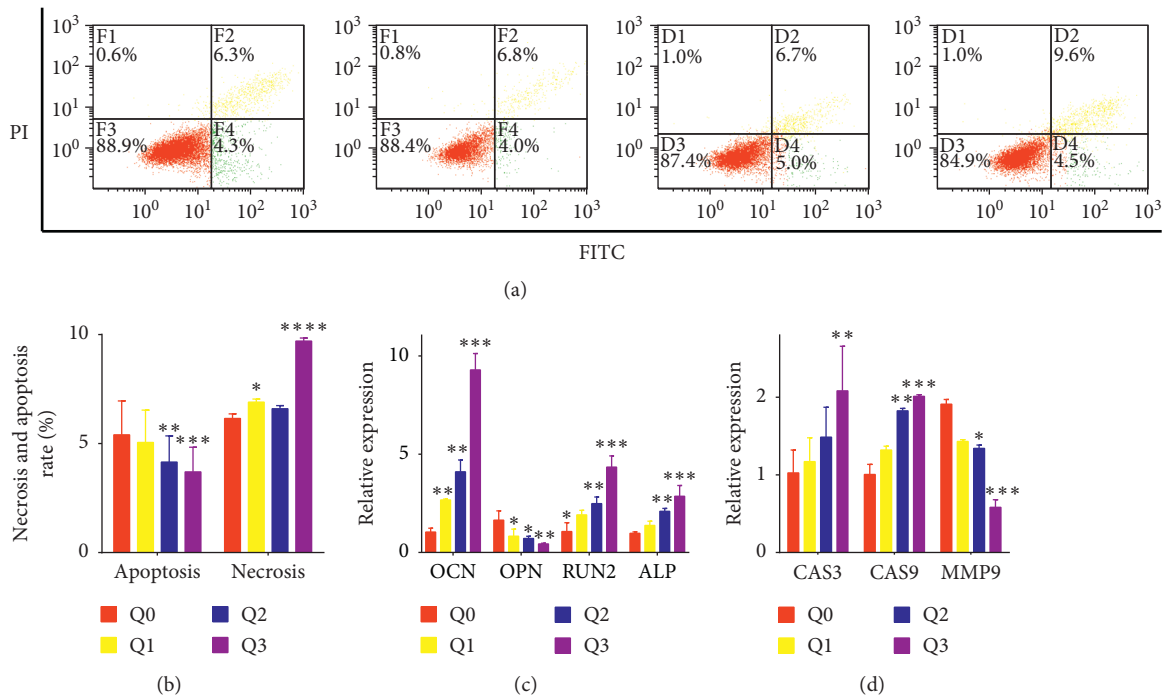
FIGURE 7: (a) Cells were treated with different material extracts for 72 h and then stained with annexin V-FITC and PI and analyzed by flow cytometry. (b) Necrosis and apoptosis rates of MG-63 cells in the material. Compared with Q0, the apoptosis rates of Q1, Q2, and Q3 were significantly higher. (c) Relative expression of osteogenic-related genes after 14 days of culture. All pro-osteogenic genes in Q3 were significantly higher. (d) Relative expression of apoptosis-related genes after 3 days of culture. All the genes were significantly in Q3 ($^*p < 0.05$; $^{**}p < 0.01$; $^{***}p < 0.001$) compared with the levels in Q0.

caspase-3 and caspase-9 are activated, which in turn leads to the cleavage of PARP [39]. Our study demonstrated that modification of the composite results in the upregulation of cleaved caspase-3, suggesting that the exogenous pathway

may be involved in inducing apoptosis. Studies have shown that NCTD induces cell shrinkage, nuclear fragmentation, and chromatin condensation in OS cells, which possibly induce apoptosis through exogenous pathways [36]. MMP-9

degrades gelatin and collagen and is closely related to the bone destruction caused by OS invasion. Figure 7(c) shows that the relative expression of CAS3 and CAS9 was higher in Q3 than in Q0 ($p < 0.05$) and that the expression of MMP9 in OS in the Q3 material was significantly lower than that in the Q0 composite ($p < 0.05$).

Figure 7(d) shows the mRNA expression levels of the osteogenic-related genes after osteoblasts were cultured in the composite extracts for 14 days. After 14 days of culture, the expression levels of Runx2, ALP, and OCN genes in the Q1, Q2, and Q3 composites were significantly higher than those in the control group, but the expression levels of the osteopontin (OPN) gene were significantly lower than that of the control group. In addition, Q3 had the greatest effect on the expression of the osteogenic-related genes Runx2, ALP, OCN, and OPN ($p < 0.01$). Bone formation consists of three main phases: proliferation, extracellular matrix maturation, and mineralization. Both ALP activity and collagen secretion increase with early osteogenic differentiation of osteoblasts [40], and Runx2 is the most important transcription factor for early osteoblast differentiation [41]. It has been reported that runx2 knockout mice have systemic osteogenic mineralization [42]. Runx2 also plays a role in the activation of genes involved in osteoblast differentiation, including ALP and OCN. OCN is a late marker of osteoblast differentiation, and its products indicate the onset of ECM deposition [43]. The relative expression levels of the above molecular indices were further confirmed by RT-PCR, confirming our understanding of the results in Figure 7(d). However, the expression of OPN was downregulated. Previous studies have demonstrated that OPN inhibits proliferation and differentiation of MC3T3-E1 cells [44]. Results of another study suggested that OPN has the ability to promote reuptake of osteoclasts as an effective stimulator of osteoclast absorption [45]. Our results appear to be consistent with those of these studies, suggesting that OPN, an inhibitor of osteoblast differentiation, is inhibited by Sr/CS/HAP. The difference in the results of the composites with respect to osteogenesis and osteogenesis-related gene expression may be due to the difference in the level of NCTD in the composites. However, potential mechanisms and signaling pathways require further research.

4. Conclusion

In the treatment of osteosarcoma, bone induction and inhibition of tumor cell growth are the key and difficult points. The results showed that the material of norcantharidin composite biomaterial had good biocompatibility, which do well in antitumor properties in vitro and promoted the mineralization of osteoblasts effectively. We believe that the strontium/chitosan/hydroxyapatite/norcantharidin composite biomaterials have a positive impact on the treatment of osteosarcoma. This study may provide information for the introduction of promising implants in surgical resection for OS hindlimb reconstruction.

Data Availability

The data used to support the findings of this study are available from the corresponding author upon request.

Conflicts of Interest

The authors declare no conflicts of interest.

References

[1] A. J. Saraf, J. M. Fenger, and R. D. Roberts, "Osteosarcoma: accelerating progress makes for a hopeful future," *Frontiers in Oncology*, vol. 8, p. 4, 2018.

[2] D. J. Harrison, D. S. Geller, J. D. Gill, V. O. Lewis, and R. Gorlick, "Current and future therapeutic approaches for osteosarcoma," *Expert Review of Anticancer Therapy*, vol. 18, no. 1, pp. 39–50, 2018.

[3] R. J. Grimer, "Surgical options for children with osteosarcoma," *The Lancet Oncology*, vol. 6, no. 2, pp. 85–92, 2005.

[4] M. Gharedaghi, M. T. Peivandi, M. Mazloomi et al., "Evaluation of clinical results and complications of structural allograft reconstruction after," *Archives of Bone and Joint Surgery*, vol. 4, no. 3, pp. 236–242, 2016.

[5] D. Zhi, Y. Bai, J. Yang et al., "A review on cationic lipids with different linkers for gene delivery," *Advances in Colloid and Interface Science*, vol. 253, pp. 117–140, 2018.

[6] F. J. Martínez-Vázquez, M. V. Cabañas, J. L. Paris, D. Lozano, and M. Vallet-Regí, "Fabrication of novel si-doped hydroxyapatite/gelatine scaffolds by rapid prototyping for drug delivery and bone regeneration," *Acta Biomaterialia*, vol. 15, pp. 200–209, 2015.

[7] M. Xuan, Z. Wu, J. Shao, L. Dai, T. Si, and Q. He, "Near infrared light-powered janus mesoporous silica," *Journal of the American Chemical Society*, vol. 138, no. 20, pp. 6492–6497, 2016.

[8] D. Mitra, M. Li, E.-T. Kang, and K. G. Neoh, "Transparent copper-loaded chitosan/silica antibacterial coatings with long-term efficacy," *ACS Applied Materials & Interfaces*, vol. 9, no. 35, pp. 29515–29525, 2017.

[9] Y. Lu, M. Li, L. Li et al., "High-activity chitosan/nano hydroxyapatite/zoledronic acid scaffolds for simultaneous tumor inhibition, bone repair and infection eradication," *Materials Science and Engineering: C*, vol. 82, pp. 225–233, 2018.

[10] U. Sylwia, S. Krzysztof, B. A. Ewa, and D.-W. Marta, "Biocompatible polymeric nanoparticles as promising candidates for drug delivery," *Langmuir*, vol. 31, no. 23, pp. 6415–6425, 2015.

[11] I.-Y. Kim, S.-J. Seo, H.-S. Moon et al., "Chitosan and its derivatives for tissue engineering applications," *Biotechnology Advances*, vol. 26, no. 1, pp. 1–21, 2008.

[12] J. Venkatesan and S.-K. Kim, "Nano-hydroxyapatite composite biomaterials for bone tissue engineering-a review," *Journal of Biomedical Nanotechnology*, vol. 10, no. 10, pp. 3124–3140, 2014.

[13] P. Hongju, Y. Zi, L. Huanhuan et al., "Electrospun biomimetic scaffold of hydroxyapatite/chitosan supports enhanced osteogenic differentiation of mMSCs," *Nanotechnology*, vol. 23, no. 48, Article ID 485102, 2012.

[14] X. Zhang, L. Zhu, H. Lv et al., "Repair of rabbit femoral condyle bone defects with injectable nanohydroxyapatite/chitosan composites," *Journal of Materials Science: Materials in Medicine*, vol. 23, no. 8, pp. 1941–1949, 2012.

[15] Y. Lei, Z. Xu, Q. Ke et al., "Strontium hydroxyapatite/chitosan nanohybrid scaffolds with enhanced osteoinductivity for bone tissue engineering," *Materials Science and Engineering: C*, vol. 72, pp. 134–142, 2017.

[16] P. J. Marie, D. Felsenberg, and M. L. Brandi, "How strontium ranelate, via opposite effects on bone resorption and formation, prevents osteoporosis," *Osteoporosis International*, vol. 22, no. 6, pp. 1659–1667, 2011.

[17] P. J. Marie, P. Ammann, G. Boivin, and C. Rey, "Mechanisms of action and therapeutic potential of strontium in bone," *Calcified Tissue International*, vol. 69, no. 3, pp. 121–129, 2001.

[18] S. H. Kok, C. Y. Hong, M. Y. P. Kuo et al., "Comparisons of norcantharidin cytotoxic effects on oral cancer cells and normal buccal keratinocytes," *Oral Oncology*, vol. 39, no. 1, pp. 19–26, 2003.

[19] Y.-N. Chen, J.-C. Chen, S.-C. Yin et al., "Effector mechanisms of norcantharidin-induced mitotic arrest and apoptosis in human hepatoma cells," *International Journal of Cancer*, vol. 100, no. 2, pp. 158–165, 2002.

[20] W. Xiao, B. Dai, Y. Zhu, and D. Ye, "Norcantharidin induces autophagy-related prostate cancer cell death through beclin-1 upregulation by miR-129-5p suppression," *Tumour Biology: The Journal of the International Society for Oncodevelopmental Biology and Medicine*, vol. 37, no. 12, pp. 15643–15648, 2016.

[21] L. P. Deng, J. Dong, H. Cai, and W. Wang, "Cantharidin as an antitumor agent: a retrospective review," *Current Medicinal Chemistry*, vol. 20, no. 2, pp. 159–166, 2013.

[22] Y. Zhu, Y. Mi, Z. Wang, X. Jia, and Z. Jin, "Norcantharidin inhibits viability and induces cell cycle arrest and apoptosis in osteosarcoma," *Oncology Letters*, vol. 17, no. 1, pp. 456–461, 2018.

[23] L. Mei, W. Sang, K. Cui, Y. Zhang, F. Chen, and X. Li, "Norcantharidin inhibits proliferation and promotes apoptosis via c-Met/Akt/mTOR pathway in human osteosarcoma cells," *Cancer Science*, vol. 110, no. 2, pp. 582–595, 2019.

[24] X.-q. Li, S.-h. Shao, G.-l. Fu, X.-h. Han, and H. Gao, "Study on norcantharidin-induced apoptosis in SMMC-7721 cells through mitochondrial pathways," *Chinese Journal of Integrative Medicine*, vol. 16, no. 5, pp. 448–452, 2010.

[25] K. Jehnhwa, Y. L. Chu, J. S. Yang et al., "Cantharidin induces apoptosis in human bladder cancer TSGH 8301 cells through mitochondria-dependent signal pathways," *International Journal of Oncology*, vol. 37, no. 5, pp. 1243–1250, 2010.

[26] D. Govindaraj, C. Govindasamy, and M. Rajan, "Binary functional porous multi mineral-substituted apatite nanoparticles for reducing osteosarcoma colonization and enhancing osteoblast cell proliferation," *Materials Science and Engineering: C*, vol. 79, pp. 875–885, 2017.

[27] Q. He, S. Xue, Y. Tan et al., "Dual inhibition of Akt and ERK signaling induces cell senescence in triple-negative breast cancer," *Cancer Letters*, vol. 448, pp. 94–104, 2019.

[28] A. Fonseca-García, J. D. Mota-Morales, Z. Y. García-Carvajal et al., "Effect of doping in carbon nanotubes on the viability of biomimetic chitosan-carbon nanotubes-hydroxyapatite scaffolds," *Journal of Biomedical Materials Research Part A*, vol. 102, no. 10, pp. 3341–3351, 2014.

[29] F. Wu, J. Li, K. Zhang et al., "Multifunctional coating based on hyaluronic acid and dopamine conjugate for potential application on surface modification of cardiovascular implanted devices," *ACS Applied Materials & Interfaces*, vol. 8, no. 1, pp. 109–121, 2016.

[30] K. Qiu, X. J. Zhao, C. X. Wan, C. S. Zhao, and Y. W. Chen, "Effect of strontium ions on the growth of ROS17/2.8 cells on porous calcium polyphosphate scaffolds," *Biomaterials*, vol. 27, no. 8, pp. 1277–1286, 2006.

[31] F. Yang, D. Yang, J. Tu, Q. Zheng, L. Cai, and L. Wang, "Strontium enhances osteogenic differentiation of mesenchymal stem cells and in vivo bone formation by activating Wnt/catenin signaling," *Stem Cells*, vol. 29, no. 6, pp. 981–991, 2011.

[32] S. J. Saint-Jean, C. L. Camiré, P. Nevsten, S. Hansen, and M. P. Ginebra, "Study of the reactivity and in vitro bioactivity of sr-substituted α-TCP cements," *Journal of Materials Science: Materials in Medicine*, vol. 16, no. 11, pp. 993–1001, 2005.

[33] H. Yuan, K. Kurashina, J. D. de Bruijn, Y. Li, K. de Groot, and X. Zhang, "A preliminary study on osteoinduction of two kinds of calcium phosphate ceramics," *Biomaterials*, vol. 20, no. 19, pp. 1799–1806, 1999.

[34] J. L. Simon, T. D. Roy, J. R. Parsons et al., "Engineered cellular response to scaffold architecture in a rabbit trephine defect," *Journal of Biomedical Materials Research*, vol. 66A, no. 2, pp. 275–282, 2003.

[35] S. Shanmugam and B. Gopal, "Antimicrobial and cytotoxicity evaluation of aliovalent substituted hydroxyapatite," *Applied Surface Science*, vol. 303, pp. 277–281, 2014.

[36] T. Zhou, J. Wu, J. Liu, Y. Luo, and Y. Wan, "Fabrication and characterization of layered chitosan/silk fibroin/nano-hydroxyapatite scaffolds with designed composition and mechanical properties," *Biomedical Materials*, vol. 10, no. 4, Article ID 045013, 2015.

[37] Y. Mi, Y. Zhu, Z. Wang, X. Jia, and Z. Jin, "Norcantharidin inhibits viability and induces cell cycle arrest and apoptosis in osteosarcoma," *Oncology Letters*, vol. 17, no. 1, 2019.

[38] E. Susan, "Apoptosis: a review of programmed cell death," *Toxicologic Pathology*, vol. 34, no. 4, pp. 495–516, 2007.

[39] A. Lopez-Beltran, G. T. Maclennan, L.H.-R. J. De, R. Montironi, and L. Cheng, "Research advances in apoptosis-mediated cancer therapy: a review," *Analytical and quantitative cytology and histology*, vol. 29, no. 2, pp. 71–78, 2007.

[40] M. Li, P. He, Y. Wu et al., "Stimulatory effects of the degradation products from Mg-Ca-Sr alloy on the osteogenesis through regulating ERK signaling pathway," *Scientific Reports*, vol. 6, no. 1, p. 32323, 2016.

[41] L. Shiting, K. Hui, Y. Naihui et al., "The role of runt-related transcription factor 2 (Runx2) in the late stage of odontoblast differentiation and dentin formation," *Biochemical & Biophysical Research Communications*, vol. 410, no. 3, pp. 698–704, 2011.

[42] T. Takeshi, H. Eiichi, N. Ryota et al., "An analysis of skeletal development in osteoblast-specific and chondrocyte-specific runt-related transcription factor-2 (Runx2) knockout mice," *Journal of Bone & Mineral Research*, vol. 28, no. 10, pp. 2064–2069, 2013.

[43] J. Zhou, B. Li, S. Lu, L. Zhang, and Y. Han, "Regulation of osteoblast proliferation and differentiation by interrod spacing of Sr-HA nanorods on microporous titania coatings," *ACS Applied Materials & Interfaces*, vol. 5, no. 11, pp. 5358–5365, 2013.

[44] H. Weibiao, C. Brian, R. George et al., "Osteopontin is a negative regulator of proliferation and differentiation in MC3T3-E1 pre-osteoblastic cells," *Bone*, vol. 34, no. 5, pp. 799–808, 2004.

[45] J. An, H. Yang, Q. Zhang et al., "Natural products for treatment of osteoporosis: the effects and mechanisms on promoting osteoblast-mediated bone formation," *Life Sciences*, vol. 147, pp. 46–58, 2016.

Research Article

Risedronate Effects on the In Vivo Bioactive Glass Behavior: Nuclear Magnetic Resonance and Histopathological Studies

Siwar Mosbahi,[1,2] Hassane Oudadesse ⬤,[1] Claire Roiland,[1] Bertrand Lefeuvre,[1] Lotfi Slimani,[3] and Hassib Keskes[2]

[1]*Univ Rennes, CNRS, ISCR-UMR 6226, F-3500Rennes, France*
[2]*Experimental Surgery of the Musculoskeletal System Laboratory, Sfax Faculty of Medicine, Sfax, Tunisia*
[3]*EA2496, Faculty of Dentistry, Paris Descartes University, Montrouge, France*

Correspondence should be addressed to Hassane Oudadesse; hassane.oudadesse@univ-rennes1.fr

The present study aimed to enhance the anti-osteoporotic performance of bioactive glass (46S6) through its association with bisphosphonate such as risedronate with amounts of 8, 12, and 20%. Obtained composites have been called 46S6-8RIS, 46S6-12RIS, and 46S6-20RIS, respectively. In vitro and in vivo explorations have been carried out. Bioactive glass and risedronate association has been performed by adsorption process. Structure analyses have been carried out to evaluate and to understand their chemical interactions. Solid Nuclear Magnetic Resonance (NMR) has been employed to study the structural properties of obtained biocomposite. The spectra deconvolution showed the appearance of a species (Q^4) in the biocomposites 46S6-8RIS, 46S6-12RIS, and 46S6-20RIS indicating their successful chemical association. In vitro experiments showed the enhancement of the chemical reactivity of the composites 46S6-xRIS compared to the pure bioactive glass. In fact, the silicon liberation after 30 days of immersion was 50 ppm for pure bioactive glass 46S6, and 41, 64, and 62 from 46S6-8RIS, 46S6-12RIS, and 46S6-20RIS, respectively. Based on the in vitro results, 46S6-8RIS was implanted in the femoral condyle of an ovariectomized rat and compared with implanted pure glass in the goal to highlight its anti-osteoporotic performance. After 60 days, implanted group with 46S6-8RIS showed the increase in bone mineral density (BMD with 10%) and bone volume fraction (BV/TV with 80%) and the decrease in trabecular separation (Tb/Sp with 74%) when compared to that of 46S6 group. These results are confirmed by the histopathological analyses, which showed the bone trabeculae reconnection after the 46S6-8RIS implantation. Chemical analyses showed the reduction in silicon (Si) and sodium (Na) ion concentrations, and the rise in calcium (Ca) and phosphorus (P) ion levels, which was explained by the dissolution of biocomposite matrix and the deposition of hydroxyapatite layer. Histomorphometric results highlighted the risedronate effect on the antiosteoporotic phenomenon. Obtained results showed good behavior with only 8% of introduced risedronate in the glass matrix.

1. Introduction

Osteoporosis is a skeletal disorder characterized by low bone density and an elevated risk of fracture. For its treatment, people resorted to enhance tissue engineering through the association and the grafting of some anti-osteoporotic drug with biomaterial. In our case the association has been established between a bisphosphonate, which has a good anti-osteoporotic effect in bone, such as the risedronate and bioactive glass having an active surface. Indeed, risedronate reduce the bone resorption directly and/or indirectly through the inhibition of osteoclast recruitments to bone surfaces, the inhibition of osteoclast activity on the surface and the shortening of the osteoclast life span. Bioactive glass has received special

attention due to its enhanced bone-bonding ability. One added advantage of silica based bioactive glass is its superior bone-bonding ability [1], due to the silicon presence, which play an integral role on in vivo bone formation [2].

The first of bioactive glass called 45S5 was discovered by Hench [3, 4]. It was completed by the 46S6 which presented the following chemical composition 46 wt% SiO_2, 24 wt% CaO, 24 wt% Na_2O and 6 wt% P_2O_5. Bioactive glass was used as bone graft or filler [5], dental [6], cranio maxillofacial applications [7] and implant coatings [8] due to their good bioactivity, osteoconductivity and osteostimulative properties.

The ability of biomaterial to bond to bone characterized its chemical reactivity and it is known by the formation of an apatite layer on its surface after its soaking in the simulated

body fluid (SBF) [9]. This apatite layer facilities the bonding interfaces between biomaterial and surround living bone after its implantation [10].

Bioactive glass offers a good clinical application. The kinetic of its chemical reactivity depends on its chemical composition. Consequently, its applications can be adapted for young or aged people. The surfaces of bioactive glass due to the presence of silicon facilities its bonding with the surrounding tissues and allow the enhancement of its biological and therapeutic properties. Its possible association with some chemical elements such as Zn, Mg, Sr,...) or organic molecules present interesting physicochemical and physiological advantages. It can be also associated with medical drug such as risedronate presented in this work.

The grafting of bioactive glass and risedronate has been carried out by adsorption process. Molecular adsorption is an initial and important event of biological responses which progress hierarchically at interfaces between materials surface and bimolecular. Therefore, it should be regulated completely for progress of safer regenerative medicine and advanced biomedical engineering.

The association and the coating of implanted materials and the enhancement of physiological properties were well developed recently in several fields such as orthopedic and cardiology. The first study revealed the enhancement of implanted material surface by its coating based on hyaluronic acid and dopamine conjugate [11]. The second study underlined the improvement of cardiovascular implants surface by the control of the molecular weight of the hyaluronic Acid Conjugated of the amine grafted on the material surface [12].

In fact, this study aimed to understand the biological effect of the grafting risedronate in bioactive glass surface after its implantation at an osteoporotic model and to compare the obtained results with these which were implanted with pure bioactive glass. For that, physicochemical analyses, histological and histomorphometric explorations have been performed.

2. Material and Methods

2.1. Bioactive Glass Synthesis. Bioactive glass with the chemical composition of 46 wt% SiO_2, 24 wt% CaO, 24 wt% Na_2O and 6 wt% P_2O_5 was synthesized by the melting process. The starting materials, calcium silicate ($CaSiO_3$), sodium metasilicate (Na_2SiO_3) and sodium phosphate ($NaPO_3$) were weighed and mixed by mechanical mixer for 2 hours. The mixture was then heated in a platinum crucible according to the following steps. First, the temperature was ramped to 900°C and then kept at 900°C for 1 hour to decompose the chemical constituents. Afterwards, the temperature was raised and kept at 1300°C for 3 hours to melt the reactive mixture. The melted bioactive glass was then poured into preheated brass moulds and annealed for 4 hours at the glass transition temperature (T_g = 536°C) to remove the residual mechanical stress. After cooling to room temperature, the bulk glasses were ground into powder and sieved to obtain bioactive glass particles with size less than 40 μm.

2.2. Loading of Risedronate on the Bioactive Glass Surface by the Adsorption Process. Adsorption experiments were performed under physiological temperature (37 ± 1°C), by dissolving of 50 mg of bioactive glass sample in 5 ml of risedronate solutions (concentration ranging from 0.8 to 2 mM) in a polyethylene tube. The latter were processed through the dispersing of the appropriate quantity of risedronate in a standard solution (1 mM of KCl solution); the pH of the obtained solutions was stabilized at 7.4 employing hydrochloric acid and potassium hydroxide solutions. After ultrasound for 1–3 min, the suspensions were incubated for 20, 40, 60 and 80 min without stirring and centrifuged for 20 min at 15000 rpm. For comparison, two references have been prepared and incubated in the same solution: the first contained only the risedronate while the second contained the bioactive glass. After centrifugation, the obtained composites were washed with deionized water, lyophilized, filtrated on Millipore filters (0.2 μm) and led to obtain our composites (46S6-8RIS, 46S6-12RIS and 46S6-20RIS).

2.3. In Vitro Assays of 46S6 and 46S6-xRIS (x = 8, 12 and 20%) in the Simulated Body Fluid (SBF). Chemical reactivity of 46S6 and 46S6-xRIS were evaluated trough the soaking of 30 mg of powder in 60 ml of the SBF solution during 1, 15 and 30 days at 37.0 ± 0.2°C with shake at 50 rpm. The SBF solution composition was similar to the blood plasma. Its preparation was described in our previous work [13]. After each soaking period, the 46S6 and the 46S6-xRIS powders were removed and succeed by rinsing with the deionized water to stop the chemical exchanges and then followed by absolute alcohol. Powders were investigated by using several physicochemical characterizations in the goal to understand the mechanism of the hydroxyapatite (HA) layer formation. The SBF solutions were kept in fridge to study the ionic exchanges between biomaterial and SBF using the Inductively Coupled Plasma-Optical Emission Spectrometry (ICP-OES).

2.4. Animal's Model and Experimental Design. Thirty-two Female Wistar rats aged between 16 and 19 weeks and weighed between 250 and 300 g were used in this study. They were obtained from the central pharmacy of Tunisia. They were housed in a specially equipped pet shop. Several parameters were taken into consideration: the ambient temperature between 23°C and 30°C and adequate ventilation have been tried; they allow regulating the temperature and the humidity, to ensure a good supply of oxygen and to eliminate the dust and the bad odors. The required light intensity cycle for our laboratory animals was 12 hours of light alternating with 12 hours of darkness. The rats were adapted to their new condition during 10 days before the starting of the study and were fed on a pellet diet (Sicco, Sfax, Tunisia) and tap water ad libitum. The Tunisian ethical committee authorized the experimental using of the animals. Sixty days after bilateral ovariectomy for the creation of osteoporosis phenomenon, rats were divided into four groups:

- (i) T: Used as negative control: (none ovariectomized and none implanted).
- (ii) T+: Used as positive control (ovariectomized and none implanted).
- (iii) 46S6: Implanted with pure bioactive glass (ovariectomized and implanted with 46S6).
- (iv) 46S6-8RIS: Implanted with biocomposite (ovariectomized and implanted with 46S6-8RIS).

2.5. Surgical Operation. Surgical operations were realized under general anesthesia in aseptic conditions. Indeed, for the anesthesia inductions, we used the chloral hydrate depending on the body weight. The sites of surgical operation were cleaned with 96% alcohol and antiseptic solutions. The obtained empty defects were irrigated profusely with physiological saline solution to eliminate bone debris. Bone defects of 3 mm diameter and 4 mm deep have been created in the lateral aspect of the femoral condyle using a refrigerated drill to avoid necrosis. It was filled with 10 mg of 46S6 and 46S6-8RIS in the cylindrical forms. The closure of the wounds was performed in layers (that is, fascias and the subcutaneous tissue) using a resorbable suture lines in a continuous fashion. All operated rats received subcutaneous analgesia during three days after the surgical operation and they were allowed unrestricted mobility during this period. Each rat receives a clinical examination every day. After 2 months of implantation, animals were sacrificed and samples (bone-biomaterials) were collected and were used for biological and physicochemical studies.

2.6. Physicochemical Characterization. The 46S6 and 46S6-xRIS powders before and after soaking in SBF solution were analyzed by several physicochemical techniques in the goal to choose the best composite 46S6-xRIS for the in vivo assays. Functional groups' structure evaluation and chemical analysis have been carried out.

2.6.1. Infrared Analysis. The Fourier Transformed Infrared Spectroscopy (FT-IR) (Bruker Equinox 55) was used to determine the functional groups of the prepared 46S6 and 46S6-xRIS composites. In fact, fine powders were mixed with KBr powder and the mixture subjected to a load of 10 tons/cm^2 in order to produce discs. FTIR collected spectra were taken in the range 400 and 4000 cm^{-1} with resolution of 2 cm^{-1}.

2.6.2. Structure Analysis by Nuclear Magnetic Resonance. 46S6, 46S6-8RIS, 46S6-12RIS and 46S6-20RIS were ground and disposed into zirconium Brokers rotors (4 mm diameter). High-resolution solid-state NMR experiments were acquired at room temperature and pressure using a Bruker MAS spectrometer ASX300 (7T). The shift (ppm) has been calculated from the reference: tetramethylsilane $(CH_3)_4Si$ (TMS). ^{29}Si MAS-NMR spectra have been fitted with Dmfit software.

2.6.3. Inductively Coupled Plasma-Optical Emission Spectrometry (ICP-OES). We used Inductively Coupled Plasma-Optical Emission Spectroscopy (ICP-OES) using an iCAP 7000 series (ThermoFisher Scientific). It can provide low cost multielement analysis for measuring trace elements in a diverse liquid sample range. In function of the element or the quantity analyses can be made using various wavelength or axial/radial measurement.

This method is based on the atom's ionization. It possessed a high sensitivity less than 1 μm/g. It permits to determine the amounts of all elements present in the studied matrix. ICP-OES was used in this study to evaluate the ionic exchanges firstly between biomaterials and SBF solution and

secondly between biomaterials and bone (interface bone-biomaterial).

2.6.4. Ultraviolet–Visible Spectroscopy. We used Ultraviolet-visible (UV–Visible) spectrophotometry using a 7315 Spectrophotometer (Jenway) with the integrated capacity to realise various measurement modes: for absorbance, % transmittance, concentration, spectrum scanning, kinetics and quantitation. Its wavelength is on a range from 198 nm to 1000 nm using a xenon lamp with a resolution of 1 nm and accuracy of ±2 nm.

Risedronate content in the SBF solution was quantified using UV spectroscopy absorption at 262 nm as reported in our previous work [14] in order to evaluate the kinetic of drug release in the SBF solution during 1, 15 and 30 days of immersion [14].

2.7. Biological Effect of Risedronate on the Osteoporosis Phenomenon

2.7.1. Histological Analysis. Harvested implanted femoral condyles have been fixed in Burdack (formalin) and included in a mixture of poly-methylmethacrylate (PMMA) and glycolmethacrylate (GMA) without prior decalcification. Sections of 6-7 mm thick were debited along a transverse plane using a sliding microtome (Reichert-Jung). Obtained sections were stained by modified goldner trichrome.

2.7.2. Micro-Computed Tomography. Micro-computed tomography represents a precise and effective technique to visualize, assess and quantify bone healing, formation and mineralization in a three dimensional volume of interest. The scanning of femoral condyles was performed using a micro-computed tomographic (μCT) imaging system (Quantum FX Caliper Life Sciences, PerkinElmer, and Waltham, MA, USA). The voltage and the intensity of the X-ray source were fixed, respectively, at 90 V and 160 μA. Samples scanning were realized with a resolution of 40 μm. After the correction of the rotation and calibration center, the region of interest reconstruction (ROI) was fixed. The same calibration system and threshold was adopted for each scan. For the evaluation of healing process, we used the Microview software for three-dimensional μCT images reconstruction. The bone volume fraction (BV/TV), trabecular thickness (Tb/Th), trabecular separation (Tb/Sp), trabecular number (Tb/N), bone mineral density (BMD) and bone mineral content (BMC) have been calculated using a specific software ABA analysis (Version 2.2; GE Healthcare, London, Ontario, Canada).

Where: BV: bone volume in mm^3, Tb: Total bone in mm^3, Trabecular Thickness (Tb/Th): It is the average thickness of the trabeculae. The measurement unit is mm, Trabecular Number (Tb/N): is the number of trabeculae per unit of length. The unit of measurement is mm^{-1}, Trabecular Separation (Tb.Sp): is the main diameter of the cavities containing the bone marrow. The measurement unit is mm.

2.8. Statistical Analysis. The statistical analysis of the data was studied using the Student's *t*-test. All values are expressed as means ± standard error. Differences are considered significant at the 95% confidence level ($p < 0.05$).
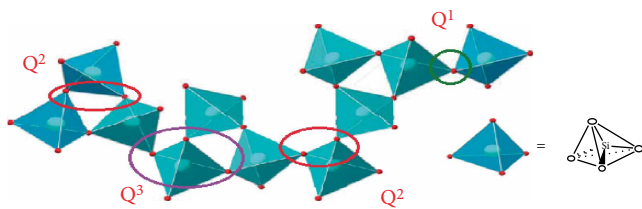
Figure 1: Structural model of silicate bioactive glass [15].

3. Results and Discussion

3.1. Assessment of 46S6 and 46S6-xRIS Association Using NMR Analyses. NMR technique is a power method to describe the structure of materials. Identified species Q^n characterize structural units as shown in Figure 1. Figure 2 shows the ^{29}Si MAS–NMR spectrum of 46S6, which was decomposed into two separate species. These species are centered at $\delta = -80$ and -86 ppm. They assigned to Q^2 and Q^3 structural units, respectively. Q^2 and Q^3 correspond, respectively, to a tetrahedron linked into the network through two or three bridging oxygen of SiO_4 [15] as shown in Figure 1.

Thanks to NMR software, the percentages of different species have been evaluated. Q^2 represents 84% while Q^3 shows 16% of the population of SiO_4 tetrahedrons [16]. The chemical neutrality around the non-bridging oxygen of Q^3 tetrahedral is respected by the preferential presence of Na^+ cations and is shown as Si $(OSi)_3(O...Na)$. The nonbridging oxygens of Q^2 species are rather combined with Ca^{2+} cations and Na^+ remaining cations as presented in Table 1. These two combinations could be expressed as Si $(OSi)_2(O_2...Ca)$ and $Si(OSi)_2(O...Na)_2$ [17].

^{29}Si MAS–NMR spectrum of 46S6-8RIS underlined the presence of these species with a slight displacement. We revealed also the decline of Q^2 to 56% and the intensification of Q^3 to 44%. This is explained by the transfer presence from Q^2 to Q^3 species in the composition of 46S6-8RIS composite. This data emphasize the risedronate effect on the pure glass structural model. This result could be explained by the risedronate effect in the cleaving of Si–O–Si link in the Q^2 tetrahedral to form Q^3 tetrahedral. Its association with the vitreous pure glass matrix explains the risedronate effect in the breaking of Si–O–Si links. This result is in good agreement with previous study during the association of pure glass with chitosan. Thus, the deconvolution of the initial 46S6-Chitosan composite shows two respectively attributed resonances to Q^2 and Q^3 units as observed in the initial pure glass. However, the quantity of Q^2 is more than the one in the initial pure glass. Accordingly, Oudadesse et al. demonstrate the transfer from Q^3 species to Q^2 species in the composition of 46S6-Citosan composite [18].

The ^{29}Si MAS–NMR spectrum of 46S6-12RIS showed the presence of Q^2 and Q^3, respectively, with 55% and 44%. In addition, we observed the emergence and development of a new species Q^4 with a chemical shift centered at 109 ppm (1%). The Q^4 characterizes the silicon in tetrahedral environment with four bridging oxygen. This silicon environment corresponds to pure silica (SiO_2) [10]. However, the association
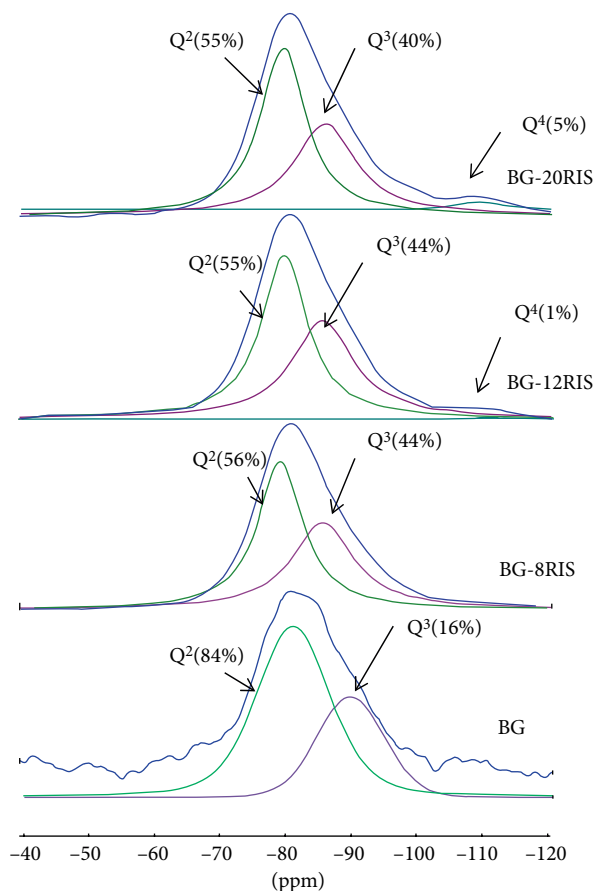
Figure 2: 29Si NMR spectra of 46S6, 46S6-8RIS, 46S6-12RIS and 46S6-20RIS after 40 min of their association by using adsorption process.

Table 1: Contribution and chemical shifts of different species in ^{29}Si spectra of 46S6, 46S6-8RIS, 46S6-12RIS and 46S6-20RIS.

Composites	Species					
	Q^2		Q^3		Q^4	
	ppm	%	ppm	%	ppm	%
46S6	−80	84	−86	16	0	0
46S6-8RIS	−79	56	−85	44	0	0
6S6-12RIS	−79	55	−85	44	−109	1
46S6-20RIS	−79	55	−85	40	−109	5

between 20% RIS and pure bioactive glass, showed the attenuation of Q^3 (40%) and the rising of Q^4 (5%). Subsequently, in the 46S6-20RIS composition we revealed a transfer from Q^3 to Q^4 species. The Q^4 emergence and development highlight the perturbation of pure glass vitreous matrix. Consequently, these findings emphasize the chemical link between bioactive glass and risedronate, as shown in Figure 1.

3.2. Pure Bioactive Glass 46S6 and 46S6-xRIS Characterizations before and after Immersion in SBF Solution

3.2.1. Investigation of 46S6 and 46S6-xRIS Behaviors before and after the Immersion in the SBF Solution Employing Infrared

(a)

(b)
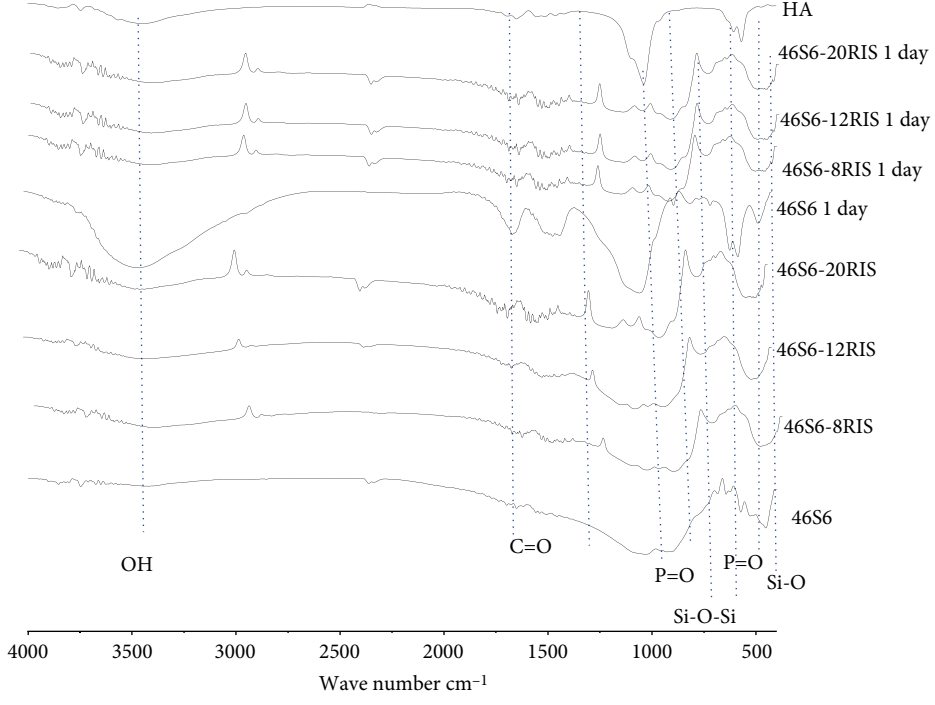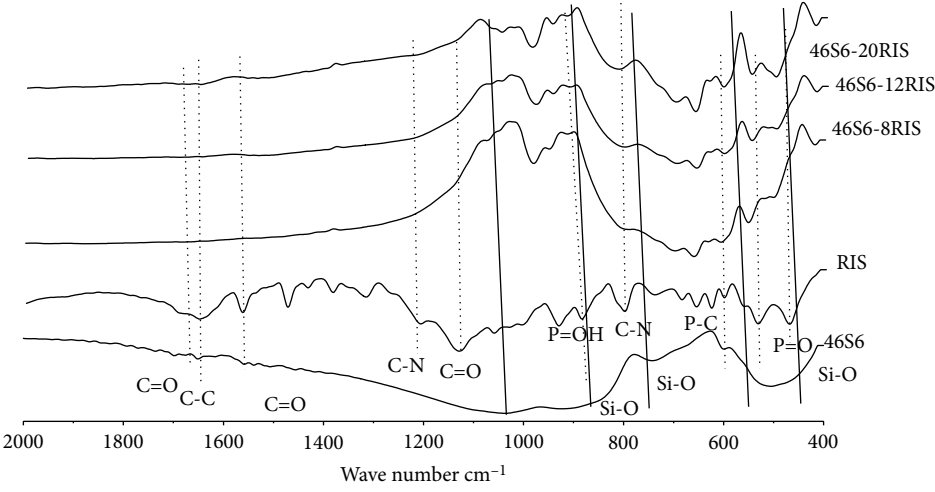
FIGURE 3: Continued.

(c)

(d)
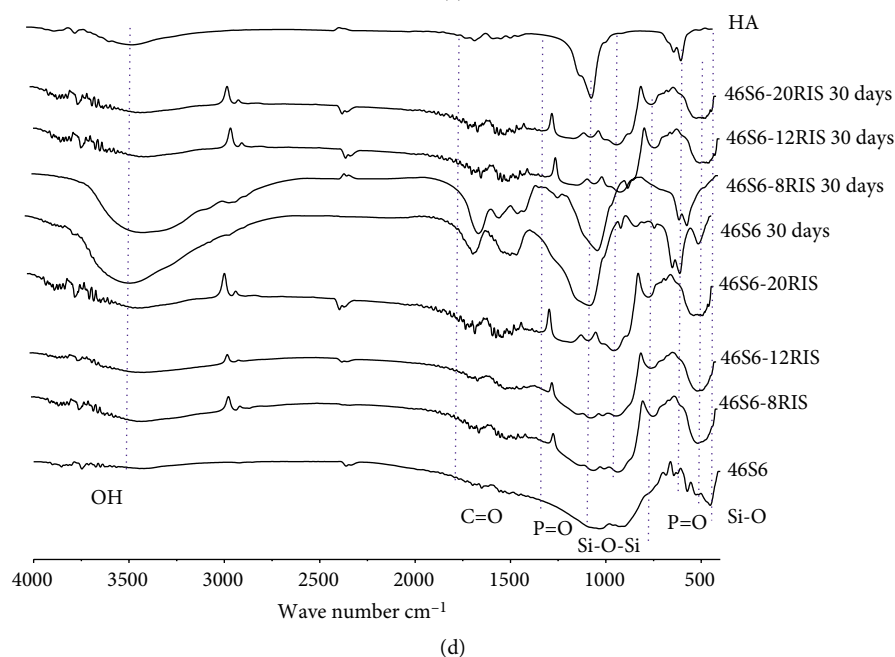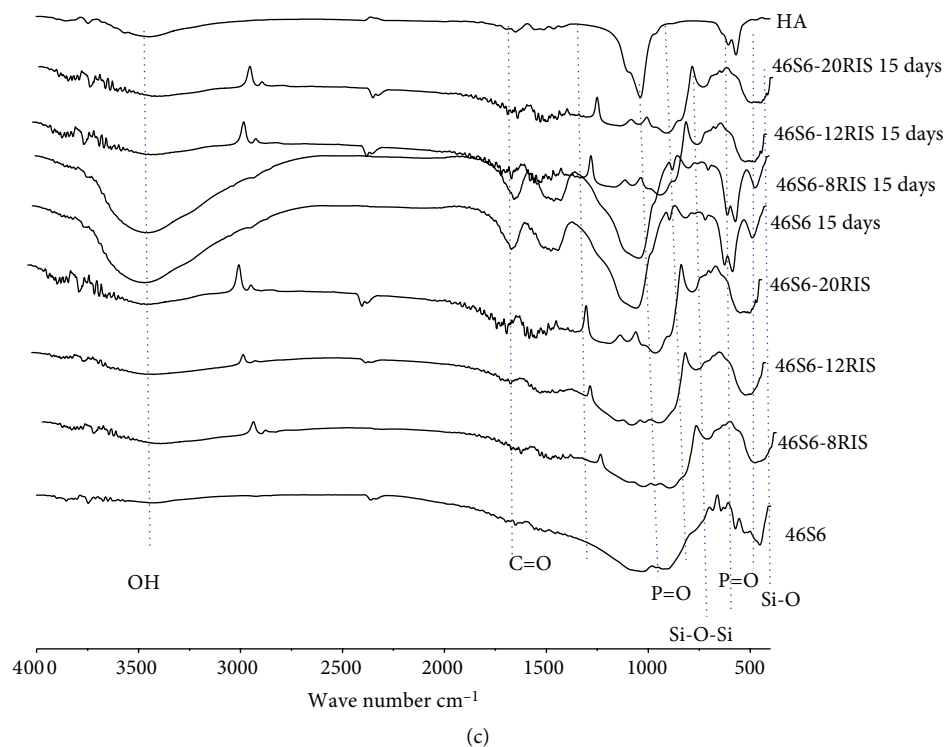
FIGURE 3: (a) FTIR spectra of 46S6, risedronate, 46S6-8RIS, 46S6-12RIS and 46S6-20RIS composites before soaking in the SBF solution [14]. (b) Infrared spectra of 46S6, 46S6-8RIS, 46S6-12RIS, 46S6-20RIS and HA before after 1 day of immersion in the SBF solution. (c) Infrared spectra of 46S6, 46S6-8RIS, 46S6-12RIS, 46S6-20RIS and HA before after 15 days of immersion in the SBF solution. (d) Infrared spectra of 46S6, 46S6-8RIS, 46S6-12RIS, 46S6-20RIS and HA before after 30 days of immersion in the SBF solution.

Analysis (FTIR). As shown in Figure 3(a), FTIR spectra of 46S6-8RIS, 46S6-12RIS and 46S6-20RIS before immersion, revealed bands characterizing 46S6 and risedronate. Thus, these composites reveal the presence of Si–O band at the wavelengths of $911 \, cm^{-1}$ and $1027 \, cm^{-1}$ which were slightly shifted and attenuated intensity. Also, we note the existence of two bands characteristics of C=O, the first at the wavelength of $1700 \, cm^{-1}$, which was slightly shifted to the right, and the second at the wavelength $1130 \, cm^{-1}$ which intensified slightly. We remark likewise the presence of C=N, C=C and of C–N=O bands, respectively, at wavelengths $1200 \, cm^{-1}$, $1666 \, cm^{-1}$ and $1570 \, cm^{-1}$ and which were slightly shifted to the right. In the end, we notice the presence of P–O bands at wavelengths 468 and $537 \, cm^{-1}$. These chemical interactions between RIS and
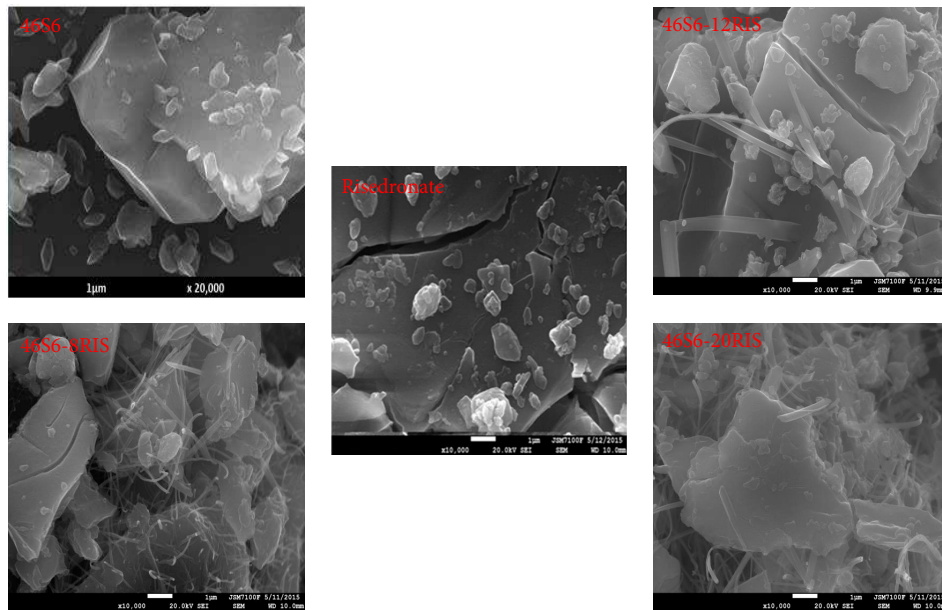
Figure 4: Morphologies of 46S6 [25], risedronate, 46S6-8RIS, 46S6-12RIS and 46S6-20RIS before immersion in the SBF solution [14].

46S6 highlights firstly the reactivity of our bioactive glass and secondly the strong ability of risedronate to bind to bioactive glass. Therefore, it was reported by previous studies [20] that RIS has a potential to bind strongly to HA, this can be explained by its affinity to bind to other molecules [21] and as a result to bone tissue [22].

Pure hydroxyapatite spectrum has been used as reference in this study and consists to emphasize these materials chemical reactivity [23]. After one day, the interfacial reaction of these biomaterials (46S6 and 46S6-xRIS) with the SBF physiological solution leads to the modification of their initial bands as shown in Figure 3(b). Therefore, bands at 932 cm^{-1}, 799 cm^{-1} and 470 cm^{-1} still remain; these bands are characteristic of bending and stretching vibration of the Si–O band in the pure silica tetrahedrons SiO_4. These results confirm the formation of the silica-rich layer at the surface of these materials. In addition, we showed the appearance of new bands in the 46S6 and 46S6-xRIS spectra such as three phosphate bands at 565, 603 and 1039 cm^{-1} assigned to stretching vibrations of PO_4^{3-} group in phosphate crystalline phases. This data displays the calcium phosphate layer formation. Also two carbonate bands at 874 and 1420 cm^{-1} are shown. The first band is characteristic of a bending vibration whereas the second band attributes to a stretching vibration of the C–O liaisons in carbonate groups. These findings emphasize the carbonated hydroxyapatite layer formation on 46S6-RIS surface (Figure 3(b)).

Fifteen days after the soaking in SBF solution, the characteristic bands of hydroxyl carbonated apatite: PO_4^{3-}, respectively, at wave numbers 565, 603, 1039 cm^{-1} and CO_3^{2-} at 874, 1420 cm^{-1} are well observed in the spectrum of 46S6 and also in the spectrum of 46S6-xRIS biocomposite. These characteristic bands are being noticed well in the spectrum of 46S6-8RIS biocomposite. This confirms the good crystallization of the apatite layer on the surface of 46S6-8RIS biocomposite as shown in Figure 3(c).

FTIR spectra of 46S6, 46S6-8RIS, 46S6-12RIS and 46S6-20RIS after 30 days of immersion in SBF are illustrated in Figure 3(d). They showed the appearance of several bands such as:

(i) The characteristic bands of hydroxyl carbonated apatite (PO_4^{3-}) are observed at 565, 603 and 1039 cm^{-1} and CO_3^{2-} at 874 and 1420 cm^{-1}. These bands are more intensified in the 46S6-8RIS spectrum which can contribute to the good crystallization of the formation of an apatite layer on its surface.

(ii) Three Si–O–Si bands observed at 470 cm^{-1} (bending vibration), 799 cm^{-1} (bending vibration) and 1075 cm^{-1} (stretch vibration) indicating the silica gel presence. It is due to the polymerization process at the glass surface. Subsequently, the appearance of both mineral apatite and silica gel highlights the chemical interactions between the biomaterial and the physiological solution as described by Hench et al. [23, 24]. Consequently, these data exhibit the bioactivity of both 46S6 and 46S6-xRIS biocomposite. Therefore, they illustrate the good effect of risedronate on the pure glass bioactivity. In fact, the 46S6-8RIS composite shows the speedy formation of well-crystallized apatite layer on its surface and in a quickest moment as compared to the 46S6.

3.2.2. Investigation of 46S6 and 46S6-xRIS Behaviors before and after the Immersion in the SBF Solution Using the Scanning Electron Microscopy (SEM). The SEM photographs of risedronate presented in Figure 4 manifest the presence of blocks formed of contiguous lamellas, while the surface of 46S6 bioactive glass was smooth fragments [25]. Moreover, in the 46S6-8RIS and 46S6-12RIS surface, risedronate adhered to the bioactive glass particles and created some interstices on the surface of the 46S6-xRIS composite. The risedronate
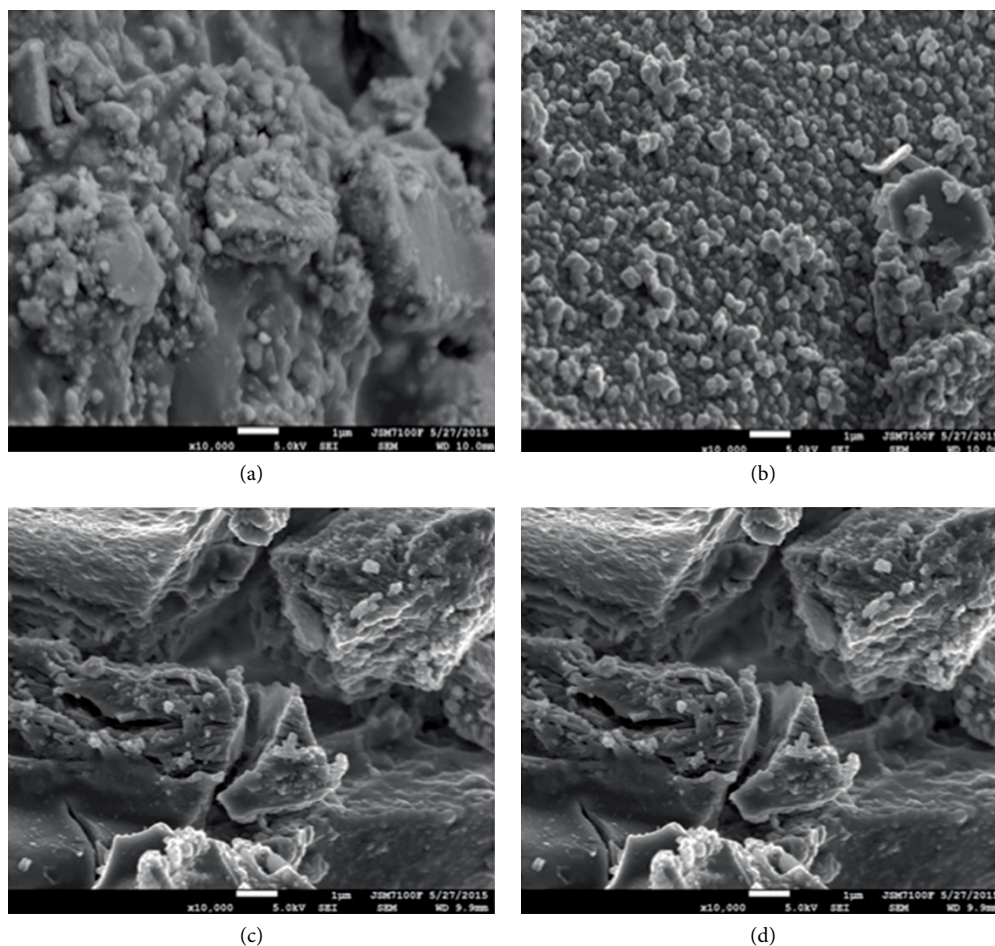
(a)

(b)

(c)

(d)

Figure 5: Morphologie of 46S6 (a), 46S6-8RIS (b), 46S6-12RIS (c) and 46S6-20RIS (d) after 1 day of immersion in the SBF solution.

molecules modify strongly the surface morphology of pure bioactive glass. However, after the incorporation of 20% of RIS to 46S6, the 46S6-20RIS surface was completely surrounded by risedronate filaments. These results are in good agreement with others reported works after the association of 46S6 with chitosan [18] and zoledoronate [21] and underlining the chemical reactivity of 46S6 surface.

After 1 day of soaking, the morphology of the 46S6 and 46S6-8RIS surface is quite similar for both compositions, presenting particles packed in spherical aggregates (Figures 5(a) and 5(b)). This result is in coincidence with result reported for the composite of 46S6 with magnesium [24] at same condition.

The microstructures of the 46S6 bioactive glass and of the 46S6-xRIS composite after 30 days of soaking in SBF solution are shown in Figure 6. The surface of bioactive glass is covered by fairly homogeneous particles. In the composite 46S6-8RIS (Figure 6(b)), the risedronate molecules do not appear. This indicates that the risedronate molecules are released from the surface of the 46S6-8RIS composite into the SBF solution. This result underlines the therapeutical effect of this composite. In fact, risedronate can be released from the composite 46S6-8RIS to the surrounding environment and heal bone pathologies after its implantation. As a consequence, this result is very interesting for biomedical applications. In addition, we noticed

a hydroxyapatite layer formed on the surface of the 46S6-8RIS composite. The surface of the bioactive glass-8RIS composite is covered by a dense apatite layer which is composed of small hydroxyapatite crystals of identical shape. It was appeared that the hydroxyapatite layer formed on the surface of 46S6-8RIS composite is denser and more visible than that of pure glass 46S6. This result is in agreement with those reported for the composite of 46S6 associated with chitosan [18] and zoledronate [21]. However, after 30 days soaking of 46S6-12RIS and 46S6-20RIS (Figures 6(c) and 6(d)), SEM micrographs did not reveal the layer of hydroxyapatite but changing of surfaces with a creamy aspect were observed. These results exhibit that the use of risedronate with a large quantity has mitigated the bioactivity and the chemical reactivity of 46S6. This result coincides with others which underline the decrease in the 46S6-xMg reactivity with the increase in magnesium quantities after 30 days [24]. This could be due to the fact that the high quantities of risedronate encased bioactive glass blocks and inhibits the ionic exchange between bioactive glass and SBF solution and as a consequent it retards the apatite formation.

3.2.3. Study of Silicon, Calcium and Phosphorus Releases in the SBF Solution through the ICP-OES Analysis. Results reported after the powder characterizations were completed by the
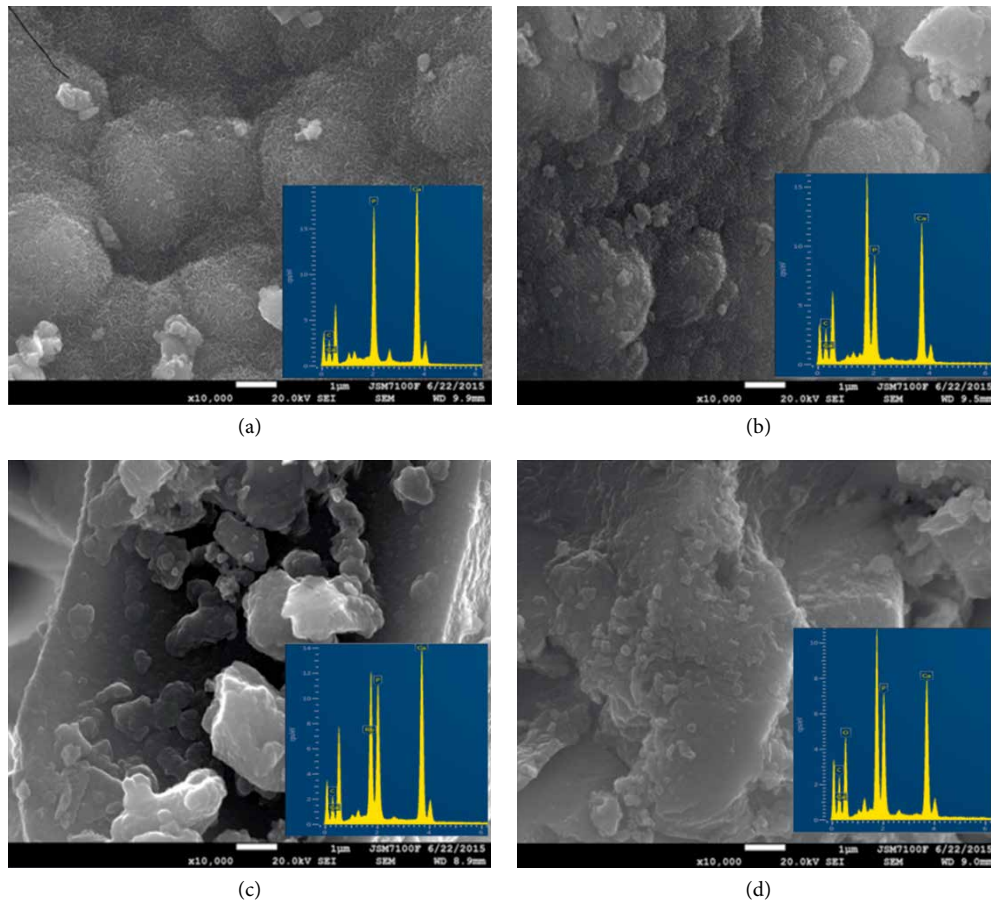
(a)

(b)

(c)

(d)

FIGURE 6: 46S6 (a), 46S6-8RIS (b), 46S6-12RIS (c) and 46S6-20RIS (d) morphologies after 30 days of immersion in the SBF solution.

chemical analysis evaluated on the SBF solution obtained after each immersion periods. Regarding silicon amount, it represents an indicator of bioactive glass dissolution when calcium and phosphorus amounts serve to comprehend the calcium phosphate formation [26]. Therefore, these results are very essential to understand the ionic exchanges between biomaterial surface and SBF solution.

As shown in Figure 7(a), silicon released in speedy manner during the first day from 0 to 50 ppm for the 46S6 and from 0 to 41 ppm for the 46S6-8RIS on average. The quickest release of silicon ions is an indicator of the first stage of dissolution by breaking up of the outer silica layers of the network highlighted by nuclear magnetic resonance (NMR). The solid silica dissolves in the form of monosilicic acid $Si (OH)_4$ to the solution resulting from breakage of Si–O–Si bonds and formation of Si–OH (silanols) at the glass solution interface. However, the risedronate presence diminishes this phenomenon and consequently the glass matrix dissolution. Therefore, it was released up to 30 days. The 46S6 and 46S6-8RIS, containing less risedronate, release much silicon in the SBF. In fact, 46S6-12RIS and 46S6-20RIS released, respectively, 64 and 62 ppm of silicon after 30 days of immersion. Thus, the bioactive glass grains are locked in the risedronate matrix, which explains the lower release. These results improved the progressive degradation of the 46S6 silica network in the SBF solution.

As illustrated in Figures 7(b) and 7(c), calcium and phosphorus releases are shown, they revealed the same looks. Indeed, calcium and phosphorus concentrations decrease continually from 1 day up to 30 days. It explains the calcium and phosphorus consumption by bioactive glass. However, calcium and phosphorus consumption increased with the decrease in risedronate quantity in the composite 46S6-xRIS. This low kinetic of calcium and phosphorus absorption leads for better crystallization of hydroxyapatite. However, the integration of bioactive glass with its high bioactivity stimulates the consumption of calcium and phosphorus and induces the hydroxyapatite formation.

3.2.4. Evaluation of Risedronate Kinetic Release in the SBF Solution Using Ultraviolet-Visible Spectroscopy. The risedronate kinetic release from the 46S6-xRIS composites to the SBF solution after 1, 15 and 30 days of soaking are presented in Figure 8. Therefore, after 1 day it was quickly released from all composites but more pronounced in the composite 46S6-12RIS and 46S6-20RIS. Moreover, after 30 days its liberation was stabilized in the composite 46S6-8RIS and still persists for the other. This clarify that all risedronate present in the composite 46S6-8RIS are released in the SBF and consequently permit the ionic exchange between biomaterial and SBF solution. This data underlined also that the 46S6-8RIS glass matrix degradation is more obvious than of 46S6-12RIS and 46S6-20RIS. Therefore, for the 46S6-12RIS and 46S6-20RIS,

(a)

(b)

(c)
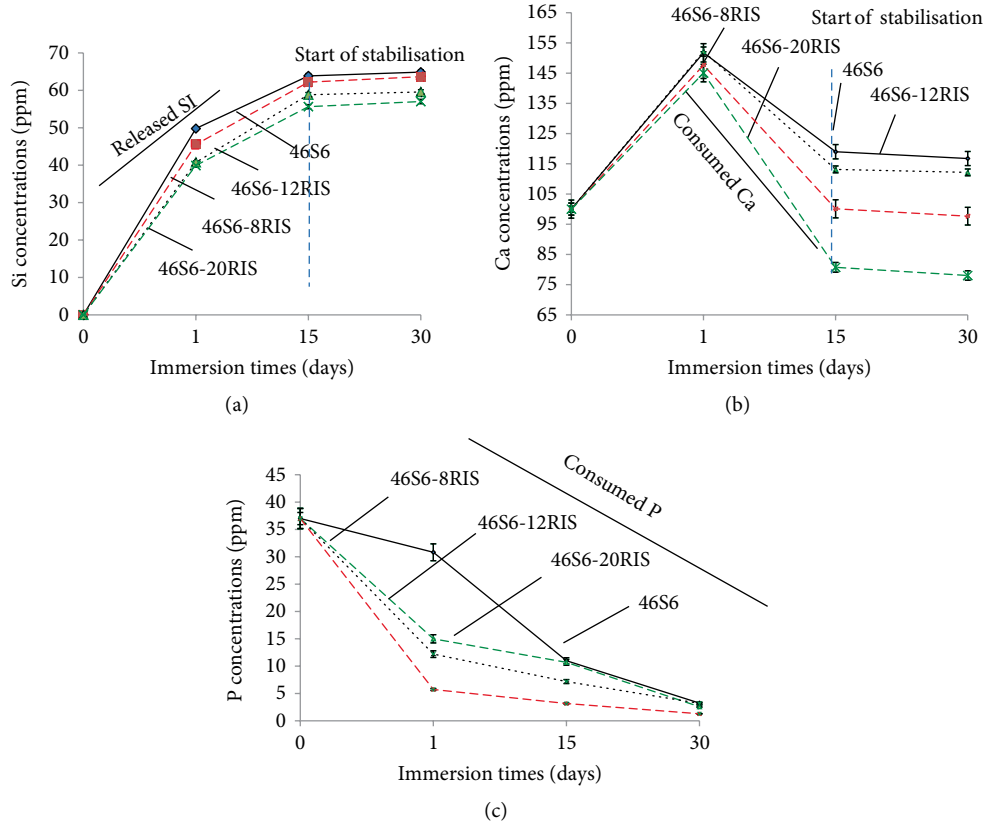
FIGURE 7: Silicon (a), calcium (b) and phosphorus (c) release after 0, 1, 15 and 30 days of immersion in the SBF solution.
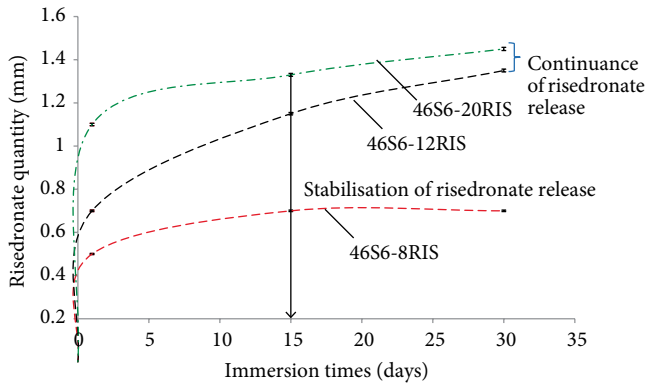
FIGURE 8: Risedronate release after 0, 1, 15 and 30 days of immersion in the SBF solution.

the risedronate keep going to release after 30 days which justify that its glasses matrix are encased by risedronate and consequently illustrates its slow degradation and the retarding of HA formation on its surface.

The in vitro accessed results conducted our in vivo experiments for the 46S6-8RIS evaluation through its implantation in osteoporotic rats.

The concentration of risedronate after 40 min of incubation was evaluated in our pervious study by the mathematical equation:

$$C_g = \frac{A}{(\varepsilon \times 1)}, \tag{1}$$

TABLE 2: Concentration of risedronate fixed on the 46S6 surface (C_f) after 40 min of incubation.

Composites	C_f (Mm)
46S6-8RIS	0.79
46S6-12RIS	1.19
46S6-20RIS	1.99

TABLE 3: Concentrations of risedronate retained on the 46S6 surface (C_r) after its immersion in the SBF solution.

Composites	C_r (Mm)		
	1 day	15 days	30 days
46S6-8RIS	0.29	0.19	0.19
46S6-12RIS	0.49	0.08	0.05
46S6-20RIS	0.79	0.47	0.39

where A is the absorbance, ε is the molar extinction coefficient (cm^2/mol); l the distance traveled by the light beam in the sample (cm).

The molar absorption coefficient was approximately 3.9×10^3 at pH 7.4 [20].

$$C_f = C_0 - C_g \tag{2}$$

C_f: risedronate fixed on the 46S6 surface after 40 min.

$$C_r = C_f - C_s \tag{3}$$

(a)

(b)

(c)
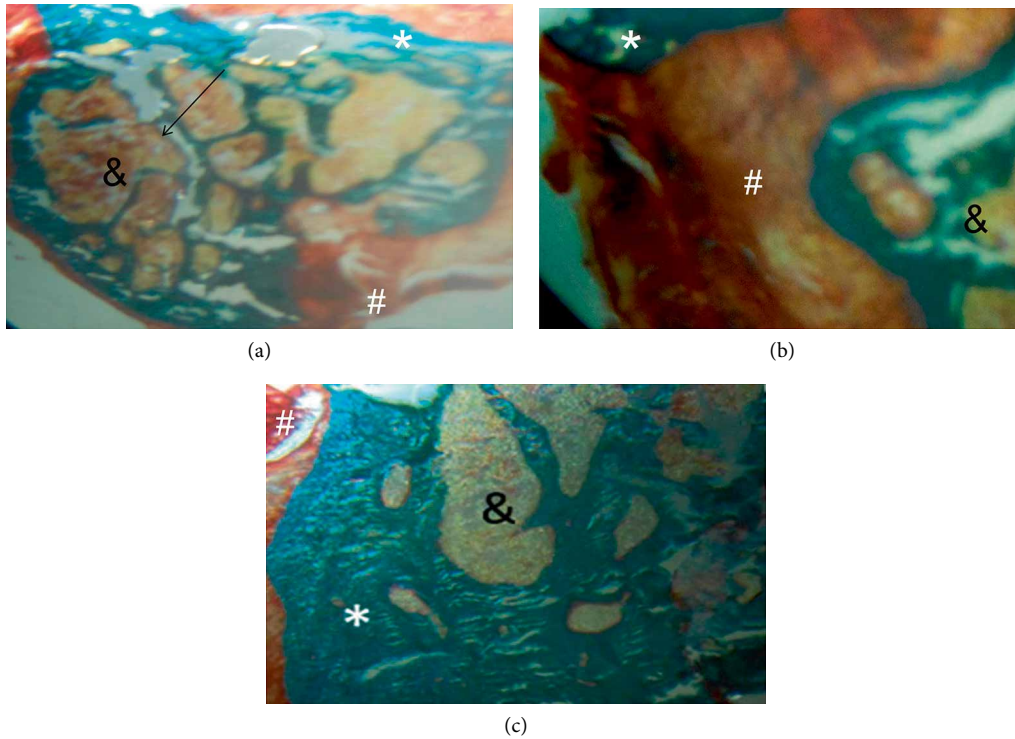
Figure 9: Histological sections stained with Goldner trichrome (×200) of ovariectomized rat (a), ovariectomized rat implanted with 46S6 (b) and ovariectomized rat implanted group with 46S6-8RIS (c) after 60 days. Arrows: indicates disconnection of bone trabeculae. ∗: Mineralized bone tissue. #: Osteoid tissue. &: Bone marrow.

(a)

(b)
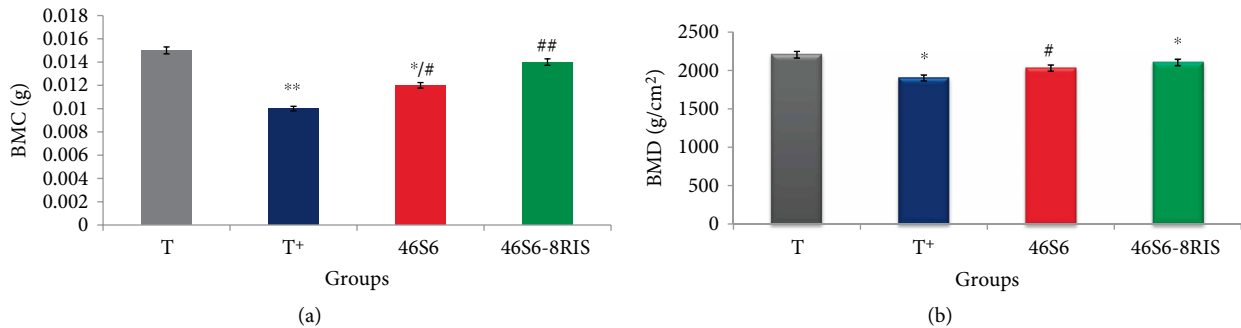
Figure 10: Bone mineral content (BMC) (a) and bone mineral density (BMD) (b) after 60 days of 46S6 and 46S6-8RIS implantation in ovariectomized rats. T: None ovariectomized and none implanted, T$^+$: Ovariectomized and none implanted, 46S6: Ovariectomized and implanted with 46S6, 46S6-8RIS: Ovariectomized and implanted with 46S6-8RIS.

C_r: risedronate retained on the 46S6 surface. C_s: risedronate released in the SBF solution.

$$C_r = C_f - C_s \qquad (4)$$

C_r: risedronate retained on the 46S6 surfaces.

3.3. Study of 46S6 and 46S6-8RIS after Implantation in the Femoral Condyle of Osteoporotic Rats.
In vitro results highlight the good chemical reactivity of the composite 46S6-8RIS. For that, we proceeded to evaluate its antiosteoporotic effect through its implantation in the femoral condyle of ovariectomized rats. Biomaterials have been inserted in the femoral condyles of rats as described in materials and methods section with respect to ethics. Sampling has been carried out 60 days after implantations.

3.3.1. Histological Evaluation.
Modified Goldner's trichrome staining was used to understand the in vivo behavior of 46S6 alone and in association with risedronate in comparison with the ovariectomized rats. Femoral condyle of OVX rats revealed the presence of thin trabeculae with reduced intertrabecular forming nodes which are most often rich in bone morrow cells characterizing osteoporotic model. Bone substance loss implanted with 46S6-8RIS implants demonstrates more advanced healing than bone treated with 46S6 alone. Mineralized tissue, sign of bone neosynthesis, was more abundant in the case of 46S6-8RIS than 46S6. This mineralization is initiated by fibro cartilaginous tissue. After 60 days of implantation, the 46S6-8RIS implant is proven to be able to generate mature bone tissue and better integrated

(a)

(b)

(c)

(d)
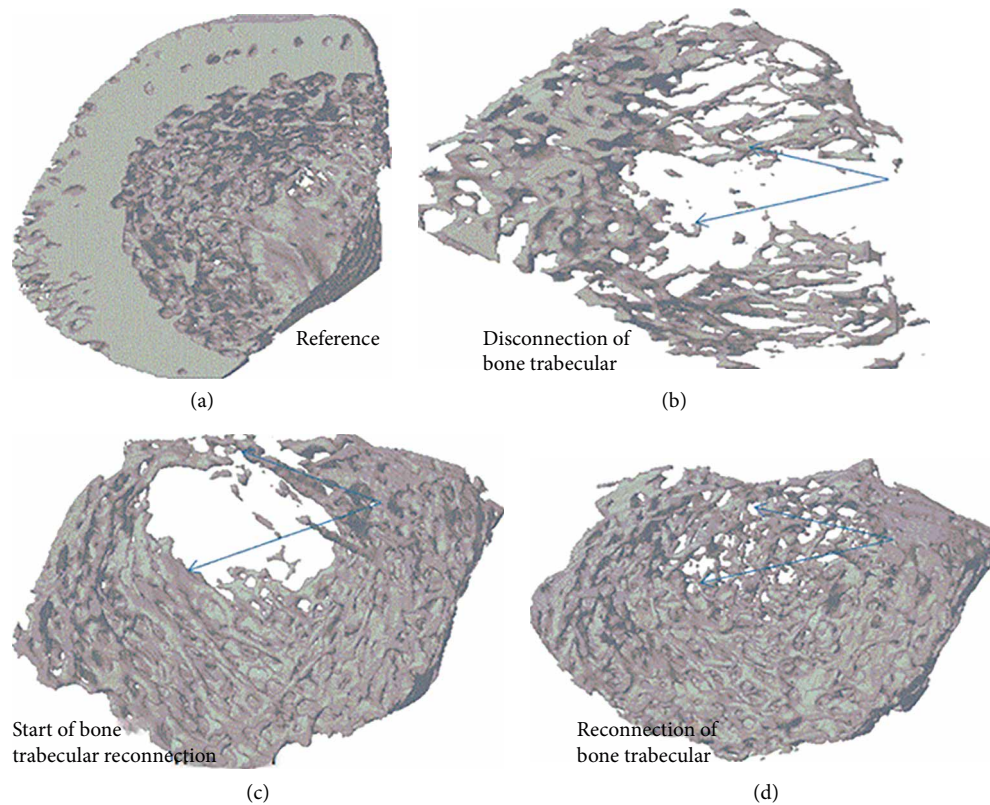
FIGURE 11: μCT image of control bone (a), ovariectomized bone (b), ovariectomized and implanted bone with 46S6 (c) and ovariectomized and implanted bone with 46S6-8RIS (d) after 60 of implantation in rats.

than the other implant. This is explained by the presence of risedronate in this composite which enhanced the osteoblastic cells formation and retard or stopped the osteoclastic formation. In fact, bisphosphonate can retard the osteoclast formation directly by the inhibition of the mevalonate pathway [27] and indirectly by the alteration of factor secretions from osteoblast, such as interleukin-6, that regulates the differentiation or activation of osteoclasts [28, 29]. This repair by the 46S6-8RIS composite essentially consists of seeing normal bone trabeculae with a well-reduced intertrabecular space. A fibro cartilaginous aspect in radiation characterizes this ossification. As well, 60 days after implantation, biomaterials were well tolerated by the surrounding bone tissue. There is no evidence of inflammation or infection at the surgical site. As a general conclusion, 60 days of 46S6-8RIS implantation is sufficient for the resorption of our material and its replacement by the newly formed bone tissue (Figure 9).

3.3.2. Bone Quality and Quantity: Assessment by MCT Scanning. In this study, the quantity and the progress of bone healing within the femoral condyle defect was evaluated by the μCT technique. Ovariectomized rats presented a significant decrease ($p < 0.05$) in bone mineral content (BMC) (Figure 10(a)) and bone mineral density (BMD) (Figure 10(b)) as compared to the control rats. Nevertheless, the implantation of these rats with 46S6-8RIS increased BMD by 10% and BMC by 80% (46S6-8RIS versus T$^+$, both $p < 0.05$).

Three-dimensional images of trabecular bones are presented in Figure 11. The OVX rats exhibited the destruction

of bone trabecular which was explained by the presence of osteoporotic phenomenon (Figure 11(b)) compared to the control group (Figure 11(a)). The implantation with 46S6 (Figure 11(c)) and 46S6-8RIS (Figure 11(d)) underlines the reconnection and the restoration of bone trabecular compared to the OVX group. Healing was remarkable after the 46S6-8RIS implantation. This result highlights the antiosteoporotic effect of risedronate. Indeed, the well regeneration of bone tissue in the implanted group with 46S6-8RIS is due to the presence of risedronate which enhance bone formation. Several studies developed the effect of bisphosphonate in the enhancement of bone restoration such as the alendronate [30].

In addition, the association of bisphosphonate with the material enhanced its fixation in the bone defect, for that, scientific experts proposed the using of bisphosphonates as coating for the fixation of orthopedic bioimplant. In fact, BPs incorporated into orthopedic implants can be used to reduce periprosthetic osteolysis at the implant/bone interface, allowing orthopedic implants to achieve a stronger primary fixation [31] by the inhibition of osteoclast action [32].

As shown in Figure 12, after 60 days of the 46S6 and 46S6-8RIS implantations in the ovariectomized rats, we revealed a modification of the trabecular architecture parameters. Indeed, we showed a significant decrease in bone volume fraction (BV/TV), trabecular number (Tb/N), and trabecular thickness (Tb/Th), respectively, with 74%, 16%, and 62% and a significant increase in trabecular bone pattern factor (Tb/PF) and trabecular spacing (Tb/Sp)), respectively, with 50% and 49% in the ovariectomized rats as compared to the control

(a)

(b)

(c)

(d)

(e)
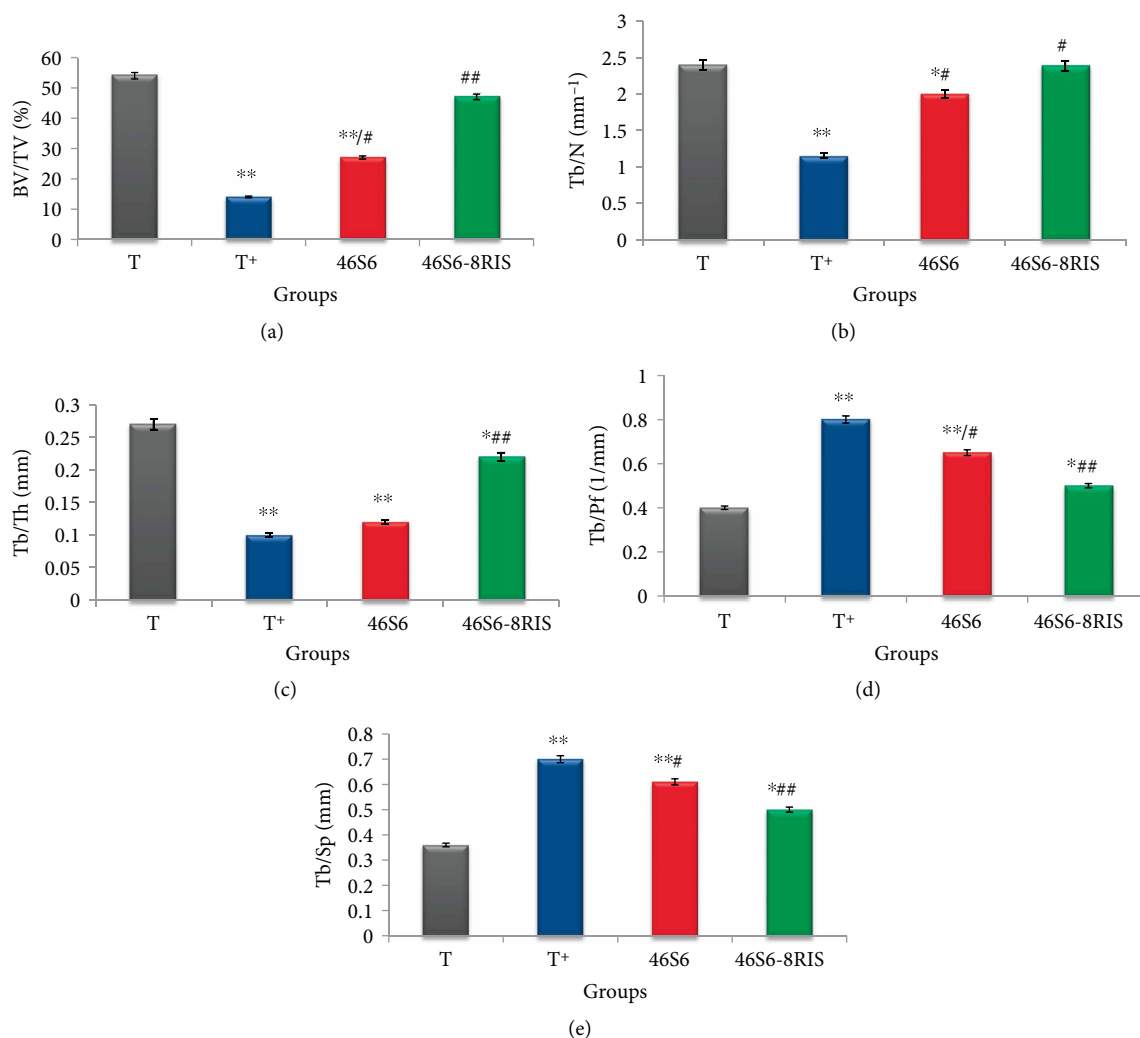
FIGURE 12: Bone volume fraction (BV/TV) (a), Trabecular Number (Tb/N) (b), Trabecular Thickness (Tb/Th) (c), Trabecular bone pattern factor (Tb/Pf) (d), and Trabecular separation (Tb/Sp) (e) after 60 days of 46S6 and 46S6-8RIS implantation in ovariectomized rats. T: None ovariectomized and none implanted, T^+: Ovariectomized and none implanted, 46S6: Ovariectomized and implanted with 46S6, 46S6-8RIS: Ovariectomized and implanted with 46S6-8RIS.

TABLE 4: Distribution of Ca, P, Si, Na, and Fe in bone of control group (T), ovariectomized (T^+) and implanted, respectively, with 46S6 and 46S6-8RIS after 60 days. $^*p < 0.01$ versus T, $^\#p < 0.01$ versus T^+ group, Values are expressed as mean ± SD of rats.

Elemental analysis Groups	Ca (mg/g)	P (mg/g)	Si (μg/g)	Na (mg/g)	Fe (μg/g)	Ca/P
T	250.0 ± 0.9	141.0 ± 0.9	26.0 ± 0.1	9.6 ± 0.1	718.0 ± 0.9	1.77
T^+	$215.0 \pm 0.7^*$	$138.0 \pm 0.8^{**}$	$25.0 \pm 0.8^{**}$	$9.0 \pm 0.5^*$	$715.1 \pm 0.8^*$	1.55
46S6	$233.1 \pm 0.8^{*\#}$	$140.1 \pm 0.8^{*\#}$	$62.0 \pm 0.8^{**\#}$	11.1 ± 0.6	725.0 ± 0.7	1.66
46S6-8RIS	$248.2 \pm 0.7^{**\#}$	$143.2 \pm 0.6^{**\#}$	$50.0 \pm 0.5^{*\#}$	10.1 ± 0.2	720.0 ± 0.9	1.73

group. Moreover, the 46S6 implantation increased the BV/TV, Tb/Th and Tb/N, respectively, with 48%, 42%, and 50% and diminished the Tb/PF by 38% and Tb/Sp by 13% as compared to the osteoporotic rats. By contrast, the 46S6-8RIS implantation expanded BV/TV by 42%, Tb/Th by 55%, and Tb/N by 16% and reduced Tb/PF by 20% and Tb/Sp by 29% as compared to the implanted group with 46S6. Consequently, the implantation of osteoporotic rats with 46S6-8RIS leads to the

reconnection of bone trabecular and the restoration of bone architectural parameters. Therefore, it restored the BMD to the initial bone quantity. This may be explained by the anti-osteoporotic effect of risedronate. Therefore, it stabilized the osteoblast and osteoclast number equilibrium in the osteoporotic bone by the inhibition of the osteoclast formation. Indeed, risedronate act directly on osteoclasts and interferes with specific intracellular biochemical processes such as

isoprenoid biosynthesis and subsequent protein prenylation to inhibit cell activity [33]. The administration of bioactive glass associated with risedronate to the osteoporotic bone induces the reconnection of bone trabecular. The quality of formed bone during the 46S6-8RIS implantation was normal and there was no evidence of impaired mineralization based on bone histomorphometrical findings.

The same results are shown after the comparison of implanted ovariectomized rats with mesoporous bioactive scaffold alone and in association with alendronate, which highlight the enhancement of bone structure and histomorphometrical parameters in the implanted group with the second composite [34], and subsequently underlined the good effect of biomaterial and bisphosphonate association for the regeneration capacity of osteoporotic bones.

3.3.3. Determination of Bone Mineral Content using ICP-OES. The intracellular and extracellular response of bioactive glass depends upon the release of soluble ionic forms of Si, Ca, P and Na from glass surface to the surrounding environment.

As shown in Table 4, the Ca and P contents for the OVX, OVX-46S6 and OVX-46S6-8RIS declined significantly when compared to the control group ($P < 0.01$). Concerning Si, Na, and Fe amounts, there are no significant variations detected in the OVX group when compared to those of the control group. The 46S6 and 46S6-8RIS implantation in the ovariectomized group enlarged the Ca and P levels; however, most amounts were revealed in the 46S6-8RIS. Simultaneously, we observed the reduction of Si content in the 46S6-8RIS compared to the 46S6. Nevertheless, Ca and P extended for the 46S6-8RIS. These data explain the speedy degradation of bioactive glass matrix and the fastest calcium phosphate layer formation at the surface of the implanted material. This finding was emphasized by the Ca/P ratio, which was about 1.66 in the 46S6 group and 1.77 in the 46S6-8RIS group. These results explained the well-crystallized and matured HA layer shown after the combination of 8% of risedronate with the glass matrix. This layer indicated the 46S6-8RIS chemical bioactivity and its transformation into biological apatite as bone. These clarify the primordial role of released risedronate from the biomaterial to surround the bone in the calcification of the newly formed bone. On the other hand, for the Fe content there are no significant variations observed in all groups. In fact, Fe trace content, performed in 46S6-8RIS-bone area, revealed the presence of cavities previously filled with red blood cells.

4. Conclusions

The chemical association of bioactive glass with risedronate by the adsorption process (46S6-8RIS, 46S6-12RIS, and 46S6-20RIS) was revealed by the perturbation of the 46S6 glass matrix and the appearance of new species (Q^4) in the ^{29}Si MAS–NMR spectrum. The in vitro study of the obtained composites was tested through its soaking in a physiological fluid and showed the retarding of 46S6-xRIS composite bioactivity with the increase in risedronate quantities added to the bioactive glass. However, the use of risedronate with less content enhances its chemical reactivity for that the good crystallized hydroxyapatite layer was detected for the 46S6-8RIS. For that,

in our in vivo experiment, we explored only the 46S6-8RIS in the goal to study its anti-osteoporotic effect after its implantation in the femoral condyle of ovariectomized rats. Sixty days after implantation, a good anti-osteoporotic performance of the 46S6-8RIS was shown by the reconnection of bone trabeculae, the enhancement of bone microarchitectural parameters, and the reestablishment of the phosphocalcic ratio (Ca/P) to the biological value. This is explained by the risedronate release and the local treatment of osteoporosis.

Data Availability

The data is presented in the PhD of Siwar Mosbahi [35]. «Etude biologique et physico-chimique de verres bioactifs/ bisphosphonates et de vitrocéramique pour le comblement des pertes osseuses chez les petits animaux». Thèse en cotutelle France-Tunisie. Université de Rennes 1, France et Université de Sfax, Tunisie, 2016, [35].

Conflicts of Interest

The authors declare that there are no conflicts of interest regarding the publication of this paper.

References

[1] K. So, S. Fujibayashi, M. Neo, Y. Anan, T. Ogawa, T. Kokubo and T. Nakamura, "Accelerated degradation and improved bone-bonding ability of hydroxyapatite ceramics by addition of glass," *Biomaterials*, vol. 27, no. 27, pp. 4738–44, 2006.

[2] C. D. Seaborn and F. H. Nielsen, "Silicon deprivation and arginine and cysteine supplementation affect bone collagen and bone plasma trace mineral concentrations in rats," *The Journal of Trace Elements in Experimental Medicine*, vol. 15, pp. 113–122, 2002.

[3] T. K. Greenlee, C. A. Beckham, A. R. Crebo, and J. C. Malmorg, "Glass ceramic bone implants," *Journal of Biomedical Materials Research*, vol. 6, no. 3, pp. 235–44, 1972.

[4] H. Oudadesse, E. Dietrich, Y. L. Gal et al., "Apatite forming ability and cytocompatibility of pure and Zn-doped bioactive glasses," *Biomedical Materials*, vol. 6, no. 3, p. 035006, 2011.

[5] M. Alcaide, P. Portolés, A. López-Noriega, D. Arcos, M. Vallet-Regí, and M T. Portolés, "Interaction of an ordered mesoporous bioactive glass with osteoblasts, fibroblasts and lymphocytes, demonstrating its biocompatibility as a potential bone graft material," *Acta Biomaterialia*, vol. 6, no. 3, pp. 892–899, 2010.

[6] O. M. Goudouri, E. Kontonasaki, N. Kantiranis et al., "A bioactive glass/dental porcelain system by the sol gel route: fabrication and characterization," *Key Engineering Materials*, vol. 3, pp. 95–98, 2008.

[7] A. Elshahat, M. A. Shermak, N. Inoue, E. Y. S. Chao, and P. Manson, "The use of novabone and norian in cranioplasty:

a comparative study," *Journal of Craniofacial Surgery*, vol. 15, no. 3, pp. 483–489, 2004.

[8] H. Oudadesse, E. Dietrich, X. V. Bui, Y. Le Gal, P. Pellen, and G. Cathelineau, "Enhancement of cells proliferation and control of bioactivity of strontium doped glass," *Applied Surface Science*, vol. 257, no. 20, pp. 8587–8593, 2011.

[9] E. Dietrich, H. Oudadesse, A. Lucas-Girot, and M. Mami, "In vitro bioactivity of melt-derived glass 46S6 doped with magnesium," *Journal of Biomedical Materials Research Part A*, vol. 88A, no. 4, pp. 1087–1096, 2007.

[10] P. T. Vallano, S. B. Shugarts, W. F. Kline, E. J. Woolf, and B. K. Matuszewski, "Determination of risedronate in human urine by column-switching ion-pair high-performance liquid chromatography with ultraviolet detection," *Journal of Chromatography B*, vol. 794, no. 1, pp. 23–33, 2003.

[11] W. Feng, J. Li, K. Zhang et al., "Multifunctional coating based on hyaluronic acid and dopamine conjugate for potential application on surface modification of cardiovascular implanted devices," *ACS Applied Materials & Interfaces*, vol. 8, no. 1, pp. 109–121, 2015.

[12] J. Li, W. Feng, K. Zhang et al., "Controlling molecular weight of hyaluronic acid conjugated on amine-rich surface: toward better multifunctional biomaterials for cardiovascular implants," *ACS applied materials and interfaces*, vol. 9, no. 36, pp. 30343–30358, 2017.

[13] S. Jebahi, H. Oudadesse, E. Wers et al., "Effect of pH and ionic exchange on the reactivity of bioglass/chitosan composites used as a bone graft substitute," *World Academy of Science, Engineering and Technology, International Journal of Materials and Metallurgical Engineering*, vol. 7, no. 5, 2013.

[14] S. Mosbahi, H. Oudadesse, B. Lefeuvre et al., "Risedronate adsorption on bioactive glass surface for applications as bone biomaterial," *Applied Surface Science*, vol. 367, pp. 205–213, 2016.

[15] S. P. Luckman, F. P. Coxon, F. H. Ebetino, R. G. G. Russell, and M. J. Rogers, "Heterocycle-containing bisphosphonates cause apoptosis and inhibit bone resorption by preventing protein prenylation: evidence from structure-activity relationships in J774 macrophages," *Journal of Bone and Mineral Research*, vol. 13, no. 11, pp. 1668–1678, 1998.

[16] E. Van Beek, C. Löwik, I. Que, and S. Papapoulos, "Dissociation of binding and antiresorptive properties of hydroxyl bisphosphonates by substitution of the hydroxyl with an amino group," *Journal of Bone and Mineral Research*, vol. 11, pp. 1492–1497, 1996.

[17] J. J. Benedict, "The physical chemistry of the diphosphonates—its relationship to their medical activity," vol. 12, in *In Symposium CEMO (Centre d'Etude des Maladies Ostéoarticulaires de Genève) IV. Diphosphonates and bone*, A. Donath and B. Courvoiser, Ed., pp. 1–19Nyon Switzerland, Editions Médecine at Hygiène, Geneva, 1982.

[18] H. Oudadesse, E. Wers, X. V. Bui et al., "Chitosan effects on glass matrices evaluated by biomaterial. MAS-NMR and biological investigations," *Korean Journal of Chemical Engineering*, vol. 30, no. 9, pp. 1775–1783, 2013.

[19] P. T. Vallano, S. B. Shugarts, and W. F. Kline, "Determination of risedronate in human urine by column-switching ion-pair high-performance liquid chromatography with ultraviolet detection," *Chromatogr*, vol. 794, pp. 23–33, 2003.

[20] F. Errassi, S. Sarda, A. Barroug, A. Legrouri, H. Sfihi, and C. Rey, "Infrared, Raman and NMR investigations of risedronate adsorption on nanocrystalline apatites," *Journal of Colloid and Interface Science*, vol. 420, pp. 101–111, 2014.

[21] X. V. Bui, H. Oudadesse, Y. Le Gal, A. Mostafa, P. Pellen, and G. Cathelineau, "Chemical reactivity of biocomposite glass-zoledronate," *Journal of the Australian Ceramic Society*, vol. 46, pp. 24–28, 2010.

[22] R. G. G. Russell, "Bisphosphonates: from bench to bedside," *Annals of the New York Academy of Sciences*, vol. 1068, no. 1, pp. 367–401, 2006.

[23] Ö. H. Andersson and K. H. Karlsson, "On the bioactivity of silicate glass," *Journal of Non-Crystalline Solids*, vol. 129, no. 1-3, pp. 145–151, 1991.

[24] E. Dietrich, H. Oudadesse, A. Lucas-Girot, and M. Mami, ""In vitro" bioactivity of melt-derived glass 46S6 doped with magnesium," *Journal of Biomedical Materials Research Part A*, vol. 88, no. 4, pp. 1087–1096, 2008.

[25] S. Boulila, ""In vitro" and "in vivo" behavior of porous glasses composite: bone assimilation, physiological and physicochemical explorations," *Thesis under joint supervision: France-Tunisia*, University of Rennes 1, France and University of Sfax, 2016.

[26] H. L. Benford, J. C. Frith, S. Auriola, J. Mönkkönen, and M. J. Rogers, "Farnesol andgeranylgeraniol prevent activation of caspases by amino bisphosphonates: biochemical evidence for two distinct pharmacological classes of bisphosphonate drugs," *Molecular Pharmacology*, vol. 56, no. 1, pp. 131–140, 1999.

[27] J. Fisher, M. Rogers, J. Halasy et al., "Alendronate mechanism of action: geranylgeraniol, an intermediate in the mevalonate pathway, prevents inhibition of osteoclast formation, bone resorption, and kinase activation in vitro," *Proceedings of the National Academy of Sciences*, vol. 96, no. 1, pp. 133–138, 1999.

[28] C. Vitte, H. Fleisch, and H. Guenther, "Bisphosphonates induce osteoblasts to secret an inhibitor of osteoclast-mediated resorption," *Endocrinology*, vol. 137, pp. 2324–2333, 1996.

[29] J. L. Sanderes, G. Tarjan, S. A. Foster, and P. H. Stern, "Alendronate/interleukin-1b cotreatment increases interleukin-6 in bone and UMR-106 cells: dose dependenceand relationship to the antiresorptive effect of alendronate," *Journal of Bone and Mineral Research*, vol. 13, no. 5, pp. 786–792, 1998.

[30] R. Pignatello, E. Cenni, D. Micieli et al., "A Novel biomaterial for osteotropic drug nanocarriers: synthesis and biocompatibility evaluation of a PLGA—ALE Conjugate," *Nanomedicine*, vol. 4, no. 2, pp. 161–175, 2009.

[31] M. Hilding, L. Ryd, S. Toksvig-Larsen, and P. Aspenberg, "Clodronate prevents prosthetic migration: a randomized radiostereometric study of 50 total knee patients," *Acta Orthopaedica Scandinavica*, vol. 71, no. 6, pp. 553–557, 2000.

[32] V. Stadelmann, O. Gauthier, A. Terrier, J. Bouler, and D. Pioletti, "Implants delivering bisphosphonate locally increase periprosthetic bone density in an osteoporotic sheep model. A pilot study," *European Cells and Materials*, vol. 16, pp. 10–16, 2008.

[33] X. Wang, D. Zeng, W. Weng et al., "Alendronate delivery on amino modified mesoporous bioactive glass scaffolds toenhance bone regeneration in osteoporosis rats," *Artificial Cells, Nanomedicine, and Biotechnology*, vol. 46, no. S2, pp. S171–S181, 2018.

[34] B. Borah, E. L. Ritman, T. E. Dufresne et al., "The effect of risedronate on bone mineralization as measured by microcomputed tomography with synchrotron radiation:

correlation to histomorphometric indices of turnover," *Bone*, vol. 37, no. 1, pp. 1–9, 2005.

[35] S. Mosbahi, "Biological and physicochemical study of bioactive/ bisphosphonate and porous glass ceramic for the filling of bone loss in animals," *Thesis under joint supervision: France-Tunisia*, University of Rennes 1, France and University of Sfax, Tunisia, 2016.

Research Article

Immobilization of Fibronectin-Loaded Polyelectrolyte Nanoparticles on Cardiovascular Material Surface to Improve the Biocompatibility

Shihui Liu (iD),[1] **Youdong Hu** (iD),[2] **Rongrong Tao,**[1] **Qingwei Huo,**[1] **Lin Wang,**[1] **Chunzhi Tang,**[1] **Changjiang Pan,**[3] **Tao Gong,**[3] **Nenggui Xu** (iD),[1] and **Tao Liu** (iD)[1]

[1]*Medical College of Acu-Moxi and Rehabilitation, Guangzhou University of Chinese Medicine, Guangzhou 510006, China*
[2]*Department of Geriatrics, The Affiliated Huai'an Hospital of Xuzhou Medical College, Huai'an 223002, China*
[3]*Jiangsu Provincial Key Laboratory for Interventional Medical Devices, Huaiyin Institute of Technology, Huai'an 223003, China*

Correspondence should be addressed to Nenggui Xu; ngxu8018@gzucm.edu.cn and Tao Liu; lt045021@gzucm.edu.cn

Vascular stent interventional therapy is the main method for clinical treatment of coronary artery diseases. However, due to the insufficient biocompatibility of cardiovascular materials, the implantation of stents often leads to serious adverse cardiac events. Surface biofunctional modification to improve the biocompatibility of vascular stents has been the focus of current research. In this study, based on the structure and function of extracellular matrix on vascular injury healing, a novel fibronectin-loaded poly-l-lysine/heparin nanoparticles was constructed for stent surface modification. *In vitro* blood compatibility evaluation results showed that the nanoparticles-modified surface could effectively reduce platelet adhesion and activation. *In vitro* cellular compatibility evaluation results indicated that the nanocoating may provide adequate efficacy in promoting the adhesion and proliferation of endothelial cells and thereby accelerate endothelialization. This study provides a new approach for the surface biological function modification of vascular stents.

1. Introduction

Cardiovascular diseases (CVDs), such as coronary artery diseases (CADs), continue to be the leading cause of death globally [1]. Although the extensive clinical application of vascular stents has significantly improved the survival rate of patients with CADs, adverse cardiac effects caused by in-stent thrombosis and restenosis often lead to implantation failure [2]. With the in-depth exploration of the mechanism of pathological response induced by material implantation, it is widely accepted that the rapid endothelialization on the surface of cardiovascular materials after implantation is an ideal way to reduce the risk of postoperative complications. Currently, in-situ regulation of platelets and vascular cells behavior via surface biological function design and microenvironment construction has become a hot topic [3].

In the human body, the repair of vascular endothelium depends largely on the existence of vascular basement membrane [4], which is a kind of extracellular matrix composed of laminin, collagen, nestin, and heparin sulfate polysaccharide. Because of the important role of extracellular matrix components in cell growth, extracellular matrix proteins are also commonly used in surface modification of biomaterials to promote the growth behavior of vascular cells. Matrix proteins and some adhesive proteins, such as fibronectin (Fn) [5, 6], laminin (Ln) [7, 8], and collagen (Col) [9, 10], may bind to the specific receptors that are expressed on endothelial cells (ECs) and initiate a variety of intracellular pathways so as to promote a series of biological behaviors, such as cell adhesion, migration, growth, and proliferation. However, extracellular matrix components can not only promote cell growth but also lead to platelet adhesion and activation and then cause thrombosis [11, 12],

which greatly limits the application of extracellular matrix coating in the field of cardiovascular materials. Therefore, it is necessary to find a way to construct the biological coating that may provide adequate properties to inhibit the function of protein molecules in promoting coagulation reaction without affecting the positive efficacy on endothelium regeneration.

Construction of multifunctional layer containing anticoagulant molecules and adhesive proteins on the surface of cardiovascular materials would be helpful to realize the selective regulation of the biological behavior of blood components and vascular cells and then to inhibit thrombus and restenosis, as well as accelerate endothelialization. However, in the current research on surface biological modification of cardiovascular materials, many functional coatings were often found having few beneficial effects on the direction of vascular neointimal regeneration. The main reasons are as follows: First, the limitations of the construction methods of biological coatings on materials surface, for example, the introduction of biomolecules on the surface of materials by covalent immobilization, may lead to the decrease of biological activity [13], while the biological coatings constructed by the interaction between biomolecules (such as electrostatic assembly) also have the defects of intermolecular functional domain shielding and lack of stability. Second, the constructed biological functional layer is not effective for a long time in vivo, so it is easy to release or degrade in the complex dynamic environment of the body and lose its functional activity rapidly. In recent years, multifunctional nanoparticles have gradually shown great potential in the controlled release of biomolecules and the regulation of cellular behavior [14, 15]. Compared with other controlled release systems, the unique nanoeffect of nanoparticles system greatly increases its loading capacity and can separate the active molecules from the surrounding environment to avoid rapid inactivation [16].

In our previous studies, we constructed a novel heparin/poly-l-lysine nanoparticle for surface modification of cardiovascular materials and found that the nanocoating can effectively improve the anticoagulant properties [17]. In order to further enhance its potential to promote endothelial regeneration, fibronectin was loaded onto nanoparticles to provide sufficient cell binding sites to accelerate endothelialization after stent implantation. It was found that the nanoparticles could be successfully immobilized to the dopamine-coated surface and the modified surface exhibits proper functions of inhibiting coagulation reaction and promoting the adhesion and proliferation of endothelial cells. This study provides a feasible method for surface biological function modification of cardiovascular materials.

2. Materials and Methods

2.1. Materials and Reagents.
316L stainless steel (316L SS) was processed into round shape (Φ10 mm, ~1.2 mm thickness) and mirror-polished. Fibronectin (Fn), dopamine (DA), and poly-l-lysine (PLL, MW 150~300 KDa) were purchased from Sigma-Aldrich. Low molecular weight heparin sodium (Hep, ≥180 U/mg), acid orange II (AO II),

toluidine blue O (TBO), and rhodamine 123 were purchased from Aladdin BioChem Technology Co., Ltd (Shanghai, China). 0.0067 M phosphate-buffered saline (PBS, pH 7.4) was used for PLL, Hep, and Fn solution preparation.

2.2. Preparation of Fn-Loaded Hep/PLL Nanocoating on 316L SS Surface.
As shown in Figure 1, the nanoparticles were immobilized on the DA-coated 316L SS surface. A detailed protocol for DA coating deposition can be referred to our previous study [7]. For nanoparticle preparation, 100 μg/ml Fn solution was mixed with an equal volume of 10 mg/ml heparin solution and incubated at 37°C for 3 h. Then, 0.5 mg/ml PLL solution was added dropwise to equal volume of Hep/Ln mixture under high-frequency ultrasonic conditions to formulate the Fn-loaded Hep/PLL nanoparticles. After that, DA-coated 316L SS was placed in a 24-well plate and 0.5 ml of nanoparticle suspension was added to the sample surface. The plate was subsequently placed in an air bath shaking table and incubated at 37°C for 12 h with gentle shaking (60–65 rpm) (termed as SS-DA-NPF). The sample modified with only Hep/PLL nanoparticle was set as the control group and termed as SS-DA-NP.

2.3. Size and Zeta Potential Analysis.
The size, zeta potential, and particle dispersion index (PDI) of prepared nanoparticles were characterized by dynamic light scattering using a ZETA-SIZER, MALVERN Nano-2S90 (Malvern Ltd., Malvern, UK).

2.4. FTIR Assay.
The alteration of surface chemical structure during surface modification was detected by Fourier transform infrared spectroscopy (FTIR). The FTIR assay is carried out by using the attenuated total reflection (ATR) model on the Tensor-27 infrared spectrum (Bruker, Germany). The infrared adsorption between 4000 and 650 cm^{-1} was recorded at room temperature and atmospheric conditions.

2.5. Quantitative Characterization of Amine Group and Heparin Exposing Density.
Surface amine density was detected by the AO II method. The samples were initially immersed in 1 ml of 0.5 mM AO II solution (in pH = 3 HCl) and incubated at 37°C for 6 hours with gentle shaking. Afterward, the samples were thoroughly rinsed with HCl solution (pH = 3). Then, the samples were placed on a filter paper, and the surface was dried with a gentle blow. Next, the samples were immersed in 1 ml of NaOH water solution (pH = 12) and shaken at 37°C for 30 minutes. Finally, 150 μl of NaOH solution mixed with eluted AO II was transferred into a 96-well plate, and the absorbance value was detected at 485 nm. The AO II molar concentration was parallel to that of the amine group.

TBO assay was prepared to detect heparin exposing density of nanoparticle-modified surfaces. First, the samples were placed in a centrifuge tube, and 5 ml of 0.04 wt.% TBO solution (in 0.01 M HCl/0.2 wt.% NaCl solution) was added. The tube was subsequently placed in an air bath shaker and
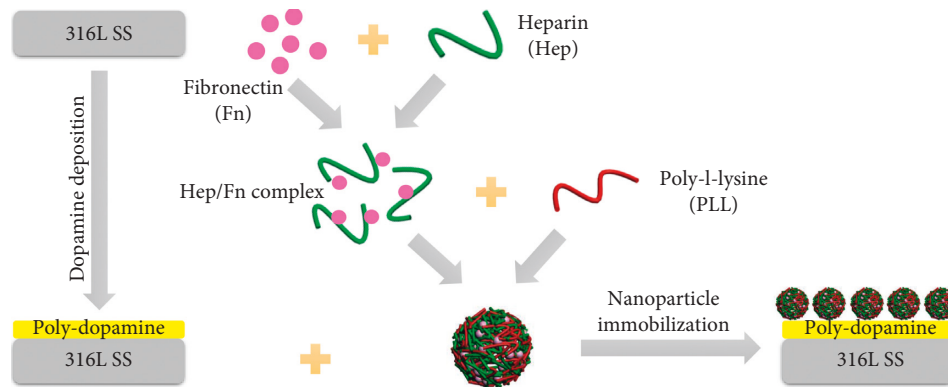
Figure 1: Schematic drawing of fibronectin-loaded nanoparticles fabrication and immobilization.

incubated at 37°C for 4 hours with gentle shaking (~60 rpm). Next, the samples were thoroughly rinsed with UP water and immersed in 5 ml of 80% ethanol/0.1 M NaOH (v/v = 4/1) solution. After being shaken for 10 minutes, the solution mixed with eluted TBO was transferred to a 96-well plate, and the absorbance value was detected at 530 nm.

2.6. Water Contact Angle and AFM Assay. The alteration of surface hydrophilicity during nanoparticles modification was detected by using a DSA25 contact goniometer (Krüss GmbH, Germany). The test was carried out at room temperature, and at least 3 independent points of each sample were measured.

The morphology of nanoparticles-modified surface was detected by atom force microscopy (AFM) (Bruker Innova, Germany). The test was conducted at room temperature, and the image was processed by NanoScope Analysis software.

2.7. In Vitro Platelet Adhesion Assay. Human whole blood was taken from healthy volunteers. The blood that was anticoagulated by using 3.8% sodium citrate (1/10 in volume ratio) was firstly centrifuged at 1500 rpm for 15 min to acquire platelet-rich plasma (PRP). The sample was then placed in a 24-well plate, and 0.5 ml PRP was added to each well to ensure that the sample was fully immersed in PRP. Subsequently, the plate is placed in a constant-temperature water bath shaker and incubated at 37°C for 2 hours with gentle shaking. After that, the sample was rinsed with normal saline and the platelets adhered on the surface were fixed in 2.5% glutaraldehyde for over 12 hours. For platelets fluorescence staining, $50\,\mu$l of $1\,\mu$g/ml rhodamine 123 solution was added to each sample surface and incubated at room temperature for 20 min. The morphology of adherent platelets was observed under an inverted fluorescence microscope.

P-selectin expression was detected to evaluate the platelet activation profile on different sample surface. A detailed protocol can be referred to our previous study [7].

2.8. ECs Adhesion and Proliferation Assay. Endothelial cells (ECs) were isolated from human umbilical cord veins and cultured in DMEM/F12 medium containing 15% fetal bovine serum (FBS) and $20\,\mu$g/ml ECGS. The culture medium was changed every 2 days. The cells were isolated with 0.25% trypsin/EDTA solution when the fusion degree was over 85% and adjusted to 1×10^5 cell/ml by using fresh culture medium for subsequent cell seeding.

316L SS and SS-DA that were used for cell seeding were presterilized by high pressure steam, and the immobilization of nanoparticles was carried out under aseptic conditions. All samples were placed in a 24-well plate, and 1 ml EC suspension was added to each well and incubated at 37°C under 5% CO_2 for 1 and 3 days, respectively. At each time point, the culture medium was removed and the fresh medium containing 10% CCK-8 reagent was added to the culture for 3.5 hours. After that, the absorbance of the culture medium at 450 nm was detected to evaluate the cell proliferation activity on different sample surfaces. Then, the samples were fixed in 2.5% glutaraldehyde solution for subsequent cell fluorescence staining. A detailed experimental protocol can be referred to our previous study [7].

2.9. Statistical Analysis. At least three independent experiments were performed for the tests described above. The data were analyzed with the software SPSS 22.0. Statistical evaluation of the data was performed using one-way ANOVA. The probability value $p < 0.05$ was considered significant.

3. Results and Discussion

3.1. Size and Zeta Potential Analysis. According to Table 1, the average size of blank nanoparticles is 313 ± 19 nm. After loading Fn, the particle size decreased slightly (287 ± 26 nm), which was mainly due to the increase of the internal force caused by the interaction between Fn and heparin, which enhanced the compactness of the particles. The results of zeta potential show that the incorporation of Fn has no significant effect on the charge of nanoparticles, which may be partly related to the lower Fn concentration when compared with heparin and PLL. On the other hand, the absolute values of zeta potential of both NP and NPF are higher than 20 mV, which indicates that the particle system has adequate stability. Besides, for nanoparticle system, it is generally considered that the particle size is more uniform

TABLE 1: Size and zeta potential of prepared nanoparticles.

	Zeta potential (mV)	Size (nm)	PDI
NP	−27.3 ± 0.5	313 ± 19	0.102 ± 0.052
NPF	−26.2 ± 1.4	287 ± 26	0.049 ± 0.011

when the dispersion coefficient (PDI) is less than 0.2, and the lower the dispersion coefficient, the better the uniformity. The results show that the PDI values of the prepared nanoparticles are lower than 0.2, indicating that both NP and NPF are of favorable uniformity.

3.2. FTIR Assay. Figure 2 shows the infrared spectroscopy of NP- and NPF-modified surface. According to the result, for the DA-coated surface, the peaks related to benzene ring structure could be observed at $1600\,cm^{-1}$ and $1502\,cm^{-1}$, which indicates the success deposition of dopamine coating. By comparison, obvious new absorption peaks were emerged after immobilization of NP and NPF. In detail, the absorption peaks in the range of 2850–$3000\,cm^{-1}$ are related to the vibration of $-CH_3$ and $-CH_2-$ groups. The new peaks at $1666\,cm^{-1}$ and $1545\,cm^{-1}$ are related to the stretching vibration of amide I and amide II from PLL molecular structure, respectively. In addition, the new peak at $1230\,cm^{-1}$ is related to the vibration of C-O-S and S=O groups, and the peak at $1062\,cm^{-1}$ is related to the vibration of C-O-C group. Both of these two peaks further demonstrated the existence of heparin.

The above results show that both NP and NPF are successfully immobilized on the dopamine-coated surface. On the other side, when compared with the NP-modified surface, the peak intensity of amide bond on the NPF-modified surface is obviously increased at the same coordinate, which may be related to the existence of Fn in nanoparticles, or to the difference in the immobilization density between NP and NPF.

3.3. Quantitative Characterization of Heparin and Amine Exposing Density. The quantitative results of amine group and heparin exposing density on the surface of different samples are shown in Figure 3. The results show that there is a small amount of amine group ($1.42 \pm 0.33\,nmol/cm^2$) on the DA surface; however, after NP immobilization, the exposure density of amine group was greatly increased ($7.2 \pm 1.4\,nmol/cm^2$). This was mainly due to the PLL used in this study is an amino-rich polycationic electrolyte. When compared with NP, the amine exposing density on NPF-modified surface is further increased, which was mainly related to the existence of the Fn molecule. The immobilization of nanoparticles on the DA-coated surface largely depends on the chemical reaction between amino groups and quinoid groups; thereby, the increase of amino density may promote the immobilization of nanoparticles on the surface. As demonstrated, the exposure density of heparin on the NP surface was $12.38 \pm 1.87\,\mu g/cm^2$, while that of the NPF-modified sample increased to $14.72 \pm 2.23\,\mu g/cm^2$. The results also proved the conclusions of the FTIR results.
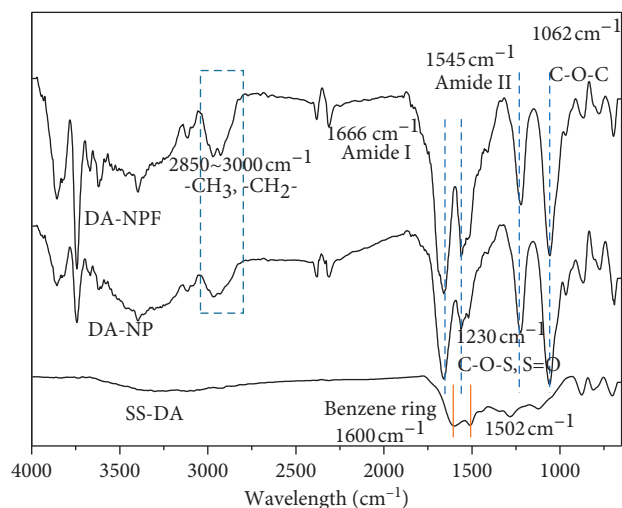
FIGURE 2: Surface chemical composition determined by FTIR spectra.
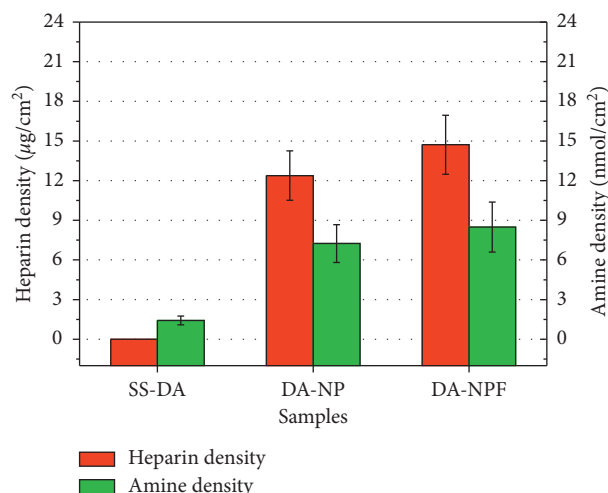
FIGURE 3: Quantitative characterization result of amine group and heparin exposing density of different sample surfaces (mean ± SD, $n = 6$).

On the other hand, according to our previous study [17], it is found that a certain amine group (0–$13\,nmol/cm^2$) and heparin exposing density (3–$10\,\mu g/cm^2$) on material surface are helpful to the selective regulation of blood and cellular behavior. In this study, the surface amine and heparin exposing densities detected are in the above range, so the modified surface may provide favorable efficacy in regulating the biological behavior of platelet and vascular cells.

3.4. Surface Physical and Chemical Properties. The hydrophilic and hydrophobic properties of the material surface can be simply characterized by the measurement of water contact angle. According to Figure 4, when compared with 316L SS, the water contact angle increased slightly after dopamine deposition. This is mainly due to the hydrophobic benzene ring structure on the SS-DA surface. After

316L SS

SS-DA

42.1 ± 2.1°

49.5 ± 1.1°

DA-NP

DA-NPF

33.5 ± 1.4°

26.7 ± 4.1°
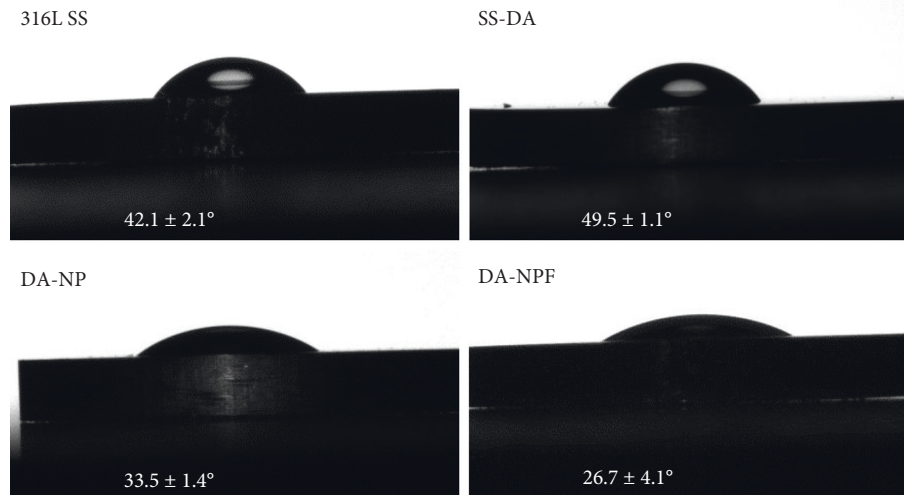
Figure 4: Alteration of surface hydrophilicity during surface modification (mean ± SD, $n = 6$).

immobilization of NP, the water contact angle was significantly decreased ($^* p < 0.05$); this is mainly due to that the heparin and PLL molecules contained a variety of hydrophilic groups, such as -COOH, -NH$_2$, and -SO$_3$. In comparison, the hydrophilicity of NPF-modified surface was further increased. This may be related to the increase of heparin and amine exposing density on the surface, which increases the content of hydrophilic groups on the surface.

According to the study, when the water contact angle is in the range of 30~60 degree, the biomaterial surface may facilitate cell adhesion and proliferation via preferentially adsorption of adhesive serum proteins, such as collagen, fibronectin, or vitronectin [18, 19]. In addition, the increase of hydrophilicity on the surface of the sample will trigger the desorption of viscous proteins [20], which is helpful to reduce the adhesion and aggregation of platelets on the surface of the material. In this study, thereby, the NP- and NPF-modified surface may provide adequate hydrophilicity to regulate platelets and vascular cells behavior.

Figure 5 shows the AFM morphology of the sample surface before and after modification of nanoparticles. It can be observed that the SS-DA surface is relatively smooth with existence of few small particles, which is mainly formed during the self-polymerization of dopamine. In comparison, both NP- and NPF-modified surface showed obvious particle structure, and the particle size is about 300 to 400 nm, which is consistent with the results shown in Table 1. In addition, no obvious particle aggregation was found on the NP- and NPF- modified surface. This may be related to the high zeta potential value of prepared nanoparticles, which can effectively inhibit the agglomeration of particles during the process of immobilization.

3.5. In Vitro Platelet Adhesion Assay. As a blood contact device, favorable hemocompatibility was usually taken into first consideration. In this study, *in vitro* platelet adhesion and activation were prepared to evaluate the anticoagulation efficacy of the modified surface. Figure 6(a) shows the results of rhodamine 123 staining of adherent platelets after incubation in platelet-rich plasma for 2 hours. It can be seen that there are a large number of platelets adhered to the surface of SS and SS-DA; in particular, serious aggregation of platelets could be observed on SS-DA surface, which indicates that the blood compatibility of the sample is poor. For the NP- and NPF-modified surfaces, the platelet adhesion density was dramatically decreased, and no obvious platelet aggregation and activation were found. P-selectin expression result further demonstrated that the NP- and NPF-modified surface may inhibit platelet activation (Figure 6(b)). Although numerous studies have shown that fibronectin is a procoagulant [21, 22], the biological function of the modified surface is closely associated with the synergistic effect of different biomolecules. The heparin density on the surface of NPF-modified samples is relatively high, which can effectively block the coagulation pathway, inhibit platelet adhesion and activation, and thereby improve blood compatibility.

3.6. ECs Adhesion and Proliferation Assay. The effect of modified surface on ECs adhesion and proliferation behavior is shown in Figure 7. Rhodamine 123 fluorescence staining result (Figure 7(a)) shows that ECs displayed a well-spread morphology on 316L SS and SS-DA surface. In comparison, the cell coverage area on NP-modified surface was significantly decreased and showed a shrinkage morphology after incubation for 1 and 3 days, which indicated the activity of adhered ECs was poor. For the NPF-modified surface, the ECs adhesion density was obviously increased, and the adherent cells showed classical cobblestone morphology. CCK-8 assay was used to further detect the proliferation activity of adherent cells. As shown in Figure 7(b), the NP-modified surface showed the lowest CCK-8 value after 1- and 3-day culture, while the proliferation activity was significantly increased ($^* p < 0.05$) on the NPF surface. The EC proliferation ratio from day 1 to 3 further demonstrates that surface modification with NPF may accelerate endothelialization (Figure 7(c)).
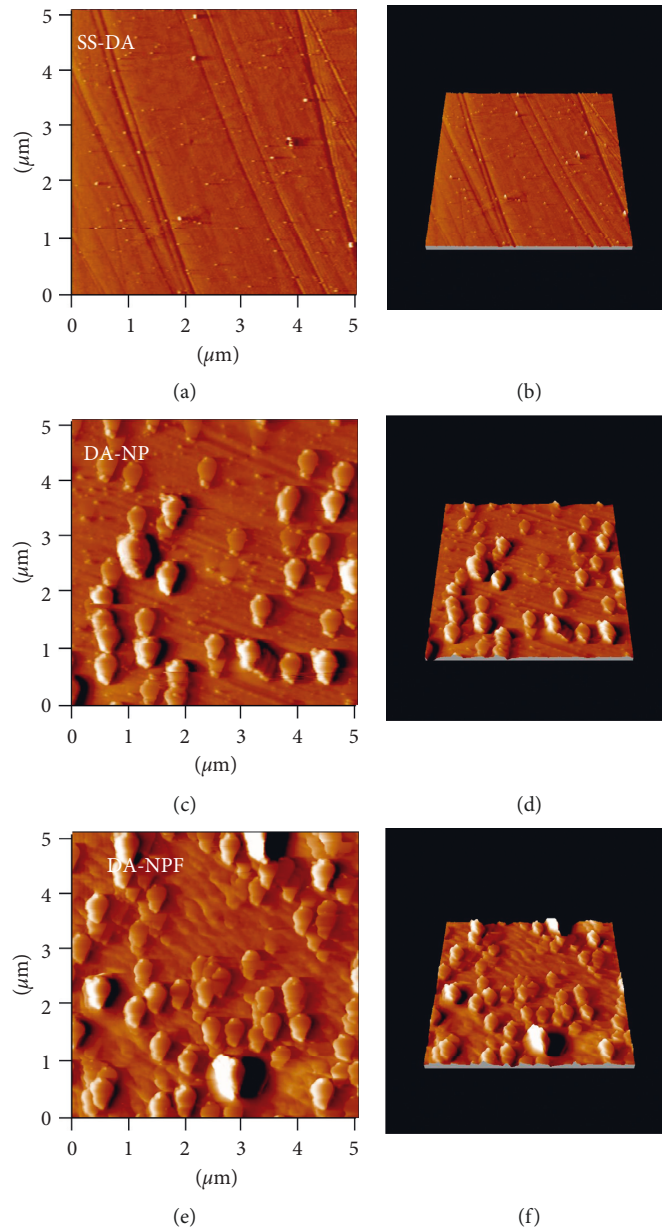
FIGURE 5: Morphology of nanoparticles-modified surface determined by AFM.

Rapid endothelialization is one of the most important requirements for the surface modification of vascular stents. For biofunctionalized surface, the biocompatibility is closely related to the surface physicochemical characteristics and biological properties. In particular, the synergistic effect of a variety of biomolecules plays an important role in the regulation of tissue-material interface response. In this study, the cell adhesion density and proliferation activity of NP-modified surface significantly decreased; this is mainly due to the high density of heparin on the modified surface. According to our previous study, the heparinized surface may inhibit cell growth when heparin-binding density is more than $10 \mu g/cm^2$ [17]. This is mainly related to the high negative charge of heparin, which may trigger the blocking effect to some important intracellular signaling pathways that closely associate with cell adhesion and proliferation behavior [23–25]. On the other hand, although the NPF-modified surface showed higher heparin exposing density, the incorporation of Fn may bring abundant cell adhesion sites, and therefore, the cell proliferation activity was enhanced. In summary, the surface of NPF modified samples not only showed adequate efficacy of inhibiting platelet adhesion and activation but also exhibited favorable property of accelerating endothelialization, both of which are helpful to improve the clinical performance of biomaterials implanted into blood vessels.

(a)

(b)
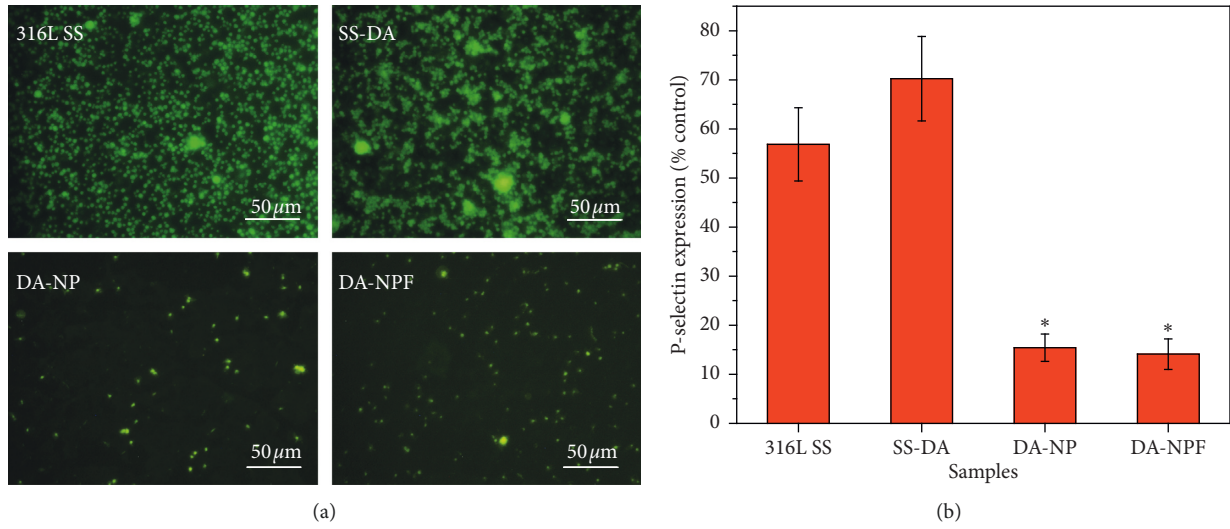
FIGURE 6: *In vitro* blood compatibility evaluation result. (a) Rhodamine 123 fluorescence staining of adhered platelets. (b) P-selectin semiquantitative characterization result (mean ± SD, $n = 6$; $^{*}p < 0.05$ indicates significant difference in comparison with 316L SS and SS-DA).

(a)

(b)

(c)
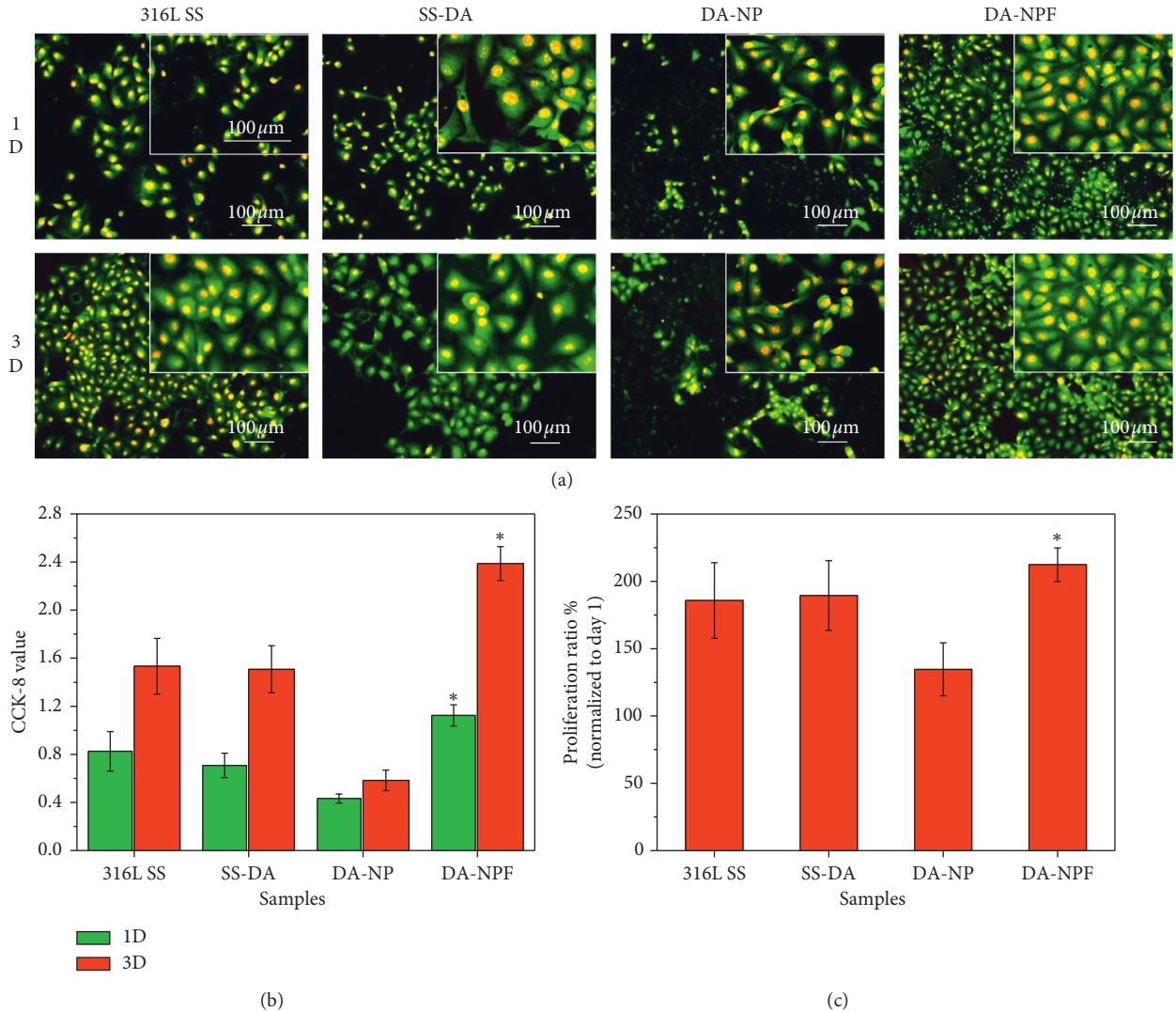
FIGURE 7: (a) Rhodamine 123 and DAPI fluorescence staining of adhered ECs after culture of 1 and 3 days. (b) Cell proliferation activity detected by CCK-8. (c) Cell proliferation ratio from day 1 to 3. (mean ± SD, $n = 12$; $^{*}p < 0.05$ indicates significant difference).

4. Conclusion

In this study, novel Fn-loaded heparin/poly-l-lysine nanoparticles were constructed and immobilized to dopamine-coated 316L SS surface to improve the biocompatibility. It is found that the incorporation of Fn can improve the binding density of nanoparticles, which may contribute to enhancing the anticoagulant properties of the surface and thereby prevent the coagulation reaction caused by the presence of Fn. In addition, the Fn-loaded nanocoating was found to effectively improve the adhesion and proliferation of vascular endothelial cells on the material surface and thereby accelerate endothelium regeneration. Molecular biological mechanism of the synergistic effects among different biomolecules in vascular remodeling and endothelium regeneration will be investigated in future studies.

Data Availability

All data and models used to support the findings of this study are available from the corresponding author upon request.

Conflicts of Interest

The authors declare there are no conflicts of interest regarding the publication of this paper.

Authors' Contributions

Shihui Liu and Youdong Hu contributed equally to this work and should be considered as the co-first authors.

Acknowledgments

References

[1] World Health Organization, Factsheets, Cardiovascular Diseases (CVDs), 2017, https://www.who.int/en/news-room/fact-sheets/detail/cardiovascular-diseases-(cvds).

[2] K. Yahagi, F. D. Kolodgie, F. Otsuka et al., "Pathophysiology of native coronary, vein graft, and in-stent atherosclerosis," *Nature Reviews Cardiology*, vol. 13, no. 2, pp. 79–98, 2016.

[3] P. Qi, S. Chen, T. Liu et al., "New strategies for developing cardiovascular stent surfaces with novel functions (review)," *Biointerphases*, vol. 9, no. 2, p. 029017, 2014.

[4] S. Browne and K. E. Healy, "Matrix-assisted cell transplantation for tissue vascularization," *Advanced Drug Delivery Reviews*, 2018.

[5] C. Pan, Y. Hu, Y. Hou et al., "Corrosion resistance and biocompatibility of magnesium alloy modified by alkali heating treatment followed by the immobilization of poly (ethylene glycol), fibronectin and heparin," *Materials Science & Engineering C*, vol. 70, pp. 438–449, 2016.

[6] G. Li, P. Yang, W. Qin, M. F. Maitz, S. Zhou, and N. Huang, "The effect of coimmobilizing heparin and fibronectin on titanium on hemocompatibility and endothelialization," *Biomaterials*, vol. 32, no. 21, pp. 4691–4703, 2011.

[7] T. Liu, X. Wang, X. Tang et al., "Surface modification with ECM-inspired SDF-1α/laminin-loaded nanocoating for vascular wound healing," *ACS Applied Materials & Interfaces*, vol. 9, no. 36, pp. 30373–30386, 2017.

[8] J. Wang, Y. Chen, T. Liu et al., "Covalent co-immobilization of heparin/laminin complex that with different concentration ratio on titanium surface for selectively direction of platelets and vascular cells behavior," *Applied Surface Science*, vol. 317, pp. 776–786, 2014.

[9] J. Li, K. Zhang, F. Wu, Z. He, P. Yang, and N. Huang, "Constructing bio-functional layers of hyaluronan and type IV collagen on titanium surface for improving endothelialization," *Journal of Materials Science*, vol. 50, no. 8, pp. 3226–3236, 2015.

[10] K. Zhang, J.-A. Li, K. Deng, T. Liu, J.-Y. Chen, and N. Huang, "The endothelialization and hemocompatibility of the functional multilayer on titanium surface constructed with type IV collagen and heparin," *Colloids and Surfaces B: Biointerfaces*, vol. 108, pp. 295–304, 2013.

[11] S. Beumer, G. J. Heijnen-Snyder, M. J. W. Ijsseldijk, P. G. de Groot, and J. J. Sixma, "Fibronectin in an extracellular matrix of cultured endothelial cells supports platelet adhesion via its ninth type III repeat: a comparison with platelet adhesion to isolated fibronectin," *Arteriosclerosis, Thrombosis, and Vascular Biology*, vol. 20, no. 4, pp. E16–E25, 2000.

[12] W. Bergmeier and R. O. Hynes, "Extracellular matrix proteins in hemostasis and thrombosis," *Cold Spring Harbor Perspectives in Biology*, vol. 4, no. 2, p. a005132, 2012.

[13] F. Zhang, M. Fath, R. Marks, and R. J. Linhardt, "A highly stable covalent conjugated heparin biochip for heparin-protein interaction studies," *Analytical Biochemistry*, vol. 304, no. 2, pp. 271–273, 2002.

[14] K. Nakano, K. Egashira, S. Masuda et al., "Formulation of nanoparticle-eluting stents by a cationic electrodeposition coating technology: efficient nano-drug delivery via bio-absorbable polymeric nanoparticle-eluting stents in porcine coronary arteries," *JACC: Cardiovascular Interventions*, vol. 2, no. 4, pp. 277–283, 2009.

[15] J. S. Golub, Y.-T. Kim, C. L. Duvall et al., "Sustained VEGF delivery via PLGA nanoparticles promotes vascular growth," *American Journal of Physiology-Heart and Circulatory Physiology*, vol. 298, no. 6, pp. H1959–H1965, 2010.

[16] P. Galvin, D. Thompson, K. B. Ryan et al., "Nanoparticle-based drug delivery: case studies for cancer and cardiovascular applications," *Cellular and Molecular Life Sciences*, vol. 69, no. 3, pp. 389–404, 2012.

[17] T. Liu, Y. Liu, Y. Chen et al., "Immobilization of heparin/poly-l-lysine nanoparticles on dopamine-coated surface to create a heparin density gradient for selective direction of platelet and vascular cells behavior," *Acta Biomaterialia*, vol. 10, no. 5, pp. 1940–1954, 2014.

[18] T. Matsuda and H. Kurumatani, "Surface induced in vitro angiogenesis: surface property is a determinant of angiogenesis," *ASAIO Transactions*, vol. 36, pp. M565–M568, 1990.

[19] A. L. Koenig, V. Gambillara, and D. W. Grainger, "Correlating fibronectin adsorption with endothelial cell adhesion and signaling on polymer substrates," *Journal of Biomedical Materials Research*, vol. 64A, no. 1, pp. 20–37, 2003.

[20] K. Lindl, M. Kresse, and R. H. Müller, "Evaluation of desorption of proteins adsorbed to hydrophilic surfaces by two-dimensional electrophoresis," *Proteomics*, vol. 1, no. 9, pp. 1059–1066, 2015.

[21] S. A. Santoro and L. W. Cunningham, "Fibronectin and the multiple interaction model for platelet-collagen adhesion," *Proceedings of the National Academy of Sciences*, vol. 76, no. 6, pp. 2644–2648, 1979.

[22] M. Benitojardón, S. Klapproth, I. Gimenolluch et al., "The fibronectin synergy site re-enforces cell adhesion and mediates a crosstalk between integrin classes," *eLife*, vol. 6, p. 6, 2017.

[23] C. Ettelaie, D. Fountain, M. E. W. Collier, A. M. Elkeeb, Y. P. Xiao, and A. Maraveyas, "Low molecular weight heparin downregulates tissue factor expression and activity by modulating growth factor receptor-mediated induction of nuclear factor-κB," *Biochimica et Biophysica Acta (BBA)-Molecular Basis of Disease*, vol. 1812, no. 12, pp. 1591–1600, 2011.

[24] L. Li, X. Rui, T. Liu, G. Xu, and S. He, "Effect of heparin-derived oligosaccharide on vascular smooth muscle cell proliferation and the signal transduction mechanisms involved," *Cardiovascular Drugs and Therapy*, vol. 26, no. 6, pp. 479–488, 2012.

[25] J. Bágel'ová, M. Antalík, and M. Bona, "Studies on cytochromec-heparin interactions by differential scanning calorimetry," *Biochemical Journal*, vol. 297, no. 1, pp. 99–101, 1994.

Research Article

PEGylated Polyethylenimine Derivative-Mediated Local Delivery of the shSmad3 Inhibits Intimal Thickening after Vascular Injury

Yu Wang,[1] Danyang Zhao,[2] Xiao Wei,[1] Lin Ma,[1] Jing Sheng,[1] and Ping Lu [iD][1]

[1]*Department of Geriatrics, Shanghai Ninth People's Hospital, Shanghai Jiao Tong University School of Medicine, No. 639, Zhizaoju Road, Shanghai 200011, China*
[2]*Department of Plastic and Reconstructive Surgery, Shanghai Ninth People's Hospital, Shanghai Jiao Tong University School of Medicine, No. 639, Zhizaoju Road, Shanghai 200011, China*

Correspondence should be addressed to Ping Lu; luping.shanghai@163.com

Intimal hyperplasia is a complex process which contributes to several clinical problems such as atherosclerosis and postangioplasty restenosis. Inhibition of Smad3 expression inhibits intimal thickening. Our previous study has modified biscarbamate cross-linked polyethylenimine derivative (PEI-Et) through PEGylation thus obtained polyethylene glycol-graft-polyethylenimine derivative (PEG-Et 1:1), which has lower cytotoxicity and higher gene transfection efficiency compared with PEI-Et. In this study, PEG-Et 1:1 was employed in Smad3 shRNA (shSmad3) delivery for preventing intimal hyperplasia after vascular injury. It was observed that PEG-Et 1:1 could condense shSmad3 gene into nanoparticles with particle size of 115–168 nm and zeta potential of 3–6 mV. PEG-Et 1:1 displayed remarkably lower cytotoxicity, higher transfection efficiency, and shRNA silencing efficiency than PEI-Et and PEI 25 kDa in vascular smooth muscle cells (VSMCs). Moreover, PEG-Et 1:1/shSmad3 polyplex treatment significantly inhibited collagen, matrix metalloproteinase 1 (MMP1), MMP2 and MMP9 expression, and upregulated tissue inhibitor of metalloproteinase 1 (TIMP1) expression both *in vitro* and *in vivo*. Furthermore, intravascular delivery of shSmad3 with PEG-Et 1:1 polyplex efficiently reduced Smad3 expression and inhibited intimal thickening 14 days after vascular injury. Ultimately, this study indicated that PEG-Et 1:1-mediated local delivery of shSmad3 is a promising strategy for preventing intimal thickening.

1. Introduction

Neointimal hyperplasia contributes to the pathophysiological process of several different vascular disorders, such as restenosis after angioplasty, allograft vasculopathy, vein graft stenosis, and atherosclerosis [1–3]. Vascular smooth muscle cells (VSMCs) play major role in intimal hyperplasia, VSMCs change from a contractile phenotype to a synthetic phenotype followed by proliferation and migration during vascular remodeling [3–5], and current therapy which aims to antagonize pathological vascular remodeling is mainly to inhibit VSMCs proliferation [6].

Transforming growth factor-β (TGF-β) is believed to be a critical regulator in the process of intimal hyperplasia; the upregulation of it has been found to stimulate the proliferation and migration of VSMCs as well as the production of extracellular matrix (ECM) after vascular injury [7–9]. Inhibition of TGF-β through different means can also decrease intimal hyperplasia [10–14]. Smad3 locates at the downstream of TGF-β signal pathway and studies have reported that TGF-β stimulates neointimal hyperplasia through Smad3-dependent pathway [15–17]. In addition, our previous studies found that inhibition of Smad3 expression using antisense Smad3 adenovirus vector could suppress the proliferation of VSMCs, reduce the secretion of collagen, and alleviate intimal hyperplasia [17–19], suggesting that inhibiting Smad3 expression is an effective strategy to prevent intimal hyperplasia.

In recent years, nanoparticle-based drug/gene delivery has attracted considerable interests for local drug/gene

delivery to prevent restenosis [20]. Among those, the cationic polyethylenimine (PEI) and branched PEI-based carriers have been tested and proved to be effective gene delivery agents for preventing intimal hyperplasia [21–25]. The transfection efficiency of PEIs is mainly influenced by their molecular weight, branching, particle size, and zeta potential [26]. PEI 25 kDa was proven to have higher transfection efficiency but higher toxicity than low-molecular-weight PEIs [26]. To increase the transfection efficiency and reduce the toxicity of PEIs, they have been modified with ester linkage, disulfide linkage, amide linkage, etc. [26–28]. Among so many modifiers, poly(ethylene glycol) (PEG) was wildly used because of its safety and water solubility [29, 30].

In our previous study, we designed and synthesized a novel biscarbamate cross-linked PEI derivative (PEI-Et), but its cytotoxicity is relative high [31]. In order to increase the transfection efficiency and reduce the toxicity of PEI-Et, we then modified PEI-Et with PEG to construct a PEI-Et derivative, namely, polyethylene glycol-graft-polyethylenimine derivative (PEG-Et 1:1), the weight-average molecular weight (Mw) of PEG-Et 1:1 was 4468 Da, with a polydispersity of 2.19, and it exhibited lower cytotoxicity and higher gene transfection efficiency compared with PEI-Et [32]. Herein, PEG-Et 1:1 was selected as a nonviral carrier to deliver the Smad3 shRNA (shSmad3) for preventing intimal hyperplasia after vascular injury. We anticipated that PEG-Et 1:1 would help to deliver shSmad3 into VSMCs with reduced cytotoxicity and enhanced gene delivery efficiency, whether delivery of shSmad3 by PEG-Et 1:1 could induce the downregulation of Smad3 and then inhibit intimal thickening were also investigated.

2. Materials and Methods

2.1. Materials. Branched PEI (25 kDa, 800 Da), ethidium bromide (EB), ethylene bis(chloroformate), and 3-(4,5-dimethylthiazol-2-yl)-2,5-diphenyltetrazolium bromide (MTT) were purchased from Sigma-Aldrich (St Louis, MO, USA). Methoxy-poly (ethylene glycol)-succinimidyl carbonate (mPEG-Sc; Mw = 2000 Da) was purchased from Yare Biotech (Shanghai, China). Fetal bovine serum (FBS), Dulbecco's modified Eagle's medium (DMEM), and Trypsin-EDTA were purchased from PAA (Cölbe, Germany). Smad3-expressing plasmid, scrambled shRNA plasmid, and green fluorescent protein (GFP) bearing Smad3 shRNA plasmid were obtained from JIKAI Cooperation (Shanghai, China). Cell Counting Kit-8 (CCK-8, Dojindo Kumamoto, Japan) was used to detect VSMCs proliferation. 3F Fogarty embolectomy catheters were purchased from Edwards Systems Technology, USA. The primer sequences used in quantitative real-time polymerase chain reaction (qRT-PCR) analysis were described in Suppl. Table 1. Mouse polyclonal to Smad2/3, mouse monoclonal to type I collagen (Col I), mouse monoclonal to and type III collagen (Col III), mouse monoclonal to MMP1, mouse monoclonal to MMP2, mouse monoclonal to MMP9, goat polyclonal antibody against the C-terminal region of TIMP1, and mouse monoclonal to GAPDH (catalog numbers 610842,

ab6308, NBP1-05119, ab126847, ab2462, ab58803, sc-6832, and ab9484) were used for Western blot analysis. Mouse monoclonal to alpha-smooth muscle actin (α-SMA) (catalog number ab7817) and mouse monoclonal to proliferating cell nuclear antigen (PCNA) (catalog number ab912) were used for immunohistochemistry analysis. All other solvents and reagents were of analytical grade.

2.2. Synthesis of PEG-Et 1:1. The synthesis of PEG-Et1:1 was divided into two steps as our previous study (Figure 1(a)) [32]. The first step was to synthesize PEI-Et. Briefly, 0.04 mol of ethylene bis(chloroformate) solution (freshly anhydrous chloroform as solvent) was added dropwise into PEI 800 Da solution (0.06 mol, freshly anhydrous chloroform as solvent); the mixture was stirred in an ice bath under nitrogen atmosphere for 24 hours. After removing solvent, the sample was dissolved in distilled water and then dialyzed with dialysis tube (MWCO: 3500 Da) for 2 days, followed by lyophilization. The resulting polymer PEI-Et was stored at −20°C for future use.

The second step was to synthesize PEG-Et 1:1, 0.04 mmol of PEI-Et was dissolved in 0.1 M of sodium bicarbonate, and then 0.04 mmol of mPEG-Sc was added to the PEI-Et solution. After the mixture was allowed to stirred for 4 h at 25°C, the resultant PEG-Et 1:1 was dialyzed with dialysis tube (MWCO: 3500 kDa) for 2 days. The acquired polymer PEG-Et 1:1 was lyophilized and stored at −20°C until use.

2.3. Preparation of Plasmid DNA/PEG-Et 1:1 Polyplex. PEG-Et 1:1/shSmad3 complexes were freshly prepared. The complexes of PEG-Et 1:1 and DNA (scrambled shRNA and shSmad3) were freshly prepared in phosphate-buffered saline (PBS, pH 6.0), according to the different N/P ratios. Next, the complexes were condensed by adding polymer solutions to equal volume of the DNA solution (shSmad3 or scrambled shRNA solution); the mixture was then stirred gently and incubated for 30 minutes at room temperature to complete the formation of the polyplexes (Figure 1(b)).

2.4. Characterization of PEG-Et 1:1/shSmad3 Polyplex. PEG-Et 1:1/shSmad3 complexes were freshly prepared at different N/P ratios of 1-20. After 30 minutes incubation at 25°C, the complex solutions were analyzed by 0.9% (w/v) agarose gels in 1 × Tris-acetate (TAE) buffer with a constant voltage of 120 V for 30 minutes. The locations of the shSmad3 bands were visualized by a UV illuminator (Tanon 2500, Shanghai).

PEG-Et 1:1/shSmad3 and PEI-Et/shSmad3 complexes were prepared at various N/P ratios from 1 to 50. The zeta potential and particle size were determined by a particle size analyzer (Zetasizer Nano 2s90, Malvern, Britain). All samples were performed in triplicate.

The morphology of PEG-Et/shSmad3 complexes was detected using a Transmission electron microscopy (TEM) at N/P ratio of 20. 10 μL of the complex solution was placed on a copper grid (100 mesh), followed by dried at room temperature. The samples were examined under 120 Kv by TEM (Tecnai G2 Spirit Biotwin, FEI, USA).
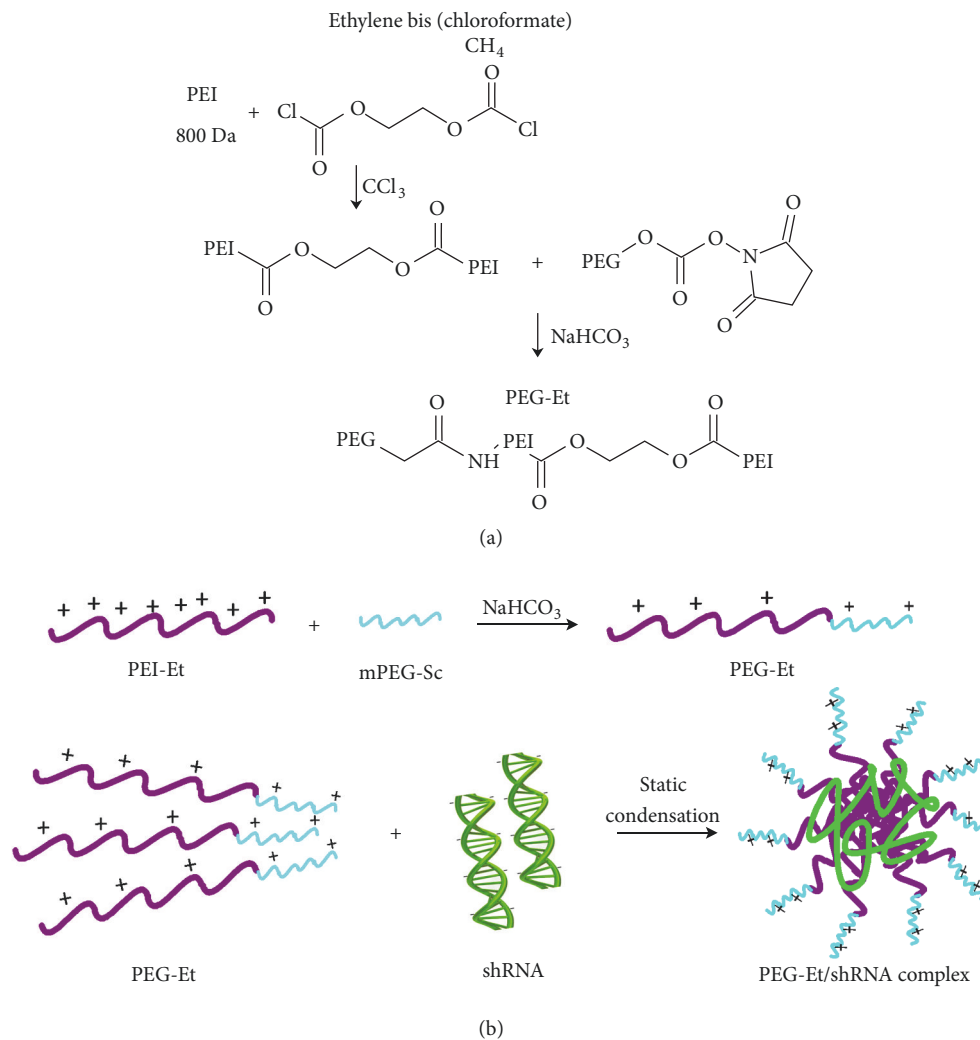
(a)

(b)

FIGURE 1: Synthesis of PEG-Et 1:1 and preparation of plasmid DNA/PEG-Et 1:1 polyplex. (a) Schematic diagram of synthesis of PEG-Et. (b) Schematic diagram of preparation of plasmid DNA/PEG-Et polyplex.

2.5. Cell Culture.

The VSMCs cell lines (C2/2) were purchased from the Life Science Center, Biochemical Research Lab, Asahi Chemical Industry. VSMCs were cultured in DMEM medium supplemented with 15% FBS. Cells were maintained at 37°C in a 95% humidified 5% CO_2 incubator. The cells of 3rd-5rd passage were used for further experiments.

2.6. Cytotoxicity Analysis In Vitro.

MTT assay was tested to investigate the cytotoxicity profiles of PEG-Et 1:1 and PEG-Et 1:1/shSmad3 polyplex; PEI 25 kDa was served as control. The VSMCs were seeded to 96-well plates at a seeding density of 2×10^4 cells per well in DMEM containing 15% FBS and were incubated for 24 hours. The polymers at various concentrations or polymer/shSmad3 complexes at various N/P ratios (dissolved in fresh serum-free DMEM) were added to 96-well plates, followed by incubation for 4 hours. Then, the medium was replaced with complete medium; 48 hours later, 125 μL of MTT (0.5 mg/mL in

fresh serum-free DMEM) was added to each well and incubated for another 6 hours. Subsequently, the medium was discarded and 150 μL/well of DMSO was added. The absorbance was measured at 570 nm (with 630 nm as a reference wavelength) using an ELISA reader (SpectraMax M3, USA). The cell viability was expressed as the percentage of the absorbance relative to that of the control experiment without polymers. Six replicates were counted for each sample.

2.7. Gene Transfection Efficiency Assay.

The VSMCs were seeded to 96-well plates in DMEM containing 15% FBS, which was incubated for 24 hours. For the reporter gene transfection efficiency, the PEG-Et 1:1/shSmad3 polyplexes were added to each well and incubated for 4 h, after that the medium was replaced with fresh serum-containing medium. After 48 hours, GFP protein expression was viewed under a fluorescent microscope (TS100, Nikon, Japan), cells were counted using flow cytometry (Beckerman, USA), and the

percentage of GFP-expressing cells was represented as the gene transfection efficiency.

2.8. qRT-PCR Analysis. Total RNA was extracted from VSMCs (after transfection for 48 h) or carotid arteries using the TRIzol reagent (Sigma, USA) according to the manufacturer's instructions. Spectrophotometer (NanoDrop2000, USA) was used to detect the concentration and purity of RNA. Synthesize of cDNA with 1.0 μg RNA and QuantiTect Reverse Transcription Kit (Qiagen, CA, USA). Amplification was performed using cDNA, and the qRT-PCR was performed with the SYBR green detection system (Thermo Scientific, Waltham, MA, USA) in an sequence detection system (Applied Biosystems, CA, USA). The house keeping gene GAPDH was used as an internal reference. The primer sequences (Smad3, MMP1, MMP2, MMP9, TIMP1, Col I, and Col III) were described in Suppl. Table 1; mRNA levels were normalized to that of GAPDH.

2.9. Western Blot Analysis. Total protein was extracted from VSMCs (after transfection for 48 h) or carotid arteries according to the protocols of the total cellular soluble protein preparation kit. Protein concentrations were examined by the BCA-100 Protein Quantitative Analysis Kit. Equal amount of protein lysates (30 μg) was loaded on 8% sodium dodecyl sulfate-polyacrylamide gel electrophoresis (SDS-PAGE) and then transferred onto a polyvinylidene difluoride membrane (PVDF, Millipore, Billerica, MA) membrane. To minimize nonspecific binding, 5% milk was used to block the membrane for 60 minutes, followed by primary antibodies (Smad3, MMP1, MMP2, MMP9, TIMP1, Col I, and Col III) incubation at 4°C overnight with a gentle shaking. The next day, the bolts were washed with Tris-buffered saline Tween-20 (TBST) buffer and then incubated with horseradish peroxidase-conjugated secondary antibody for 1 h at room temperature, antibody binding was detected using the enhanced chemiluminescence method, and the house keeping gene GAPDH was used as control.

2.10. Cell Proliferation Assay. CCK-8 assay was used to detect VSMCs proliferation. PEG-Et 1:1/shSmad3, PEG-Et 1:1/scrambled shRNA, and PEG-Et 1:1 were added to cells and incubated for 48 h, then the medium was replaced by 500 μL complete medium contain 50 μL CCK-8 solution. The cells were incubated for another 3 hours. Finally, the absorbance was measured using an ELISA reader (SpectraMax M3, USA) at 450 nm. The cell number was expressed as a percentage of the absorbance to that of the control experiment (untreated). Six replicates were counted for each sample.

2.11. Animal Model. New Zealand White rabbits weighing 3.0 to 3.5 kg were purchased from the Laboratory Animal Center of Shanghai Ninth People's Hospital, Shanghai Jiao Tong University School of Medicine. Animals were intravenous anesthetized with 3% pentobarbital sodium 1 ml/kg, and then the left common carotid artery (CCA), left external carotid artery (ECA), left internal carotid artery (ICA), and the bifurcation between them were exposed. After systemic

heparinization, a permanently ligature was made on the ECA at 5 mm away from the bifurcation, the ICA was temporarily ligated by a bulldog clamp, and also a bulldog clamp was put on the proximal end of CCA. A 3F Fogarty balloon catheter (Edwards Systems Technology, USA) was introduced through the branch of the left ECA and positioned at the origin of the left CCA to develop the animal model of vascular balloon injury. The balloon injury was performed by inflating the balloon with about 0.1 mL saline solution and then the arteries were denuded by gently pulling the catheter back along the CCA three times (denudation of endothelium), and the length of denuded arteries was about 4 cm. After balloon injury, a PE-10 catheter (Boston Scientific, USA) was used for local gene administration, gene transfection was performed under the pressure of 6 AT for 30 minutes and the total volume of gene transfer reagents was 200 μL. The experimental animals were divided into four groups according to the difference of gene transfer reagents. The CCA were treated with PEG-Et 1:1/shSmad3 complexes (200 μL, the concentration of shSmad3 was 10 μg/ml, and the concentration of PEG-Et 1:1 was 0.2 mg/ml) in experimental group (n = 6), equal volumes of empty PEG-Et 1:1 or PBS were delivered as controls (n = 6 for each control condition), and another group (n = 6) was untreated after balloon injury. The ECA was ligated immediately after being treated; the bulldog clamps on CCA and ICA were removed. Animals were euthanized and killed for collecting samples 14 days after gene transfection; each artery was divided into three segments, which were fixed in 10% buffered formalin (one segment) and liquid nitrogen (two segments). Animals received humane care, the experiment was approved by the Animal Care and Use Committee of Shanghai Jiao Tong University School of Medicine, and all the animal protocols were carried out in accordance with the Animal Care and Use committee of Shanghai Ninth People's Hospital, Shanghai Jiao Tong University School of Medicine.

2.12. Histology and Morphometry. Carotid arteries were fixed in formalin for 24 hours and then dehydrated in graded alcohols, followed by embedding in paraffin and cutting into slices of 5 μm. The sections were stained with Elastica van Gieson (EVG) and Masson following the manufacturer's instructions, and then photographed using a Nikon microscope. The intima area, media area and intimal-to-medial (I/M) area ratio were calculated on EVG stain slices, collagen fibers were calculated on Masson stain slices. All the data were measured and analyzed using Image-Pro PLUS system.

2.13. Immunohistochemistry. Carotid arteries were fixed in formalin for 24 hours and were cut into slices of 5 μm, sections were repaired with pepsin at 37°C for 30 min and blocked endogenous peroxidase activity with 3% H_2O_2, after that the sections were incubated with mouse anti-α-SMA and mouse anti-PCNA antibodies at 4°C overnight. Negative control was treated with PBS. Next day the sections were then incubated with goat anti-mouse IgG-HRP (Maixin, China) at 25°C for 1 h. Finally, the sections were stained with DAB Detection Kit (Maixin, China) and counterstained
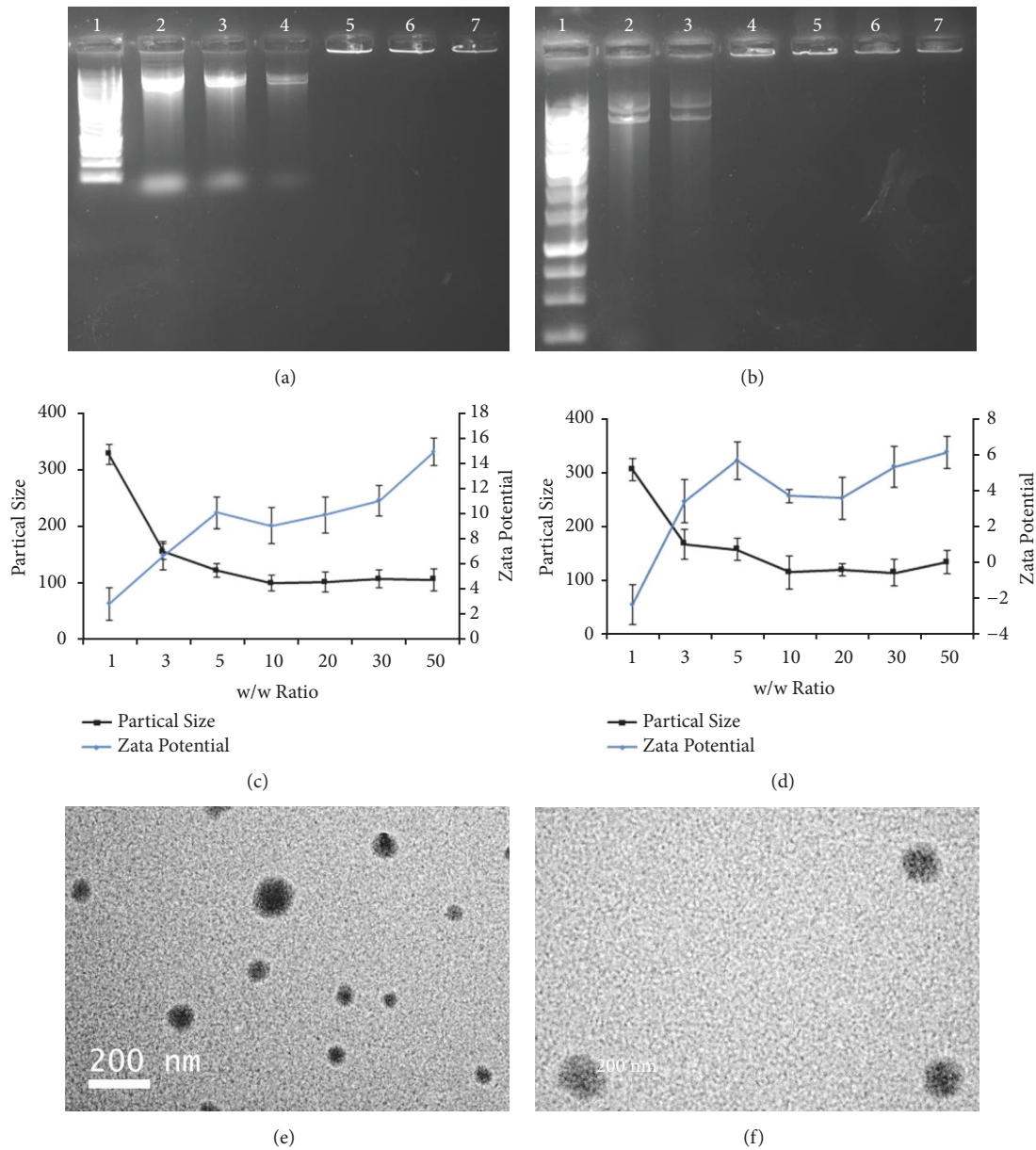
(a)

(b)

(c)

(d)

(e)

(f)

FIGURE 2: Characterization of PEI-Et/shSmad3 and PEG-Et 1:1/shSmad3 complexes. (a) Agarose gel electrophoresis of PEI-Et/shSmad3 complexes at various N/P ratios. (b) Agarose gel electrophoresis of PEG-Et 1:1/shSmad3 complexes at various N/P ratios. Lane 1: Marker, Lane 2: naked shSmad3, and Lanes 3-7: polymer/shSmad3 complexes at N/P ratios of 1, 3, 5, 10, and 20. (c) Particle size and zeta potential of PEI-Et/shSmad3 complexes at various N/P ratios. (d) Particle size and zeta potential of PEG-Et 1:1/shSmad3 complexes at various N/P ratios. (e) Representative transmission electron microscopy image of PEI-Et/shSmad3 complexes at N/P ratio of 20. (f) Representative transmission electron microscopy image of PEG-Et 1:1/shSmad3 complexes at N/P ratio of 20.

with hematoxylin. Five sections of each artery were chosen for quantification, four different fields of each section were imaged at 200 ×. The antigen positive signals were quantified using Image-Pro PLUS system.

2.14. Statistical Analysis. All the data were expressed as mean ± standard deviation and were analyzed by one-way ANOVA with the SPSS statistical program (IBM SPSS Statistics). $P < 0.05$ was considered statistically significant, and $P < 0.01$ or $P < 0.001$ was considered highly statistically significant.

3. Results

3.1. Preparation and Characterization of PEG-Et/shSmad3 Complexes. PEG-Et/shSmad3 complexes were prepared as described in the "materials and methods" section (Figure 1). Gene cargo should be condensed into stable nanoparticle for efficient delivery [33]. Agarose gel electrophoresis was performed to assess the condensation ability of shSmad3 gene by PEG-Et 1:1, naked shSmad3 gene was used as control. As displayed in Figures 2(a) and 2(b), the migration of

shSmad3 gene was completely retarded when N/P ratio was 5 or higher, this indicated that PEG-Et 1:1/shSmad3 complexes were completely formed at an N/P ratio of 5 or above.

An appropriate particle size and zeta potential is helpful for polyplexes to enter cells. The particle size between 50 nm and 200 nm is preferable for cellular uptake of nanoparticles [34, 35]. The particle size of PEG-Et 1:1/shSmad3 complexes varied at different N/P ratios, when the N/P ratio was greater than 3, the particle size was 115-168 nm (Figures 2(c) and 2(d)), that of PEI-Et/shSmad3 complexes was 100-154 nm, the particle size of PEG-Et 1:1/shSmad3 was a little higher compared with PEI-Et/shSmad3 at the same N/P ratio. When the N/P ratio was 1, the particle size of PEG-Et 1:1/shSmad3 and PEI-Et/shSmad3 were higher than 200 nm (326 nm and 306 nm), which were not suitable for cellular uptake. The surface charge can affect the cellular uptake and cytotoxicity of nanoparticles [36, 37]. When the N/P ratio was greater than 3, the zeta potential of PEG-Et 1:1/shSmad3 was 3-6 mV, that of PEI-Et/shSmad3 was 6-15 mV, the zeta potential of PEG-Et 1:1/shSmad3 complexes was lower than that of PEI-Et/shSmad3 complexes at the same N/P ratio (Figures 2(c) and 2(d)), this demonstrated that PEGylation can help to reduce the positive charge of PEI-Et/shSmad3 complexes.

Figures 2(e) and 2(f) showed the representative TEM images of PEI-Et/shSmad3 and PEG-Et/shSmad3 complexes (N/P = 20). The PEG-Et 1:1/shSmad3 complexes were spherical in shape with a diameter 100-130 nm, which were consistent with the particle size analysis.

3.2. Cytotoxicity Assay.

PEG-Et 1:1 could produce immediate cytotoxicity mediated by free PEG-Et 1:1 and delayed cytotoxicity mediated by PEG-Et 1:1/DNA complexes [38], so we measured the cytotoxicity of free PEG-Et 1:1 and PEG-Et 1:1/scrambled shRNA complexes on VSMCs by MTT analysis. The cell viability of PEG-Et 1:1, PEI-Et and PEI 25 kDa treated cells decreased with the increase of polymer concentrations (Figure 3(a)), which indicated that the cytotoxicity of these polymers was concentration-dependent. Moreover, the cytotoxicity of PEG-Et 1:1 was much lower than that of PEI-Et and PEI 25 kDa at the same concentration (P < 0.01). As for the cytotoxicity, the cell viability of PEG-Et 1:1/scrambled shRNA, PEI-Et/scrambled shRNA and PEI 25 kDa/scrambled shRNA decreased with the increase of N/P ratios (Figure 3(b)). When the N/P ratio was 3, the cell viability was 100% in all the three polymer/DNA complexes groups. When the N/P ratio was greater than 3, PEG-Et 1:1/scrambled shRNA showed higher viability than PEI 25 kDa/scrambled shRNA (P< 0.01), and when we raised the N/P ratio from 20 to 50, PEG-Et 1:1/scrambled shRNA showed significantly higher viability than that of PEI-Et/scrambled shRNA and PEI 25 kDa/scrambled shRNA complexes. The results showed that PEG-Et 1:1/scrambled shRNA complexes displayed lower cytotoxicity than PEI-Et/scrambled shRNA and PEI 25 kDa/scrambled shRNA complexes.

3.3. Transfection Efficiency of PEG-Et 1:1.

The gene delivery efficiency of PEG-Et 1:1 was observed by *in vitro* transfection experiments of shSmad3 into VSMCs, with GFP as the reporter gene, PEI 25 kDa and PEI-Et were used as positive controls. Figures 3(c), 3(e), and 3(g) showed the representative fluorescence images, PEI 25 kDa/shSmad3 produced significant GFP expression (Figure 3(c)), with 22.8% of cells expressing GFP (Figures 3(c) and 3(d)), when the N/P ratio was 3-20, the transfection efficiency of PEG-Et 1:1 and PEI-Et increased with the increasing of N/P ratios, and then decreased at a N/P ratio of >20, as determined by flow cytometry (Figures 3(f) and 3(h)). When the N/P ratios were 5, 10, 20, 30, the gene transfection efficiency of PEG-Et 1:1 was significantly higher than that of PEI-Et. These results indicated that PEG-Et 1:1 could be used as a higher efficiency gene delivery vector compared with PEI 25 kDa and PEI-Et. PEG-Et 1:1 displayed maximum efficiency at N/P ratio of 20; the qRT-PCR and Western blot were detected at optimal N/P ratio of 20.

3.4. Gene Silencing Efficiency of PEG-Et 1:1.

The expression of the Smad3 can be knocked down by shSmad3; we measured the ability of PEG-Et 1:1/shSmad3 to reduce Smad3 gene expression in VSMCs by qRT-PCR and Western blot analysis, PEI-Et/shSmad3 and PEI 25 kDa/shSmad3 were used as positive controls. The mRNA expression of Smad3 in PEG-Et 1:1/shSmad3 treated cells was significantly lower compared with PEI-Et/shSmad3 treated cells (32.5% ± 2.8% versus 48.5% ± 2%, P <0.001), PEI 25 kDa/shSmad3 treated cells (32.5% ± 2.8% versus 70.9% ± 1.7%, P <0.001) and untreated cells (32.5% ± 2.8% versus 100% ± 2.3%, P <0.01) (Figure 4(a)). To further confirm the gene silencing effect, Western blot analysis was performed; the expression of shSmad3 protein showed similar results (Figures 4(b) and 4(c)). Based on these results, it would be better to use PEG-Et 1:1 as a carrier for shSmad3 gene therapy in comparison with PEI-Et or PEI 25 kDa, we next tried to apply PEG-Et 1:1 to deliver shSmad3 for the treatment of intimal thickening and investigate the potential mechanism of the therapeutic effect.

3.5. Inhibition Effects of PEG-Et1:1/shSmad3 Polyplex on VSMCs Proliferation.

Inhibition of Smad3 expression can suppress the proliferation of VSMCs [17–19]. VSMCs were treated with PEG-Et 1:1/shSmad3 (N/P=20), PEG-Et 1:1/scrambled shRNA and PEG-Et 1:1. The proliferation of VSMCs treated with PEG-Et 1:1/shSmad3 polyplex was lower than that of PEG-Et 1:1/scrambled shRNA treated group, PEG-Et 1:1 treated group and control group (Figure 4(d)), the proliferation of VSMCs treated with PEG-Et 1:1/scrambled shRNA and PEG-Et 1:1 were slightly lower than control group, but the data showed no statistically significant difference between the three groups (Figure 4(d)). These results indicated that PEG-Et 1:1 mediated shSmad3 treatment could effectively inhibit VSMCs proliferation.

3.6. The Effect of PEG-Et 1:1/shSmad3 on the Expression of Collagen, MMPs, and TIMP1 In Vitro.

Inhibition of Smad3 expression suppresses the synthesis of collagen thus preventing intimal hyperplasia [16, 17, 19]. As shown in Figure 5(a), significant downregulation of Col I, Col III mRNA levels

(a)   (b)   (c)

(d)   (e)

(f)   (g)

(h)
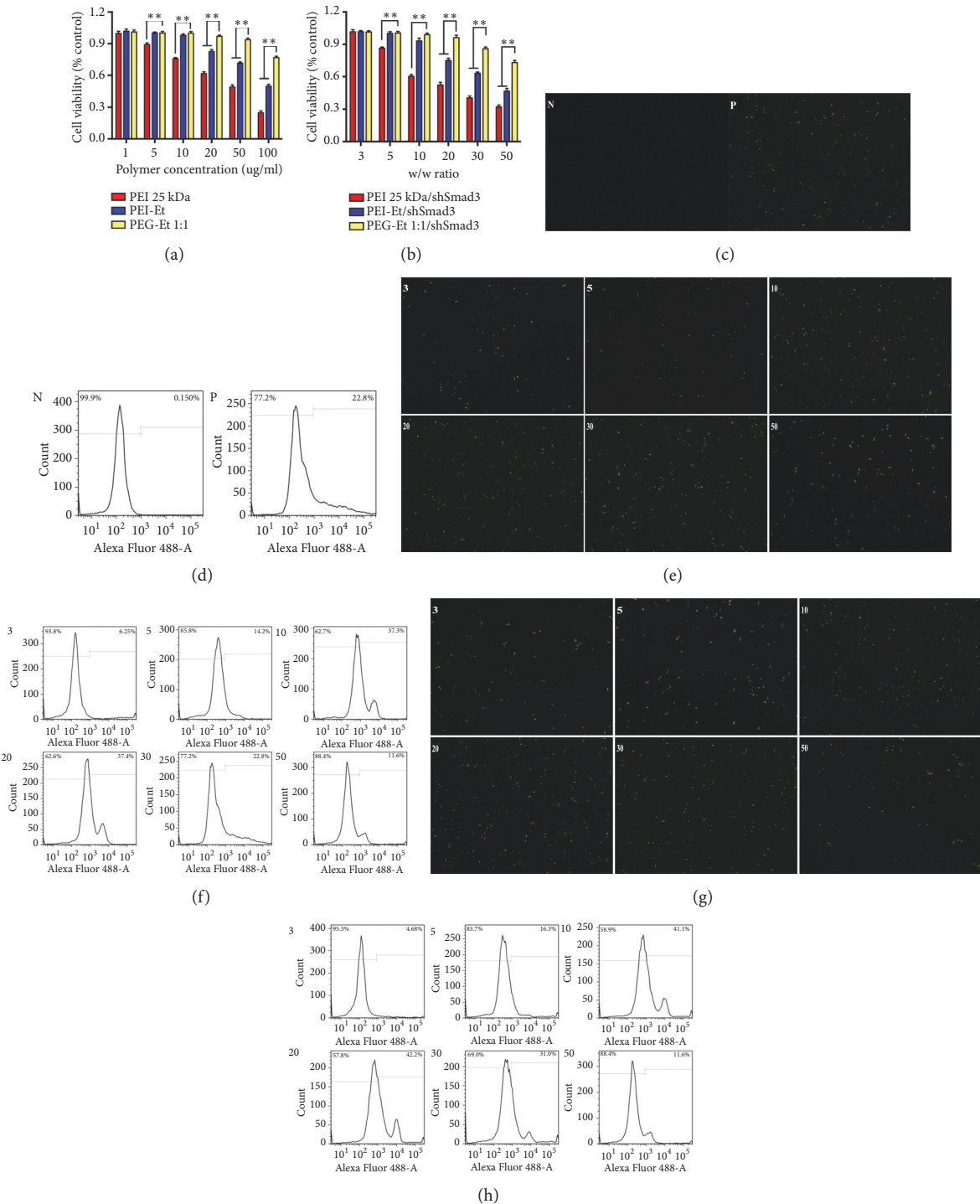
Figure 3: Cytotoxicity and gene transfection efficiency analysis of the PEG-Et 1:1. (a) Cytotoxicity analysis of the PEI 25 kDa, PEI-Et, and PEG-Et 1:1 at various concentrations (1, 5, 10, 20, 50, and 100 μg/ml) in VSMC cell lines. (b) Cytotoxicity analysis of PEG-Et 1:1/scrambled shRNA complexes at various N/P ratios (N/P ratio: 3, 5, 10, 20, 30, and 50) in VSMCs cell lines. (c) Fluorescence images of negative control group (N) and PEI 25 kDa/shSmad3 group (P). (d) Flow cytometry analyzed graphs of negative control group (N) and PEI 25 kDa/shSmad3 group) (P). (e) Fluorescence images of PEI-Et/shSmad3 group at w/w ratios of 3, 5, 10, 20, 30, and 50. (f) Flow cytometry analyzed graphs of PEI-Et/shSmad3 group at w/w ratios of 3, 5, 10, 20, 30, and 50. (g) Fluorescence images of PEG-Et 1:1/shSmad3 group at w/w ratios of 3, 5, 10, 20, 30, and 50. (h) Flow cytometry analyzed graphs of PEG-Et 1:1/shSmad3 group at w/w ratios of 3, 5, 10, 20, 30, and 50.

(a)

(b)

(c)

(d)

FIGURE 4: Gene silencing effect of PEG-Et 1:1 and inhibition effect of PEG-Et 1:1/shSmad3 polyplex on VSMCs proliferation. (a) qRT-PCR analysis of Smad3 mRNA expression, GAPDH ser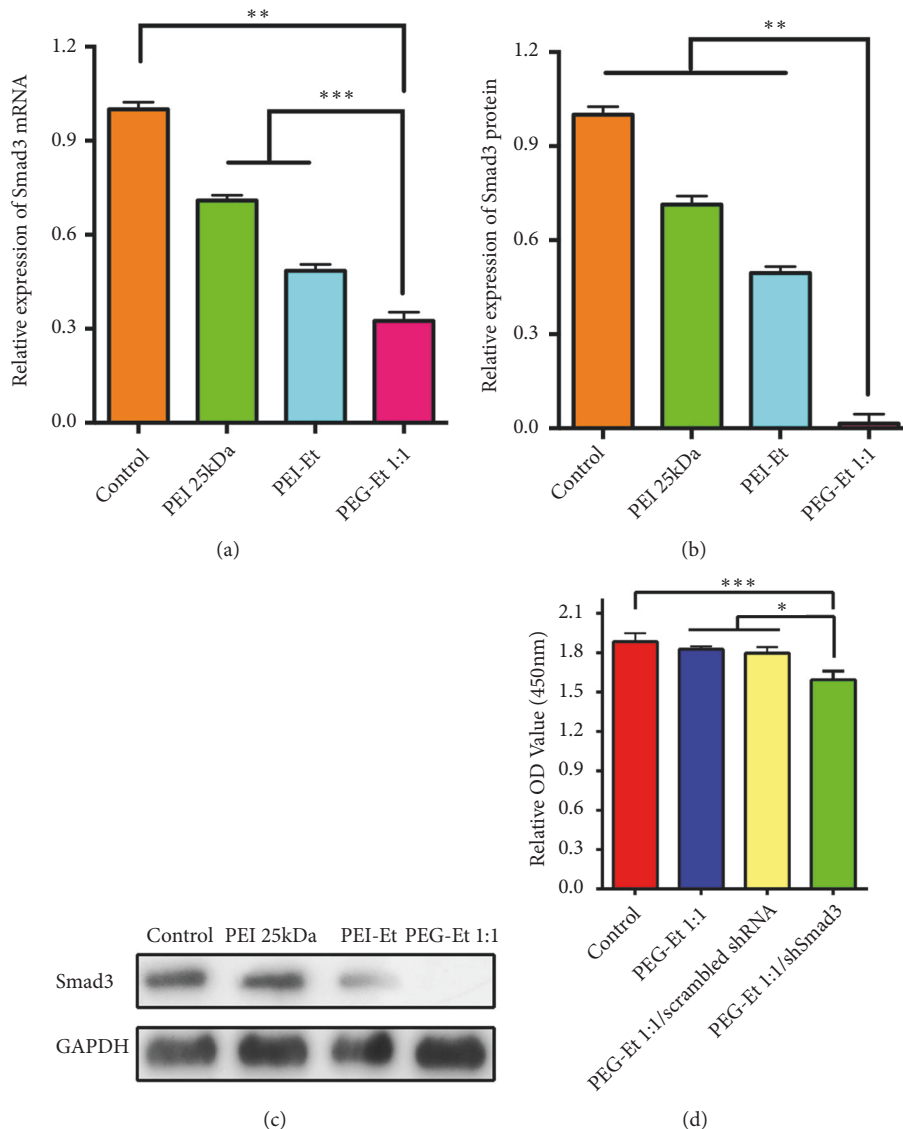ved as internal standard. n = 3. (b) Semiquantitative densitometric analysis of relative Smad3 protein level. n = 3. (c) Western blot analysis of Smad3 protein expression, GAPDH served as internal standard. (d) Effects of PEG-Et 1:1-mediated delivery of shSmad3 and adSmad3 on VSMCs proliferation *in vitro*. The cell number was expressed as a percentage of the absorbance to that of the control group (PEG-Et 1:1/scrambled shRNA) measured by CCK-8. Control: PEG-Et 1:1/scrambled shRNA. n = 6. Each bar shows as mean ± SD. $*P < 0.05$; $**P < 0.01$; $***P < 0.001$.

was found in PEG-Et 1:1/shSmad3 polyplex treated group compared with PEG-Et 1:1/scrambled shRNA treated group, PEG-Et 1:1 treated group, and untreated group, and there were no significant differences between the other three groups for type I and III Collagen mRNA expression. Western blot showed similar result to that of qRT-PCR (Figure 5(b)). These results suggested that PEG-Et 1:1/shSmad3 polyplex could decrease the expression of Col I and Col III.

Studies have shown that MMPs and TIMPs play essential roles in intimal thickening [39–41]; we sought to investigate the effect of PEG-Et 1:1/shSmad3 treatment on the expression of MMPs and TIMP1. Results showed that significantly upregulation of MMP1, MMP2, and MMP9 mRNA was

found in PEG-Et 1:1/shSmad3 polyplex treated group compared with PEG-Et 1:1/scrambled shRNA treated group, PEG-Et 1:1 treated group, and untreated group, while the expression of TIMP1 was downregulated in PEG-Et 1:1/shSmad3 polyplex treated group, and there were no significant differences between the other three groups for MMP1, MMP2, MMP9, and TIMP1 mRNA expression (Figures 5(a) and 5(b)). These results indicated that PEG-Et 1:1/shSmad3 polyplex treatment could increase the expression of MMP1, MMP2, and MMP9 but decrease the expression of TIMP1.

3.7. PEG-Et 1:1/shSmad3 Polyplex Efficiently Reduced Smad3 Expression and Inhibited Intimal Thickening after Vascular
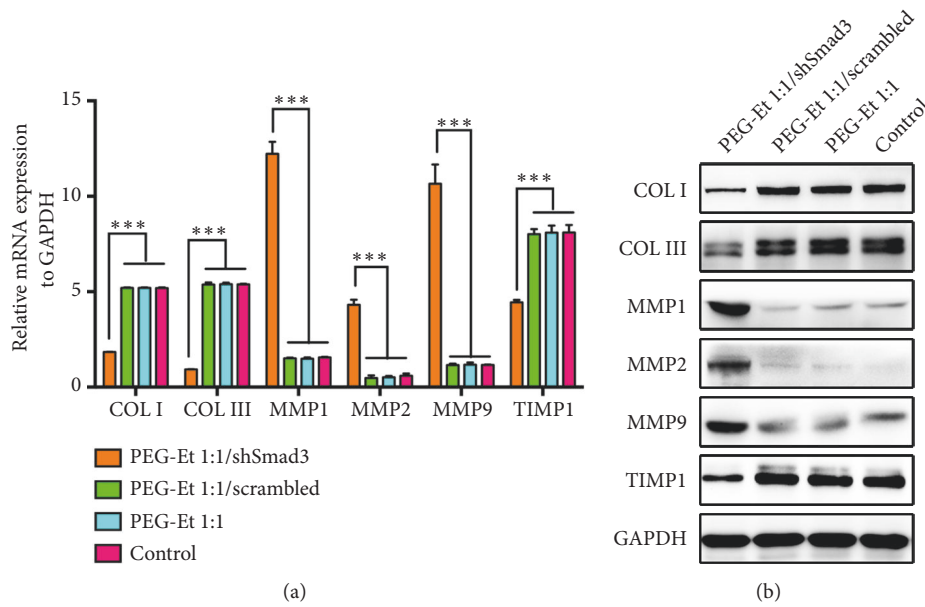
(a)

(b)

FIGURE 5: Effects of shSmad3 gene delivery on the expression of Col I, Col III, MMP1, MMP2, MMP9, and TIMP1. (a) qRT-PCR analysis Col I, Col III, MMP1, MMP2, MMP9, and TIMP1 mRNA expression, GAPDH served as internal standard. n = 3. (b) Western blot analysis of Col I, Col III, MMP1, MMP2, MMP9, and TIMP1 protein expression, GAPDH served as internal standard. Each bar shows as mean ± SD. $* * *P < 0.001$.

Injury. Having illustrated that PEG-Et 1:1/shSmad3 polyplex could efficiently decrease the expression of Smad3 and inhibit VSMCs proliferation *in vitro*, we anticipated that PEG-Et 1:1/shSmad3 could reduce Smad3 expression and inhibit VSMCs proliferation thus preventing intimal thickening *in vivo*. We examined the impact of local delivery of the PEG-Et 1:1/shSmad3 on the expression of Smad3 and intimal thickening 14 days after vascular injury in a rabbit model. As shown in Figure 6, no significant differences in the expressions of Smad3 were observed between empty PEG-Et 1:1 treated group, PBS treated group, and untreated group. The expression of Smad3 was markedly reduced after treatment with PEG-Et 1:1/shSmad3 (200 μL and N/P = 20) 14 days after balloon angioplasty (P < 0.001 for all) (Figure 6). These results suggested that PEG-Et 1:1/shSmad3 polyplex efficiently suppressed the expression of Smad3 *in vivo*.

EVG staining was used to assess the effect of PEG-Et 1:1/shSmad3 polyplex on intimal thickening after vascular injury, as shown in Figure 7(a). Morphometric analysis of all the 4 groups showed that PEG-Et 1:1/shSmad3 polyplex treated group exhibited less intima area (296,929 ± 36,412 μm^2) in comparison with the empty PEG-Et 1:1 treated group (1,080,862 ± 253,490 μm^2, P < 0.001), PBS treated group (1,258,121 ± 225,153 μm^2, P < 0.001), and untreated group (1,333,983 ± 292,778 μm^2, P < 0.001) (Figure 7(d)), the I/M area ratios showed similar results (Figure 7(e)), and there were no significant differences between the other three groups on intima areas or I/M area ratios. These results suggested that PEG-Et 1:1-mediated delivery of the shSmad3 gene could efficiently inhibit intimal thickening.

Immunohistochemistry staining of PCNA (a marker for cell proliferation) and α-SMA was performed to assess

intimal VSMCs proliferation, the majority of cells in the arteries were positive with the monoclonal anti-α-SMA (Figure 7(b)), indicating that they were VSMCs, and the cells which were positive with anti-PCNA were proliferative cells (Figure 7(c)). The ratio of PCNA-positive nuclei to total cell nuclei was significantly decreased in PEG-Et 1:1/shSmad3 polyplex treated group in comparison with the empty PEG-Et 1:1 treated group (P < 0.05), PBS treated group (P < 0.01), and untreated group (P < 0.001) (Figure 7(f)), and no significant differences were observed between the other three groups. These results indicated that the PEG-Et 1:1-mediated delivery of the shSmad3 gene could inhibit arterious intimal VSMCs proliferation.

3.8. The Effect of PEG-Et 1:1/shSmad3 Polyplex on the Expression of Collagen, MMPs, and TIMP1 In Vivo.

Masson staining was used to assess the amount of extracellular collagen fibers (Figure 8(a)); as summarized in Figure 8(b), PEG-Et 1:1/shSmad3 polyplex treated group exhibited reduced ratio of collagen content to total intimal area compared with the PEG-Et 1:1 treated group (P < 0.01), PBS treated group (P < 0.01), and untreated group (P < 0.001) and treated with PEG-Et 1:1/shSmad3 polyplex significantly downregulated the expression of Col I and Col III in comparison with the other three groups 14 days after balloon angioplasty (Figures 8(c) and 8(d)). Furthermore, significant upregulation of MMP1, MMP2, and MMP9 was also found in PEG-Et 1:1/shSmad3 polyplex treated group compared with the other three groups while the expression of TIMP1 was downregulated (Figure 9). These results were consistent with our study *in vitro* (Figure 5).

(a)   (b)
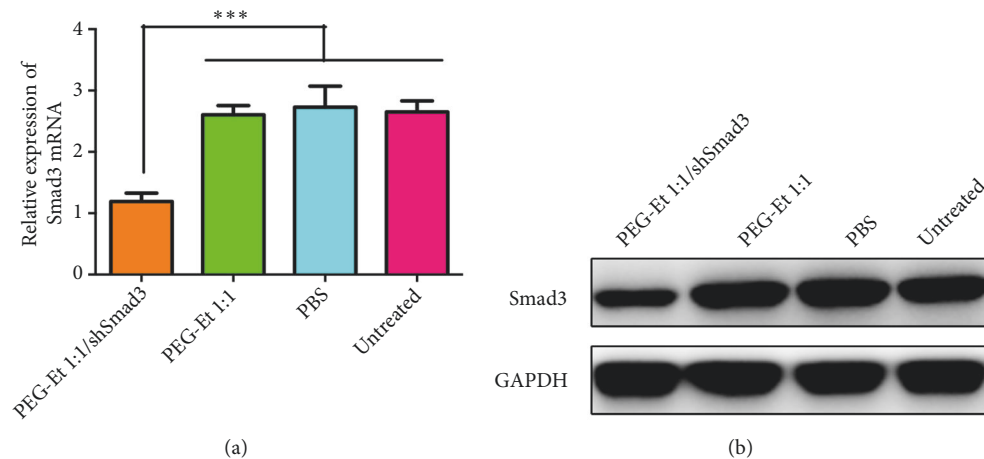
FIGURE 6: The mRNA expression and protein expression of Smad3 in injured arteries 14 days after balloon angioplasty. (a) qRT-PCR analysis of Smad3 mRNA expression, GAPDH served as internal standard. n = 3. (b) Western blot analysis of Smad3 protein expression, GAPDH served as internal standard. Each bar shows as mean ± SD. $* * *P < 0.001$.

4. Discussion

Restenosis is an important clinical problem after arteriovenous stent implantation, arterial intimal resection, and peripheral artery angioplasty [3]. Downregulation of Smad3 expression is an effective strategy to inhibit intimal hyperplasia and prevent restenosis. In this study, we developed PEG-Et 1:1 based nanoparticles to loaded shSmad3 for preventing intimal hyperplasia after vascular injury.

The formation of polymer/DNA complexes is a necessary step in gene delivery, which needs to protect the gene cargo from enzymatic degradation [42]. The migration of shSmad3 gene was completely retarded when the weight ratio (N/P ratio) was 5 or higher (Figure 2(b)), indicated that PEG-Et 1:1/shSmad3 complexes could be prepared at those N/P ratios. We estimated that the positive charge of PEG-Et 1:1 could reduce the negative charges of the phosphate groups in shSmad3 gene, thus retarding the shSmad3 gene migration. The ability of polyplex entering cells is affected by its particle size and zeta potential [43]. When the N/P ratio was greater than 3, the particle size of PEG-Et 1:1/shSmad3 was a little higher compared with PEI-Et/shSmad3 at the same N/P ratio (Figure 2(d)), but the zeta potential of PEG-Et 1:1/shSmad3 complexes was much lower than that of PEI-Et/shSmad3 complexes at the same N/P ratio (Figure 2(d)), small size and reduced positive charge are preferable for nanoparticles to enter cells [34, 35], and weak positive charge can also bring low cytotoxicity [36, 37]; therefore, we speculated that PEG-Et 1:1 might be a promising gene delivery agent.

Compared with PEI-Et and PEI 25 kDa, PEG-Et 1:1 exhibited significantly lower cytotoxicity in VSMCs (Figure 3(a)); as for the cytotoxicity of polymer/scrambled shRNA complexes (Figure 3(b)), PEG-Et 1:1/scrambled shRNA complexes also exhibited lower cytotoxicity than PEI-Et/scrambled shRNA and PEI 25 kDa/scrambled shRNA complexes. PEG modification could help reduce the number of PEI amino groups by coupling reaction to decrease the surface charge [42]. Therefore, lower cytotoxicity of PEG-Et 1:1 was probably

attributed to the reduction of positive charge after PEG modification.

The transfection results of PEG-Et 1:1/shSmad3 complexes to cultured VSMCs were presented in Figures 3(c)–3(h), the transfection efficiency of PEG-Et 1:1 was improved after PEGylation in VSMCs, and the enhanced transfection efficiency of PEG-Et 1:1 relative to PEI-Et was probably attributed to its low cytotoxicity, which was in agreement with a previous study [44]. When the N/P ratio was 3-20, the transfection efficiency of PEG-Et 1:1 increased with the increasing of N/P ratios and then decreased at a N/P ratio of >20 (Figure 3(g)). This phenomenon might be explained as follows: at low N/P ratios, the complexes were unstable and had poor transfection efficiency; at high N/P ratios, the complexes were too stable to release the DNA from the complexes and resulted in low efficiency [31]. PEG-Et 1:1/shSmad3 at optimal N/P ratio of 20 was then selected for transfection of VSMCs. As shown in Figures 4(a)–4(c), the gene silencing effect of PEG-Et 1:1 was obviously better in comparison with PEI-Et or PEI 25 kDa. This was probably due to the low cytotoxicity and higher transfection efficiency of PEG-Et 1:1 in comparison with PEI 25 kDa and PEI-Et. Based on the conclusion that PEG-Et 1:1 has lower cytotoxicity, higher gene transfection efficiency, and shSmad3 silencing efficiency in comparison to PEI-Et and PEI 25 kDa, PEG-Et 1:1/shSmad3 polyplex was used for further research.

Inhibition of Smad3 expression suppresses the proliferation of VSMCs and the synthesis of collagen, thus preventing intimal hyperplasia [16, 17, 19]. PEG-Et 1:1/shSmad3 treatment significantly reduced the proliferation of VSMCs and decreased the expression of collagen in vitro (Figures 4(d) and 5), and in vivo experiment further affirmed the inhibitory effects (Figures 7 and 8); these were consistent with previous studies [16, 19]. These results indicated that inhibiting the expression of Smad3 has great potential for preventing intimal thickening.

MMPs and TIMPs contribute to intimal hyperplasia by regulating ECM degradation as well as VSMCs migration and
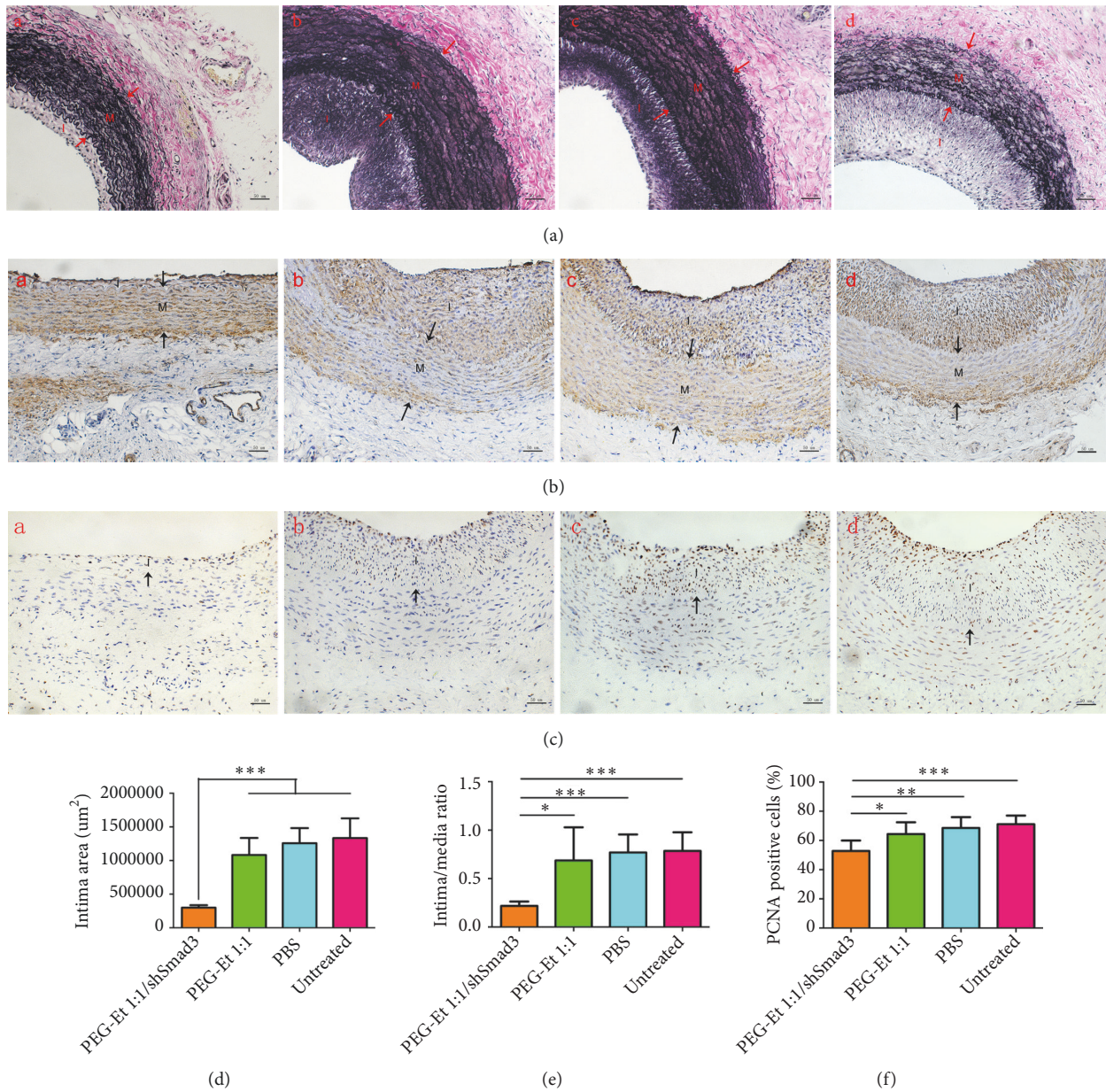
(a)

(b)

(c)

(d)

(e)

(f)

FIGURE 7: Effects of shSmad3 gene delivery on intimal thickening and VSMCs proliferation after vascular injury. (a) Representative EVG sections of injured arteries 14 days after balloon angioplasty. The distance between arrows indicated the media area. Original magnifications: 200 ×. (b) Representative immunohistochemistry staining of α-SMA 14 days after balloon angioplasty. The distance between the arrows indicated the media area. Original magnifications: 200 ×. (c) Representative immunohistochemistry staining of PCNA 14 days after balloon angioplasty. The arrow indicated the internal elastic lamina. Original magnifications: 200 ×. (d) Average intima area for the four injured groups. n = 3. (e) Average I/M area ratios for the four injured groups. n = 3. (f) The ratio of PCNA-positive nuclei to total cell nucleus in intima area. n = 3. Each bar shows as mean ± SD. *$P < 0.05$, **$P < 0.01$; * * *$P < 0.001$. a, PEG-Et 1:1/shSmad3 polyplex treated group; b, PEG-Et 1:1 treated group; c, PBS treated group; d, untreated group.

proliferation; MMPs can degrade most ECM components, while TIMP1 reverses the effect of MMPs; studies have found that coordinated regulation of MMPs and TIMPs contribute to intimal thickening after vascular injury [39–41]. However, the effect of Smad3 on the expression MMPs and TIMP1 after vascular injury remains unknown. PEG-Et 1:1-mediated delivery shSmad3 could decrease TIMP1 expression but increase the expression of MMP1, MMP2, and MMP9 both *in vitro* and *in vivo* (Figures 5 and 9); our study was the first to report that targeted disruption of Smad3 can reduce intimal hyperplasia through regulating the expression of MMPs and TIMP1.

Local intravascular gene delivery is an effective strategy for preventing restenosis during angioplasty procedure [45, 46]. Since previous study reported that endogenous Smad3 expression reached a maximal level around 14 days
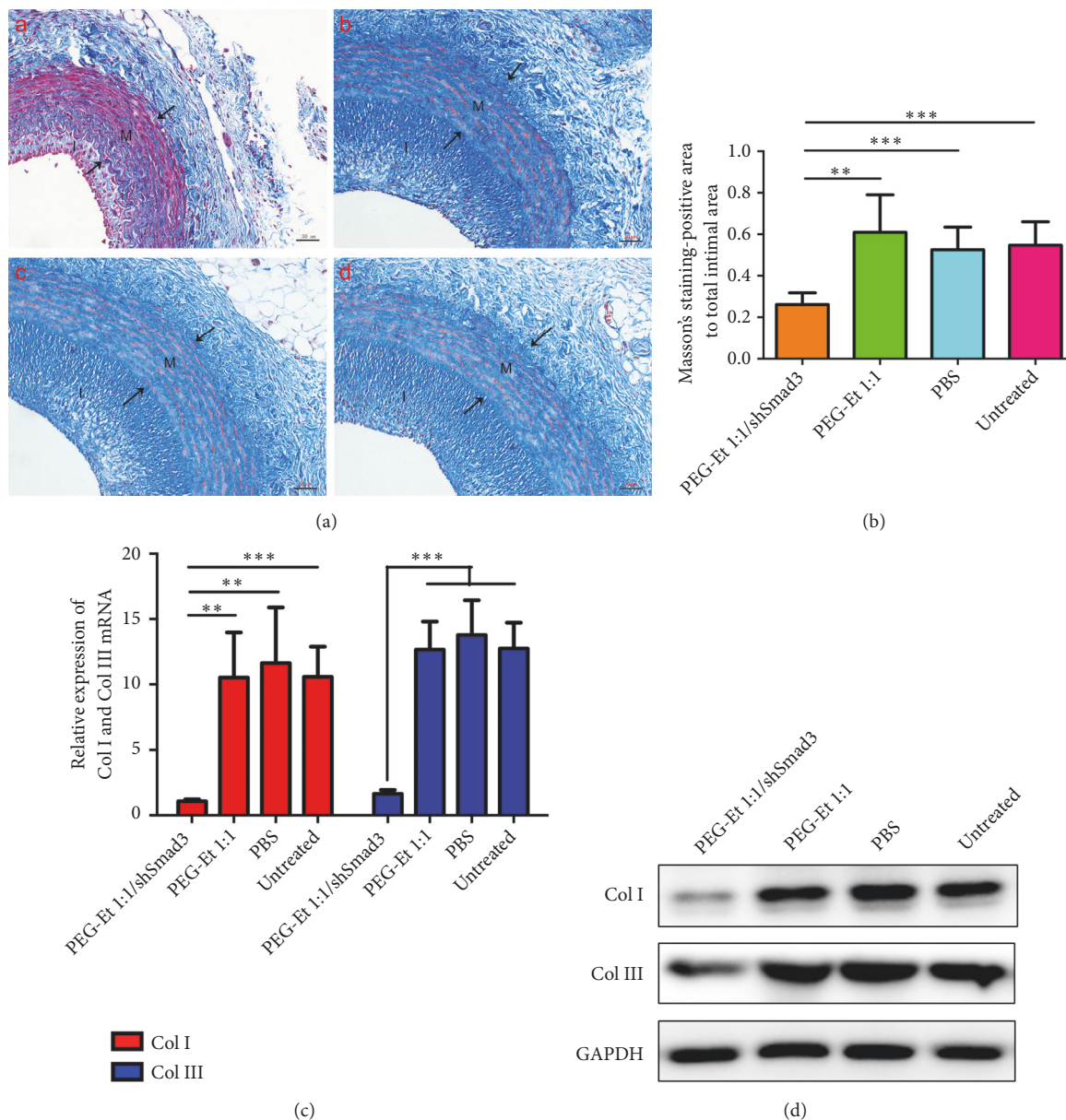
FIGURE 8: Effect of Smad3 gene delivery on intimal collagen content after vascular injury. (a) Representative Masson staining sections of injured arteries 14 days after balloon angioplasty. The distance between the arrows indicated the media area. Original magnifications: 200 ×. (b) The ratio of collagen content to total intimal area in the four injured groups. (c) qRT-PCR analysis of Col I and Col III mRNA expression, GAPDH served as internal standard. n = 3. (d) Western blot analysis of Col I and Col III protein expression, GAPDH served as internal standard. Each bar shows as mean ± SD. $**P < 0.01$; $***P < 0.001$. a, PEG-Et 1:1/shSmad3 polyplex treated group; b, PEG-Et 1:1 treated group; c, PBS treated group; d, untreated group.

after vascular injury [16], we selected this time point for evaluations. PEG-Et 1:1 /shSmad3 complex at N/P of 20 was selected for transfection *in vivo*. We adopted 200 μL volume for local administration in case larger volume (>200 μL) would increase the diameter of CCA. In our study, PEG-Et 1:1/shSmad3 polyplex efficiently suppressed the expression of Smad3 *in vivo* (Figure 6). The neointima and I/M ratio in PEG-Et 1:1/shSmad3 polyplex treated group was less increased than that in the empty PEG-Et 1:1 treated group, PBS treated group, or untreated group

(Figures 7(a), 7(d), and 7(e)). These results proved PEG-Et 1:1/shSmad3 polyplex could obviously downregulate the Smad3 expression in local artery and PEG-Et 1:1-mediated delivery shSmad3 could be a feasible approach for preventing restenosis.

The limitation of the current study is that PEG-Et 1:1 still exhibited cytotoxicity when the concentration was over 50 μg/mL, some modifiers such as Pluronic [47], MoS2 [48], and PLLA [49] can be applied for efficient gene delivery, and in order to reduce its cytotoxicity, we can modify the

(a)   (b)
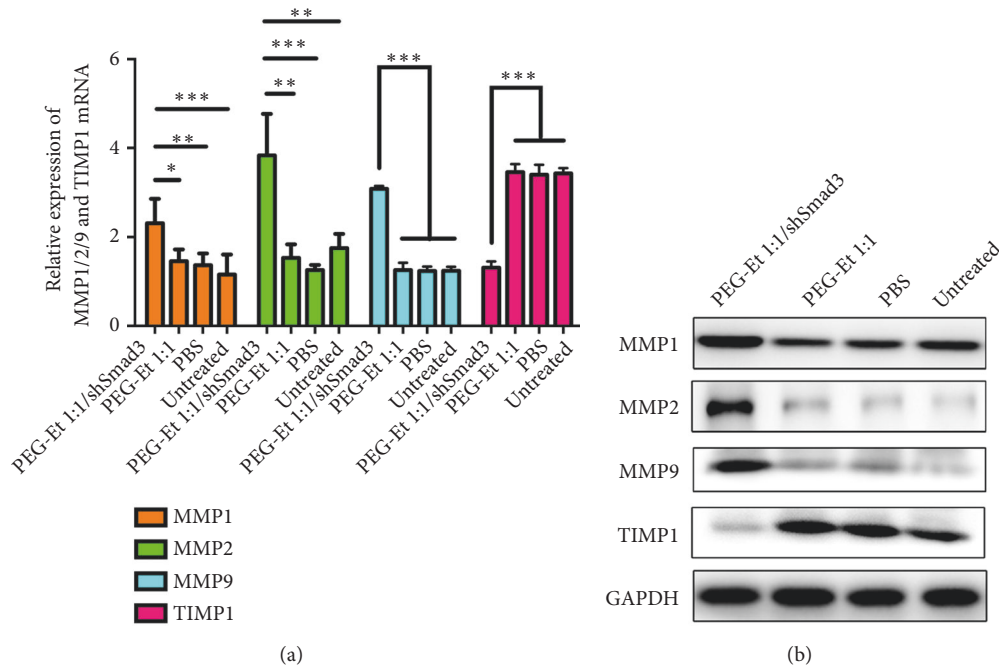
Figure 9: The mRNA expression and protein expression of MMP1, MMP2, MMP9, and TIMP1 in injured arteries 14 days after balloon angioplasty. (a) qRT-PCR analysis of MMP1, MMP2, MMP9, and TIMP1 mRNA expression, GAPDH served as internal standard. (b) Western blot analysis of MMP1, MMP2, MMP9, and TIMP1 protein expression, GAPDH served as internal standard. Each bar shows as mean ± SD. $*P < 0.05$; $**P < 0.01$; $***P < 0.001$.

structure of the cationic polymer with other modifiers. *In vivo* study, we evaluated the results 14 days after vascular injury, we did not select other time points for further evaluations (3 months or one year). Furthermore, loss of Smad3 was found to promote abdominal aortic aneurysm formation in mouse models of inflammatory abdominal aortic aneurysm [50]; shSmad3 gene therapy might have side effect: aneurysm. Longer follow-up of the efficacy and side effect of PEG-Et 1:1/shSmad3 polyplex treatment on neointimal hyperplasia will be undertaken in our future research.

5. Conclusion

In summary, PEG-Et 1:1 exhibited lower cytotoxicity, higher transfection efficiency, and shRNA silencing efficiency than PEI-Et and PEI 25 kDa in VSMCs. PEG-Et 1:1-mediated delivery of shSmad3 could reduce Smad3 expression and VSMCs proliferation both *in vitro* and *in vivo*. Furthermore, intravascular delivery of shSmad3 using PEG-Et 1:1 inhibited intimal thickening 14 days after vascular injury. Our results showed that PEG-Et 1:1 can be served as a nonviral carrier for gene delivery in inhibiting intimal thickening after vascular injury.

Data Availability

The data used to support the findings of this study are available from the corresponding author upon request.

Conflicts of Interest

The authors declare that they have no conflicts of interest.

Authors' Contributions

Yu Wang, Danyang Zhao, Xiao Wei, and Lin Ma contributed equally to this work.

Acknowledgments

Supplementary Materials

Supplementary Table 1: primer pairs used for quantitative real-time polymerase chain analysis in this study. *(Supplementary Materials)*

References

[1] G. F. Neitzel, J. J. Barboriak, K. Pintar, and I. Qureshi, "Atherosclerosis in aortocoronary bypass grafts. Morphologic study and risk factor analysis 6 to 12 years after surgery," *Arteriosclerosis, Thrombosis, and Vascular Biology*, vol. 6, no. 6, pp. 594–600, 1986.

[2] S. M. Schwartz, D. DeBlois, and E. R. M. O'Brien, "The intima. Soil for atherosclerosis and restenosis," *Circulation Research*, vol. 77, no. 3, pp. 445–465, 1995.

[3] A. Forte, B. Rinaldi, L. Berrino, F. Rossi, U. Galderisi, and M. Cipollaro, "Novel potential targets for prevention of arterial restenosis: insights from the pre-clinical research," *Clinical Science*, vol. 127, no. 11, pp. 615–634, 2014.

[4] V. J. Dzau, R. C. Braun-Dullaeus, and D. G. Sedding, "Vascular proliferation and atherosclerosis: new perspectives and therapeutic strategies," *Nature Medicine*, vol. 8, no. 11, pp. 1249–1256, 2002.

[5] G. K. Owens, M. S. Kumar, and B. R. Wamhoff, "Molecular regulation of vascular smooth muscle cell differentiation in development and disease," *Physiological Reviews*, vol. 84, no. 3, pp. 767–801, 2004.

[6] S. O. Marx, H. Totary-Jain, and A. R. Marks, "Vascular smooth muscle cell proliferation in restenosis," *Circulation: Cardiovascular Interventions*, vol. 4, no. 1, pp. 104–111, 2011.

[7] R. Khan, A. Agrotis, and A. Bobik, "Understanding the role of transforming growth factor-β1 in intimal thickening after vascular injury," *Cardiovascular Research*, vol. 74, no. 2, pp. 223–234, 2007.

[8] S. Nikol, J. M. Isner, J. G. Pickering, M. Kearney, G. Leclerc, and L. Weir, "Expression of transforming growth factor-beta 1 is increased in human vascular restenosis lesions," *The Journal of Clinical Investigation*, vol. 90, no. 4, pp. 1582–1592, 1992.

[9] A. Bobik, "Transforming growth factor-βs and vascular disorders," *Arteriosclerosis, Thrombosis, and Vascular Biology*, vol. 26, no. 8, pp. 1712–1720, 2006.

[10] P. A. Kingston, S. Sinha, A. David, M. G. Castro, P. R. Lowenstein, and A. M. Heagerty, "Adenovirus-mediated gene transfer of a secreted transforming growth factor-beta type II receptor inhibits luminal loss and constrictive remodeling after coronary angioplasty and enhances adventitial collagen deposition," *Circulation*, vol. 104, no. 21, pp. 2595–2601, 2001.

[11] J. D. Smith, S. R. Bryant, L. L. Couper et al., "Soluble transforming growth factor-β type II receptor inhibits negative remodeling, fibroblast transdifferentiation, and intimal lesion formation but not endothelial growth," *Circulation Research*, vol. 84, no. 10, pp. 1212–1222, 1999.

[12] D. Sun, Z. Liu, X. Tan et al., "Nanoparticle-mediated local delivery of an antisense TGF-β1 construct inhibits intimal hyperplasia in autogenous vein grafts in rats," *PLoS ONE*, vol. 7, no. 7, Article ID e41857, 2012.

[13] Y. Sun, P. Ye, J. Wu et al., "Inhibition of intimal hyperplasia in murine aortic allografts by the oral administration of the transforming growth factor-beta receptor I kinase inhibitor SD-208," *The Journal of Heart and Lung Transplantation*, vol. 33, no. 6, pp. 654–661, 2014.

[14] W. Zhao, C. Wang, R. Liu et al., "Effect of TGF-β1 on the migration and recruitment of mesenchymal stem cells after vascular balloon injury: involvement of matrix metalloproteinase-14," *Scientific Reports*, vol. 6, no. 1, Article ID 21176, 2016.

[15] E. J. Ryer, R. P. Hom, K. Sakakibara et al., "PKCdelta is necessary for Smad3 expression and transforming growth factor beta-induced fibronectin synthesis in vascular smooth muscle cells," *Arteriosclerosis, Thrombosis, and Vascular Biology*, vol. 26, no. 4, pp. 780–786, 2006.

[16] S. Tsai, S. T. Hollenbeck, E. J. Ryer et al., "TGF-β through Smad3 signaling stimulates vascular smooth muscle cell proliferation and neointimal formation," *American Journal of Physiology-Heart and Circulatory Physiology*, vol. 297, no. 2, pp. H540–H549, 2009.

[17] P. Lu, S. Wang, W. Cai, and J. Sheng, "TGF-beta 1/Smad3 expression and its effects on carotid intimal hyperplasia," *Frontiers in Bioscience - Elite*, vol. 4, no. 6, pp. 2022–2028, 2012.

[18] Z. H. Cheng, P. Lu, S. J. Ma, Y. Chen, and J. Sheng, "Effects of signal transduction interruption of transforming growth factor-beta;1 by anti-Smad3 on proliferation of vascular smooth muscle cells.pdf," *Journal of Shanghai Jiaotong University*, vol. 29, no. 8, pp. 935–937, 2009.

[19] P. Lu, S. Wang, W. Cai, and J. Sheng, "Role of TGF-β1/Smad3 Signaling Pathway in Secretion of Type I and III Collagen by Vascular Smooth Muscle Cells of Rats Undergoing Balloon Injury," *Journal of Biomedicine and Biotechnology*, vol. 2012, Article ID 965953, 8 pages, 2012.

[20] Z. Gu, B. Rolfe, A. Thomas, and Z. Xu, "Restenosis treatments using nanoparticle-based drug delivery systems," *Current Pharmaceutical Design*, vol. 19, no. 35, pp. 6330–6339, 2013.

[21] C. S. Nabzdyk, M. C. Chun, H. S. Oliver-Allen et al., "Gene silencing in human aortic smooth muscle cells induced by PEI-siRNA complexes released from dip-coated electrospun poly(ethylene terephthalate) grafts," *Biomaterials*, vol. 35, no. 9, pp. 3071–3079, 2014.

[22] I. Fishbein, I. Alferiev, M. Bakay et al., "Local delivery of gene vectors from bare-metal stents by use of a biodegradable synthetic complex inhibits in-stent restenosis in rat carotid arteries," *Circulation*, vol. 117, no. 16, pp. 2096–2103, 2008.

[23] H.-L. Che, I.-H. Bae, K. S. Lim et al., "Suppression of post-angioplasty restenosis with an Akt1 siRNA-embedded coronary stent in a rabbit model," *Biomaterials*, vol. 33, no. 33, pp. 8548–8556, 2012.

[24] D. Yamanouchi, J. Wu, A. N. Lazar, K. Craig Kent, C. Chu, and B. Liu, "Biodegradable arginine-based poly(ester-amide)s as non-viral gene delivery reagents," *Biomaterials*, vol. 29, no. 22, pp. 3269–3277, 2008.

[25] K. Liu and M. E. Meyerhoff, "Preparation and characterization of an improved Cu2+–cyclen polyurethane material that catalyzes generation of nitric oxide from S-nitrosothiols," *Journal of Materials Chemistry*, vol. 22, no. 36, pp. 18784–18787, 2012.

[26] R. Molinaro, J. Wolfram, C. Federico et al., "Polyethylenimine and chitosan carriers for the delivery of RNA interference effectors," *Expert Opinion on Drug Delivery*, vol. 10, no. 12, pp. 1653–1668, 2013.

[27] S. Patnaik and K. C. Gupta, "Novel polyethylenimine-derived nanoparticles for in vivo gene delivery," *Expert Opinion on Drug Delivery*, vol. 10, no. 2, pp. 215–228, 2013.

[28] y. Wang, J. Su, C. Wenwei et al., "Hepatocyte-targeting gene transfer mediated by galactosylated poly(ethylene glycol)-graft-polyethylenimine derivative," *Drug Design, Development and Therapy*, vol. 7, pp. 211–221, 2013.

[29] Z. He, B. Chu, X. Wei et al., "Recent development of poly(ethylene glycol)-cholesterol conjugates as drug delivery systems," *International Journal of Pharmaceutics*, vol. 469, no. 1, pp. 168–178, 2014.

[30] A. Alexander, Ajazuddin, J. Khan, S. Saraf, and S. Saraf, "Poly(ethylene glycol)–poly(lactic-co-glycolic acid) based thermosensitive injectable hydrogels for biomedical applications," *Journal of Controlled Release*, vol. 172, no. 3, pp. 715–729, 2013.

[31] Y. Q. Wang, J. Su, F. Wu et al., "Biscarbamate cross-linked polyethylenimine derivative with low molecular weight, low cytotoxicity, and high efficiency for gene delivery," *Journal of Nanomedicine*, vol. 7, pp. 693–704, 2012.

[32] X. Tang, P. Lu, M. Qiu et al., "Screening PEGylated polyethylenimine derivatives for safe and efficient delivery of gene materials," *RSC Advances*, vol. 6, no. 108, pp. 106316–106326, 2016.

[33] S. Shi, K. Shi, L. Tan et al., "The use of cationic MPEG-PCL-g-PEI micelles for co-delivery of Msurvivin T34A gene and doxorubicin," *Biomaterials*, vol. 35, no. 15, pp. 4536–4547, 2014.

[34] G. J. Doherty and H. T. McMahon, "Mechanisms of endocytosis," *Annual Review of Biochemistry*, vol. 78, pp. 857–902, 2009.

[35] I. M. Adjei, B. Sharma, and V. Labhasetwar, "Nanoparticles: cellular uptake and cytotoxicity," *Advances in Experimental Medicine and Biology*, vol. 811, pp. 73–91, 2014.

[36] S. Salatin, S. M. Dizaj, and A. Y. Khosroushahi, "Effect of the surface modification, size, and shape on cellular uptake of nanoparticles," *Cell Biology International*, vol. 39, no. 8, pp. 881–890, 2015.

[37] E. Fröhlich, "The role of surface charge in cellular uptake and cytotoxicity of medical nanoparticles," *International Journal of Nanomedicine*, vol. 7, pp. 5577–5591, 2012.

[38] M. Bauer, C. Lautenschlaeger, K. Kempe, L. Tauhardt, U. S. Schubert, and D. Fischer, "Poly(2-ethyl-2-oxazoline) as alternative for the stealth polymer poly(ethylene glycol): comparison of in vitro cytotoxicity and hemocompatibility," *Macromolecular Bioscience*, vol. 12, no. 7, pp. 986–998, 2012.

[39] A. C. Newby, "Dual role of matrix metalloproteinases (matrixins) in intimal thickening and atherosclerotic plaque rupture," *Physiological Reviews*, vol. 85, no. 1, pp. 1–31, 2005.

[40] A. Azevedo, A. F. Prado, R. C. Antonio, J. P. Issa, and R. F. Gerlach, "Matrix metalloproteinases are involved in cardiovascular diseases," *Basic & Clinical Pharmacology & Toxicology*, vol. 115, no. 4, pp. 301–314, 2014.

[41] M. P. Jacob, "Extracellular matrix remodeling and matrix metalloproteinases in the vascular wall during aging and in pathological conditions," *Biomedicine & Pharmacotherapy*, vol. 57, no. 5-6, pp. 195–202, 2003.

[42] J. C. Fernandes, X. Qiu, F. M. Winnik, M. Benderdour, X. Zhang, K. Dai et al., "Linear polyethylenimine produced by partial acid hydrolysis of poly(2-ethyl-2-oxazoline) for DNA and siRNA delivery in vitro," *International Journal of Nanomedicine*, vol. 8, pp. 4091–4102, 2013.

[43] S. Bhattacharjee, "DLS and zeta potential - What they are and what they are not?" *Journal of Controlled Release*, vol. 235, pp. 337–351, 2016.

[44] H. Petersen, P. M. Fechner, A. L. Martin et al., "Polyethylenimine-*graft*-poly(ethylene glycol) copolymers: influence of copolymer block structure on DNA complexation and biological activities as gene delivery system," *Bioconjugate Chemistry*, vol. 13, no. 4, pp. 845–854, 2002.

[45] N. Cenizo Revuelta, J. Gonzalez-Fajardo, M. Bratos, T. Alvarez-Gago, B. Aguirre, and C. Vaquero, "Role of calcifying nanoparticle in the development of hyperplasia and vascular calcification in an animal model," *European Journal of Vascular and Endovascular Surgery*, vol. 47, no. 6, pp. 640–646, 2014.

[46] M. K. Reddy, J. K. Vasir, S. K. Sahoo, T. K. Jain, M. M. Yallapu, and V. Labhasetwar, "Inhibition of apoptosis through localized delivery of rapamycin-loaded nanoparticles prevented neointimal hyperplasia and reendothelialized injured artery," *Circulation: Cardiovascular Interventions*, vol. 1, no. 3, pp. 209–216, 2008.

[47] W. Fan, X. Wu, B. Ding et al., "Degradable gene delivery systems based on Pluronics-modified low-molecular-weight polyethylenimine: preparation, characterization, intracellular trafficking, and cellular distribution," *International Journal of Nanomedicine*, vol. 7, pp. 1127–1138, 2012.

[48] J. Kim, H. Kim, and W. J. Kim, "Single-layered MoS2-PEI-PEG nanocomposite-mediated gene delivery controlled by photo and redox stimuli," *Small*, vol. 12, no. 9, pp. 1184–1192, 2016.

[49] D. G. Abebe, R. Kandil, T. Kraus, M. Elsayed, O. M. Merkel, and T. Fujiwara, "Three-layered biodegradable micelles prepared by two-step self-assembly of PLA-PEI-PLA and PLA-PEG-PLA triblock copolymers as efficient gene delivery system," *Macromolecular Bioscience*, vol. 15, no. 5, pp. 698–711, 2015.

[50] X. Dai, J. Shen, N. Priyanka Annam et al., "SMAD3 deficiency promotes vessel wall remodeling, collagen fiber reorganization and leukocyte infiltration in an inflammatory abdominal aortic aneurysm mouse model," *Scientific Reports*, vol. 5, no. 1, Article ID 10180, 2015.